DIPLOMARBEIT

Numerical Simulation of Interface Cracks in Glued Die-Attach Semiconductor Devices

ausgeführt zum Zwecke der Erlangung
des akademischen Grades eines Diplom-Ingenieur
unter der Leitung von

Univ. Doz. Dipl.-Ing. Dr. Heinz E. Pettermann

Institut für Leichtbau und Struktur-Biomechanik (E317)

eingereicht an der Technischen Universität Wien
Fakultät für Maschinenwesen und Betriebswissenschaften

von

Jakob Gager
E700/e0425895
Hollitzergasse 2-6/17
1100 Wien.

Wien, im Jänner 2010

Acknowledgment

My deepest gratitude is to my advisor, Univ.-Doz. Dipl.-Ing. Dr. Techn. Heinz Pettermann. His valuable feedback and challenges taught me to think critically and express my ideas.

I would also like to thank ao.Univ.Prof. Dipl.-Ing. Dr. mont. Jürgen Stampfl from the institute of materials science and -technology for acting as my co-advisor.

I am also indebted to the people at K-AI and Infineon who helped me to put theoretical ideas into practice. Particularly, I would like to acknowledge Dr. Balamurugan Karunamurthy, Dr. Michael Nelhiebel, Dr. Arno Zechmann and Dr. Javad Zarbakhsh.

I am also very thankful to o.Univ.Prof. Dipl.-Ing. Dr. Techn. Franz G. Rammerstorfer, Priv.-Doz. Dipl.-Ing. Dr. Techn. Dieter Pahr, and all other people at the ILSB who helped me with lots of discussions and advises.

None of this would have been possible without the support of my parents, Maria and Herbert.

Finally, I would like to thank Steffi for being the wonderful person she is.

Abstract

During service most semiconductor devices are exposed to temperature variations or thermal cycles. Because of the multi-material-design of the devices these thermal loads often induce considerably tractions at the interfaces. These tractions might initiate cracks and delaminations and, therefore, can lead to a device failure due to a loss of electric contact. Hence, it is important to understand the influences of the temperature loads and the resulting stress fields on the cracks to develop reliable semiconductor devices.

The interpretation of the crack situation is based on linear elastic interface fracture mechanic methods. Here, the stress intensity factor, the mode-mix, and the energy release rate are used to assess the crack. To obtain these fracture parameters, the displacement extrapolation method and the virtual crack closure technique are implemented as post processing routines. To compute the underlying stress and displacement fields the finite element method is used. The fracture mechanics methods are verified by means of two example problems for which analytical solutions exist.

Under the assumptions of linear elastic fracture mechanics, two-dimensional models with various cracks located in the interface between the die-attach – mould compound, lead frame – mould compound, and die-attach – die, respectively, are created. For a better accuracy special crack tip elements, which are capable of representing the $1/\sqrt{r}$ singularity, are used. Some of these crack configurations suffer from crack face overlapping, thus, for these special cases contact capabilities are introduced. Furthermore, for all models a manufacturing simulation is performed to predict residual stresses. A thermo-elastic simulation covers the cooling down part of a thermal cycle, and a subsequent fracture mechanics analysis gives the fracture mechanics parameter.

A design study is performed in which various geometry and crack configurations are investigated. It reveals that a variation of the effective clearance has no influence on the fracture parameters as long as the crack remains in the die-attach – mould compound interface. Rather, the bleed-out angle is the parameter with the main influence on the crack tips in this basic configuration. If the crack is extended into the lead frame – mould compound interface the effective clearance shows a strong influence on the crack tip in this interface. By means of a more realistic bleed out shape model the concave shaped bleed out turns out to be an preferable design. A crack extension to both sides, into the lead frame – mould compound and die-attach – die interface shows that the crack tip in the latter interface is not affected by the delamination length on effective clearance side. This means, that under the given modeling assumptions, the delamination of the lead frame does not alter the predicted stress state at the die-attach – die interface.

Kurzfassung

Die meisten Halbleiterbauelemente sind im Betrieb Temperaturschwankungen oder Temperaturzyklen ausgesetzt. Aufgrund ihres Multi-Material-Aufbaues kommt es dadurch häufig zu beträchtlichen Spannungen an den Grenzflächen. Diese Spannungen können Risse und Delaminationen starten und damit zu einem Kontaktverlust und Bauteilfehler führen. Darum ist es wichtig die Einflüsse von temperaturinduzierten Spannungsfelder auf die Risse zu verstehen, um zuverlässige Halbleiterbauelemente zu entwickeln.

In der vorliegenden Arbeit werden die Grenzflächenrisse mittels linear elastischer Interface Bruchmechanik bewertet. Dazu wird der Spannungsintensitätsfaktor, der Modemix und die Energiefreisetzungsrate verwendet. Um diese Größen zu ermitteln wird die „Displacement-Extrapolation-Method“ und die „Virtual-Crack-Closure-Technique“ als Postprocessing Routine implementiert. Beide Verfahren sind mittels zweier analytisch lösbarer Vergleichsbeispiele verifiziert. Die zugrundeliegenden Spannungs- und Verschiebungsfelder werden mit Hilfe der Methode der finiten Elemente bestimmt.

Basierend auf den Annahmen der linear elastischen Bruchmechanik werden zweidimensionale Modelle mit unterschiedlichen Ausgangsrissen in den Grenzflächen zwischen Die-Attach und Vergussmasse, Lead Frame und Vergussmasse und Die-Attach und Chip aufgebaut. Um die Genauigkeit zu erhöhen werden Rissspitzenelemente verwendet, die die $1/\sqrt{r}$ Singularität abbilden können. Weiters werden, wenn notwendig, auch Kontaktelemente zwischen den Rissflanken integriert. Durch die Simulation der Fertigung des Bauteils wird für jedes Modell der fertigungsbedingte Eigenspannungszustand ermittelt. Die thermischen Zyklen werden durch eine einmalige Abkühlung ersetzt und zusammen mit dem Eigenspannungsfeld als Belastung für eine linear elastische Simulation aufgebracht. Aus den Simulationsergebnissen werden die bruchmechanischen Kenngrößen ermittelt.

Mit Hilfe einer Parameterstudie zeigt sich, solange sich der Riss in der Grenzfläche zwischen Die-Attach und Vergussmasse befindet, hat eine Variation des effektiven Abstandes (Abstand zwischen Lead Frame Kante und Klebstoff) keinen, aber der Winkel des Bleed-outs einen sehr großen Einfluss auf die bruchmechanischen Kenngrößen. Hat sich der Riss aber in die Grenzfläche zwischen Lead Frame und Vergussmasse ausgebreitet, zeigt sich ein großer Einfluss des effektiven Abstandes. Ein Modell mit einer zweiteiligen, stückweise linearen Geometrie des Bleed-outs bestärkt die Annahme, dass eine konkave Form besonders gute Eigenschaften aufweist. Die Simulation eines Risses, der von der Grenzfläche zwischen Lead Frame und Vergussmasse bis zur Grenzfläche zwischen Die-Attach und Chip reicht, zeigt, dass die Delamination des effektiven Abstandes keinen Einfluss auf die Rissspitze an der Chipseite hat.

Abbreviations

Material	
E	Young's modulus
ν	Poisson ratio
μ	Shear modulus
α	Dundur's parameter
β	Dundur's parameter
$G(t)$	Shear relaxation modulus
$K(t)$	Bulk relaxation modulus

Continuum mechanics	
σ_{ij}	Stresses
ε_{ij}	Strains
u_i	Displacements
n_i	Normal vector

Fracture mechanics	
$\tilde{K}$	Complex stress intensity factor
K_i	Stress intensity factor component
K^{e}	Norm of stress intensity factor
Y	Geometry factor
a	Crack length
Δa	Crack extension
$\mathscr{G}_i$	Energy release rate
r	Distance from crack tip
ψ	Mode mix
K_{Ic}	Critical stress intensity factor (mode I)
$\mathscr{G}_{\mathrm{Ic}}$	Critical energy release rate (mode I)
ε	Bimaterial parameter
l	Reference length

Nomenclature

Name	Description
Die	Chip
Lead frame	Supporting structure below the die
Die-Attach	Glue connecting die and lead frame
Bleed-out	Die-attach pushed out of the adhesive gap
Mould compound	Compound covering the whole device
Clearance	Distance between lead frame corner and die corner
Effective clearance	Distance between lead frame corner and bleed-out corner

Contents

Chapter 1

Introduction

Microelectronic devices are fabricated by depositing thin films with huge variations in their electrical, mechanical, and thermal properties [21]. One of the major concerns is reliability. However, in the past, electronic properties of materials were primarily considered in the project development. The structural reliability, especially the thermo-mechanical properties have been treated as low priority in the early days. They gain attention recently due to the increasing quality standards in the whole industry.

One of the most common failure modes in Integrated Circuits (ICs) is the occurrence of cracks due to mechanical and thermal mismatch at bi-material interfaces. These cracks may propagate at the essential interface, for example, between die and lead-frame and interrupt the electrical and thermal conduction (see Fig. 1.1), thereby leading to device failures. Moreover, high currents at locations where no crack was nucleated could lead to overheating and subsequent failure of the device [57].

Microelectronics devices are exposed to aggressive conditions not only in the processing steps, but also during operation. For example, ICs for high power applications as employed in the automotive industry are operated under thermal cycles varying from $-55\,^{\circ}\mathrm{C}$ to $150\,^{\circ}\mathrm{C}$. As a result, tractions at the interfaces between dissimilar materials may lead to failure under the effect of many cumulated cyclic loads.

Recently, additional efforts where applied to increase the thermo-mechanical reliability by optimized design and materials [57]. Furthermore, numerous papers have been published dealing with different aspects of interface fracture mechanics with application in electronic packaging, e. g. [2, 34, 44, 67].

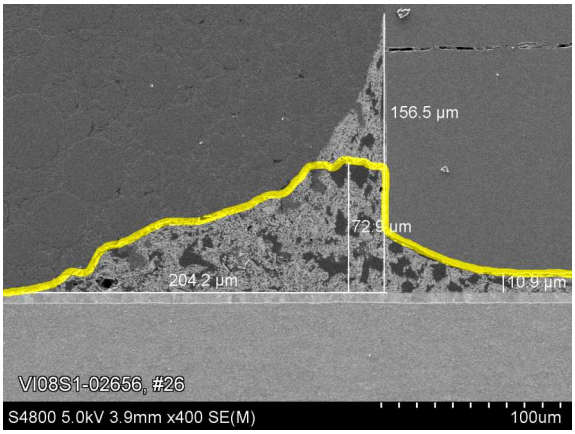

Figure 1.1: SEM image of cracked device with indicated crack ©K-AI.

The goal of the current work is to assess the influence of crucial geometry parameters, like the bleed-out dimensions and the clearance, on the risk of crack initiation. Especially, in the interface between the die-attach and the mould compound, which is known to be the one with the lowest toughness, it is very likely that cracks exist and initiate during thermal or mechanical loading. Thus, it is important to understand the influence of this loading conditions on the cracks, in order to develop a reliable product.

To examine the crack behavior fracture mechanics methods are introduced and implemented as finite element post processing routines. A proper level of abstraction and simplification is carried out, to build up a two dimensional model of the semiconductor device. The basic geometry is supplied by K-AI, Center of expertise in automotive and industrial electronics.The finite element method (ANSYS® 11, ANSYS Inc., 275 Technology Drive, Canonsburg, PA 15317, USA), a commercial FEM software, is used to study various geometry and crack configurations. To account for residual stresses the nonlinear manufacturing process—provided by K-AI—is simulated as well. Finally the results are interpreted and design recommendations are presented.

The thesis is subdivided into four parts. First, a basic introduction into fracture mechanics, including interface fracture mechanics and numerical fracture mechanics is presented. The second part is the introduction and verification of the implemented fracture mechanics methods. The third part considers the semiconductor device, including modelling, material assumptions, simulation procedures, and design studies. And finally, the results of the simulations are given and conclusions are presented.

Chapter 2

Fracture mechanics

> "A crack is made up of empty space, but it is so sharp that it easily cuts glass, rock and metal. Fracture mechanics studies just this phenomenon." Slepyan [56]

2.1 Basic concepts of fracture mechanics

Fracture mechanics is an addition to continuum mechanics to describe the behavior of a cracked body. The classical continuum mechanics is not capable of modeling the complex processes in the close vicinity of the crack tip – the so called, process zone. This process zone is assumed to be negligibly small or behave according to special laws. The key feature of fracture mechanics is that a crack already exists. The nucleation of cracks can be treated by e. g. damage mechanics.

In the field of linear elastic fracture mechanics (LEFM), the whole body is assumed to behave linear elastic. All possible inelastic processes have to take place in a tight region around the crack tip, to ensure the applied assumptions to hold. Thus, the process zone is assumed to be negligibly small, which is true for most brittle materials. Furthermore, the crack faces have to be free of tractions. The LEFM is used to model the fracture of essentially brittle materials.

The following sections deal with LEFM of a homogeneous isotropic body containing a crack under plane strain or plane stress conditions. The elastic constants i. e., the Young's modulus, E, the Poisson ratio, ν, and the shear modulus, μ, are used to describe the material properties. The treatment follows [19, 33].

2.1.1 Introduction

The discipline of fracture mechanics was driven by catastrophic failures like the Liberty ships in world war II, the Comet aircrafts [37], or numerous other disasters [16]. Back in 1907, Wieghardt was the first to address the problem of finding the stress distribution around a crack and demonstrated the square-root singularity at the crack tip [9]. However this achievement remains unappreciated. A fundamental advancement was done by Griffith in 1921 who applied energy considerations for the analysis of fracture phenomenon [9]. The break through in fracture mechanics came when Irwin introduced the stress intensity factor concept in 1957 [9]. This concept allows the application of fracture mechanics in an engineering way. Since then numerous researchers pushed forward the field of fracture mechanics. In the 1960s, Paris introduced a concept for fatigue fracture propagation. There is still a lot of unsolved problems, and thus, fracture mechanics is in steady development.

2.1.2 Crack geometry

A two-dimensional plane crack (Griffith crack) is described by the two crack faces and is border by the crack tips. The crack length is $2a$ and the plane formed by the crack faces and the out-of-plane z-axis is called crack plane, see Fig. 2.1. Basically, the crack is considered to occur in an infinite body. The crack faces are assumed to be traction free and parallel to each other. Moreover, the crack tips are assumed to be infinitely sharp.

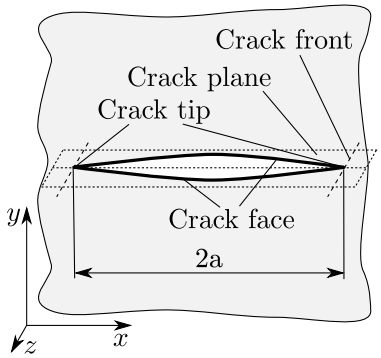

Figure 2.1: Denotations of a typical two dimensional crack.

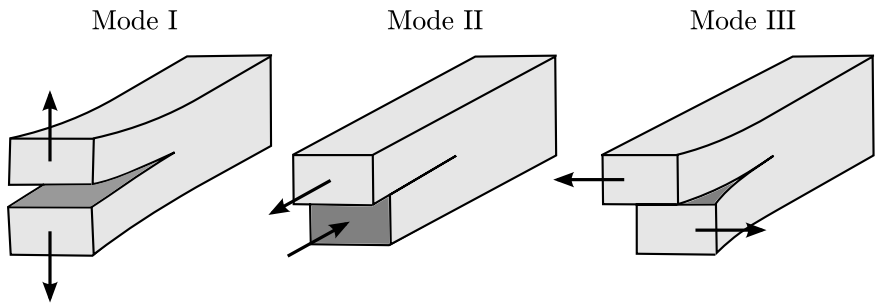

Figure 2.2: Crack opening modes.

2.1.3 Crack opening modes

There are three different crack opening modes, with respect to the deformations of a crack (see Fig. 2.2).

Mode I – opening mode; the crack faces moves perpendicular to the crack plane and are symmetric with respect to the crack plane.

Mode II – sliding mode or in-plane shear mode; the crack faces move on each other in the direction perpendicular to the crack front. Here the displacements are antisymmetric with respect to the crack plane.

Mode III – tearing mode or out-of-plane shear mode; the crack faces slide in the direction parallel to the crack front in an antisymmetric manner.

2.1.4 Stress and displacement field

Within linear elastic fracture mechanics the stress and displacement field in the vicinity of a crack tip depends on the crack length half, a, the applied stress, σ, and a geometry factor, Y. The later, accounts for the local geometry features (e. g. edge crack, finite ligament) and the finite size of the component. Irwin introduced the stress intensity factor which relates these quantities as [19]

$$K = \sigma\sqrt{\pi a}\, Y \ , \tag{2.1}$$

for describing the crack tip situation. For pure mode I (or pure mode II) the stress field

in the vicinity of the crack tip can be expressed by

$$\begin{pmatrix} \sigma_{xx} \\ \sigma_{yy} \\ \tau_{xy} \end{pmatrix} = \frac{K_i}{\sqrt{2\pi r}} \cdot \begin{pmatrix} f^i_{xx}(\theta) \\ f^i_{yy}(\theta) \\ f^i_{xy}(\theta) \end{pmatrix} + (O) \ , \qquad i = \{\mathrm{I}, \mathrm{II}\} \ . \tag{2.2}$$

Here, r and θ give the cylindrical coordinates of the considered point (see. 2.3), and f^i_{kl} with $k, l = \{x, y\}$ is a function of θ which can be found in e. g. [19]. The square-root singularity with respect to the radial coordinate r, $\frac{1}{\sqrt{r}}$, can be clearly seen. (O) represents terms of higher order with respect to r with a vanishing effect as $r \to 0$.

With the application of Hook's material law the displacements can be derived in the form

$$\begin{pmatrix} u_x \\ u_y \end{pmatrix} = \frac{K_i}{2\mu}\sqrt{\frac{r}{2\pi}} \cdot \begin{pmatrix} g^i_x(\theta) \\ g^i_y(\theta) \end{pmatrix} + (O) \ , \qquad i = \{\mathrm{I}, \mathrm{II}\} \ , \tag{2.3}$$

where u_j is the displacement in direction j, and g^i_j is a function of θ.

For mode III similar equations like Eq. (2.2) and (2.3) exist. This thesis focuses on 2 dimensional problems, without out-of-plane shear stresses. Thus, for additional information about mode III the reader is referred to [19, 33].

In general, a combination of mode I, II, and III occur and due to the assumptions of the LEFM, these three modes can be superimposed. Thus, for mixed mode cases Eq. (2.2) and (2.3) are combined to

$$\sigma_{ij}(r, \theta) = \frac{1}{\sqrt{2\pi r}} \left(K_{\mathrm{I}} \, f^{\mathrm{I}}_{ij}(\theta) + K_{\mathrm{II}} \, f^{\mathrm{II}}_{ij}(\theta) + K_{\mathrm{III}} \, f^{\mathrm{III}}_{ij}(\theta) \right) \ , \qquad i, j = \{x, y\} \ , \tag{2.4}$$

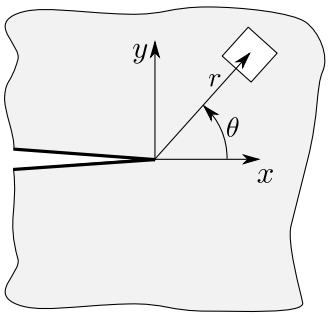

Figure 2.3: Crack in a homogeneous material.

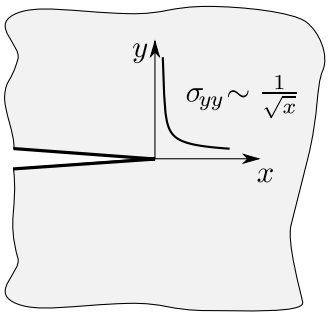

Figure 2.4: Stress distribution σ_{yy} in the vicinity of the crack tip.

and

$$u_i(r,\theta) = \frac{1}{2\mu}\sqrt{\frac{r}{2\pi}}\left(K_{\mathrm{I}}\, g_i^{\mathrm{I}}(\theta) + K_{\mathrm{II}}\, g_i^{\mathrm{II}}(\theta) + K_{\mathrm{III}}\, g_i^{\mathrm{III}}(\theta)\right) \ , \qquad i = \{x, y\} \ . \tag{2.5}$$

2.1.5 Fracture mechanics parameters

Stress intensity factor

To classify a crack and to describe the stress and displacement field, Irwin introduced the stress intensity factor concept. As mentioned above, the stress field in the vicinity of the crack tip is solely defined by the crack length, the applied stress, and the geometry factor (see Eq. (2.1)). The derived stress intensity factor describes the stresses and displacements in an unambiguous way. This means, cracks with the same stress intensity factors exhibit the same stress and displacement field even if they are subjected to different loads and appear in different structures.

Due to this unambiguousness, explicit equations for the stress intensity factors of different geometry and loading situations can be given and are collected in fracture mechanics handbooks (e. g. [40, 61]). Stress intensity factors are additive (the superposition principle applies) but only to the same mode.

A generalized form can be expressed as [33]

$$\begin{aligned} K_{\mathrm{I}} &= \sigma_{yy}\sqrt{\pi a}\, Y_{\mathrm{I}} \ , \\ K_{\mathrm{II}} &= \sigma_{xy}\sqrt{\pi a}\, Y_{\mathrm{II}} \ , \end{aligned} \tag{2.6}$$

where a is the crack length, σ_{kl} is a representative stress (e. g. far field stress) and Y characterizes the geometry, respectively [33].

Mode mix

The general loading case is a mixed mode loading. This implies that tensile as well as the shear far field stresses are present. To characterize such a situation the mode mix can be defined as

$$\tan\psi = \frac{K_{\mathrm{II}}}{K_{\mathrm{I}}} \,. \tag{2.7}$$

In case of interface fracture the mode mix attracts special interest, as will be discussed in Sec. 2.2.

Energy release rate

Based on Griffith's energy considerations the energy released per unit area is called energy release rate and reads [19]

$$\mathscr{G} = -\frac{1}{B}\frac{d(\Pi^i + \Pi^e)}{da} \,. \tag{2.8}$$

Here Π^i = is the elastic potential, Π^e is the potential of external forces if the crack is extended by an area $B\,da$, B the thickness and da the crack extension. The energy release rate has the dimension of a work per unit length squared or force per unit length and is therefore often called as crack extension force.

For linear elastic fracture mechanics Irwin derived the link between energy release rate and stress intensity factor. This relationship can be expressed as

$$\begin{aligned} \mathscr{G}_{\mathrm{I}} &= \frac{K_{\mathrm{I}}^2}{E'} \,, \\ \mathscr{G}_{\mathrm{II}} &= \frac{K_{\mathrm{II}}^2}{E'} \,, \\ \mathscr{G}_{\mathrm{III}} &= \frac{K_{\mathrm{III}}^2(1+\nu)}{E} \,, \end{aligned} \tag{2.9}$$

where

$$E' = E \,, \qquad \text{for plane stress,} \tag{2.10}$$

$$E' = \frac{E}{1-\nu^2} \,, \qquad \text{for plane strain.} \tag{2.11}$$

When the crack is exposed to a mixed mode condition the individual strain energy release

rates can be summed up to achieve the total energy release rate as

$$\mathscr{G} = \mathscr{G}_{\mathrm{I}} + \mathscr{G}_{\mathrm{II}} + \mathscr{G}_{\mathrm{III}} = \frac{K_{\mathrm{I}}^2}{E'} + \frac{K_{\mathrm{II}}^2}{E'} + \frac{K_{\mathrm{III}}^2(1+\nu)}{E} \,. \tag{2.12}$$

This indicates that in contrast to the stress intensity factors, the superposition principle applies also to different modes.

2.1.6 Fracture toughness

The (interface) parameter which is used together with linear fracture mechanics is the fracture toughness, K_{c}. Since mode I condition is typically the most severe case the value of K_{Ic} is always smaller than the values for K_{IIc} and K_{IIIc} respectively. Thus, basically K_{Ic} is called the fracture toughness. Furthermore, this toughness value belongs to a plane strain assumption as this is the most critical case, usually. To be conservative, in most of the cases K_{Ic} is used instead of the feasible K_{IIc} or K_{IIIc} values. For the determination of fracture toughness values standardized testing methods like notched-bar impact testing are applied [19]. For many materials K_{Ic} strongly depends on the temperature and on the specimen thickness thus, the fracture toughness is no real material parameter.

In case of mixed mode situation both K_{Ic} and K_{IIc} can be used to assess the likeliness of crack initiation.
Typical values of the fracture toughness K_{Ic} are taken from [19] and are presented in Tab. 2.1. With Eqs. (2.9) corresponding critical strain energy release rates , $\mathscr{G}_{\mathrm{Ic}}$, $\mathscr{G}_{\mathrm{IIc}}$, $\mathscr{G}_{\mathrm{IIIc}}$ can be defined.

Table 2.1: Fracture toughness values K_{Ic} for several materials [19].

Material	K_{Ic} [MPa$\sqrt{\mathrm{mm}}$]
Mild steel	1000 . . . 4000
High strength steel	800 . . . 3000
Al-alloys	600 . . . 2000
Glass	20 . . . 40
Concrete	5 . . . 30

2.1.7 Fracture criterion

Stress intensity criterion

If pure mode I acts on the crack tip, the fracture criterion can be expressed as

$$K_{\mathrm{I}} = K_{\mathrm{Ic}} \ . \tag{2.13}$$

Similar simple equations exist for pure mode II and III loading. The critical state can be reached by increasing the load, $\sigma \to \sigma_c$, by increasing the crack length, $a \to a_c$, or by a combination of both, cf Eqs. (2.6).

For the general mixed mode condition, some more advanced fracture criterion has to be applied. Crack initiation under mixed mode conditions takes place when K_{I} and K_{II} reach some values to satisfy the equations of a fracture envelope. There exist several different forms for the fracture locus, see Fig. 2.5.

Circular $K_{\mathrm{I}}^2 + K_{\mathrm{II}}^2 = K_{\mathrm{Ic}}^2$, simplest case but implies $K_{\mathrm{Ic}} = K_{\mathrm{IIc}}$ which is in general not the case and a very conservative assumption.

Linear $\frac{K_{\mathrm{I}}}{K_{\mathrm{Ic}}} + \frac{K_{\mathrm{II}}}{K_{\mathrm{IIc}}} = 1$, a preferred envelope since derived predictions are relatively safer than relying the design upon the elliptic.

Ellipse $\left(\frac{K_{\mathrm{I}}}{K_{\mathrm{Ic}}}\right)^2 + \left(\frac{K_{\mathrm{II}}}{K_{\mathrm{IIc}}}\right)^2 = 1$.

Quadratic $\left(\frac{K_{\mathrm{I}}}{K_{\mathrm{Ic}}}\right)^2 + C\frac{K_{\mathrm{I}}K_{\mathrm{II}}}{K_{\mathrm{Ic}}K_{\mathrm{IIc}}} + \left(\frac{K_{\mathrm{II}}}{K_{\mathrm{IIc}}}\right)^2 = 1$, where C is a fitting parameter, is also a preferred envelope, due to the relatively safer prediction.

Illustratively, this implies that a point in the K_{I}–K_{II} plane, inside the fracture locus, indicates a safe state, see Fig. 2.5. A point located on or outside the fracture envelope induces crack initiation. For homogeneous materials this initiation generally takes place under a certain angle to the crack plane (crack kinking).

It should be noted that the proposed envelopes have no theoretical basis and the applied fracture locus should be verified by experimental testing. Furthermore, the criteria imply self similar crack growing, which is usually not the case under mixed mode conditions in homogeneous materials. Experiments show that cracks propagate such that pure mode I condition are maintained at the crack tip. Thus, they grow by changing direction to establish a mode I condition. Therefore, further criteria have been developed based on e. g.

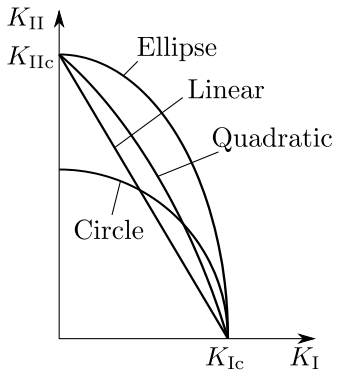

Figure 2.5: Mix mode fracture criterion.

maximum hoop-stress, maximum shear stress, maximum energy release rate and minimum strain energy density. Further details can be found in [3, 64]. Additional considerations have to be made when dealing with interface cracks, which is detailed in Sec. 2.2.5.

Energetic Criterion

Griffith derived an energetic crack initiation criterion as [31]

$$\frac{dU}{dA} - \frac{dW}{dA} = \frac{dV}{dA} \,, \tag{2.14}$$

where $\frac{dU}{dA}$ is the elastic strain energy per unit crack area that is released by crack extension, $\frac{dW}{dA}$ is the work to create new surface per unit crack area and $\frac{dV}{dA}$ is a energy type expression which can be used to describe the crack growth.

In terms of the potentials and with unit thickness Eq. (2.14) can be expressed as

$$\frac{d(\Pi^i + \Pi^e)}{da} + \mathscr{G}_{\mathrm{c}} \begin{cases} > 0 & \text{no growth} \\ = 0 & \text{equilibrium growth} \\ < 0 & \text{non-equilibrium growth} \end{cases} . \tag{2.15}$$

With Eq. (2.8) this indicates that the fracture criterion reads

$$\mathscr{G}_{\mathrm{I}} = \mathscr{G}_{\mathrm{Ic}} \,. \tag{2.16}$$

For mixed mode situations similar equations like those of the stress intensity factors exist,

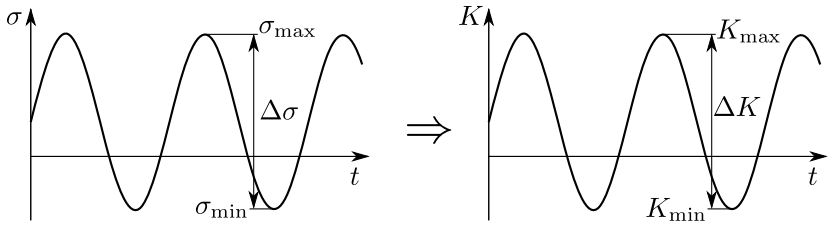

Figure 2.6: Variation of stresses and stress intensity factor.

e. g. a quadratic interaction criterion [69] reads

$$\left(\frac{\mathscr{G}_{\mathrm{I}}}{\mathscr{G}_{\mathrm{Ic}}}\right)^2 + \left(\frac{\mathscr{G}_{\mathrm{II}}}{\mathscr{G}_{\mathrm{IIc}}}\right)^2 + \left(\frac{\mathscr{G}_{\mathrm{III}}}{\mathscr{G}_{\mathrm{IIIc}}}\right)^2 = 1 \; . \tag{2.17}$$

Although it is possible to superimpose the strain energy release rates $\mathscr{G} = \mathscr{G}_{\mathrm{I}} + \mathscr{G}_{\mathrm{II}} + \mathscr{G}_{\mathrm{III}}$, the total critical strain energy release rate, $\mathscr{G}_{\mathrm{c}}(\psi)$, is a function of the mode mix and cannot be derived by superposition.

2.1.8 Fatigue crack growth

The following gives a very brief introduction into fatigue fracture in homogeneous elastic materials. Fatigue cracks grow due to cyclic deformation at the crack tip. This cyclic deformation is generally based on a cyclic loading $\Delta\sigma$. Similar to the LEFM (Eq. (2.1)) a variation of the stress intensity factor can be written as [19]

$$\Delta K = \Delta\sigma\sqrt{\pi a}\, Y \; , \tag{2.18}$$

where $\Delta\sigma = |\sigma_{\max} - \sigma_{\min}|$, and $\sigma_{\max}$ is the maximum stress and $\sigma_{\min}$ is the minimum stress acting (see Fig. 2.6).

In case of an applied cyclic stress with constant amplitude, ΔK can only change due to an increase of the crack length a. In general three regions are defined with fatigue crack growth, see Fig. 2.7. The basic boundaries of these regions are a threshold stress intensity factor range ΔK_{th} and a critical stress intensity factor range ΔK_{c}. For values below the ΔK_{th} no macroscopic crack propagation will take place. And if ΔK reaches ΔK_{c}, the maximum stress intensity factor $K_{\max}$ reaches K_{Ic} and thus the crack grows in an monotonic manner.

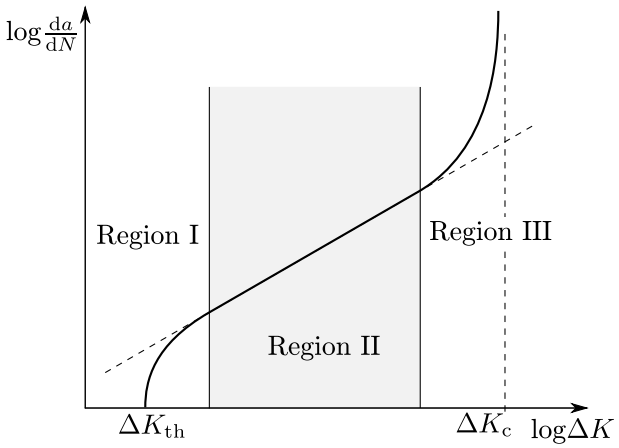

Figure 2.7: General $\frac{da}{dN}$ crack growth curve.

In the 1960s, Paris presented a propagation law which connects the crack extension velocity $\frac{da}{dN}$ with the stress intensity factor range ΔK. It reads

$$\frac{da}{dN} = C\Delta K^m \,, \tag{2.19}$$

where C and m are empirical constants and N is the number of load cycles. This famous Paris-law applies for an intermediate area of ΔK (region II). For ΔK values near the boundaries (region I and III) the Paris-law predicts bad results (see Fig. 2.7) therefore for these areas different equations have to be used, e. g. Foreman equation [41].

Paris' law is excessively used to predict lifetime in crack bearing structures and to define appropriate service intervals. By integration of Eq. (2.19) and using Eq. (2.18) the critical number of load cycles N_c can be predicted by

$$N_c = \frac{1}{C\Delta\sigma^m} \int_{a_i}^{a_c} \frac{d\tilde{a}}{\left(\sqrt{\pi\tilde{a}}\, Y\right)^m} \,, \tag{2.20}$$

where a_i is the initial crack length and a_c is the critical crack length.

It is possible to apply the Paris-law to interface cracks. This is often achieved by setting the constants C and m dependend of the mode-mix [52]. There exist several papers dealing with fatigue in interfaces [36, 48].

2.2 Interface fracture mechanics

There are lots of engineering applications which require one material to be bonded to another. These bi-material interfaces undergo complex failure modes. They experience stress intensification from geometric as well as material discontinuities. Due to this mismatch a crack tip is allways subjected to a mixed mode loading. Thus, the crack can propagate straight ahead under mixed mode loading along the interface or can kink out of the interface.

The following deals with linear elastic fracture mechanics on interface cracks between dissimilar isotropic solids. Nonlinear effects are limited to a small zone around the crack tip and can be neglected. Furthermore, no contact and no friction between the crack faces is assumed. The elastic materials are described by Young's moduli, $E^{(k)}$, Possion ratio, $\nu^{(k)}$ and the resulting shear moduli $\mu^{(k)}$ where $k = \{1, 2\}$ indicates the material.

2.2.1 Introduction

The first complete analytical solution of the stress field around a bi-material crack tip was given by Williams 1959 [9] and Erdogan 1963 [14]. These elastic solutions indicate a stress and displacement oscillation in addition to the $\frac{1}{\sqrt{r}}$ singularity in the vicinity of the crack tip. This displacement oscillation causes the crack faces to overlap each other which is physically inadmissible. Therefore, several papers, e. g. [10], introduce contact between the crack faces or apply material plasticity to get rid of these overlaps. For many practical applications the overlapping zone is very small and can be neglected in many cases [50]. However, there are situations where the region of oscillations are physically relevant. Such situations result from significant shear loads.

In the field of interface fracture mechanics different zones around the crack tip are introduced.

Fracture process zone – based on the assumption of LEFM the process zone is suppost be neglectable small.

Oscillation zone – as mentionend before, in general, the oscillation zone is very small compared to the crack length and is therefore often neglected. The size of the overlapping zone can be estimated as will be treated later.

***K* dominated zone** – all fracture mechanics equations are dealing with the conditions in the K dominated zone. This zone dominates until the effect of higher order terms cannot be neglected any more.

Outer zone – in this zone the higher order terms take a major part in the stress and displacement fields. Basic fracture mechanics methods are not applicable since the $\frac{1}{\sqrt{r}}$ singularity has lost its dominance and the assumptions lead to wrong results.

2.2.2 Stress and displacement field

Similar to a crack in homogeneous material the stress and displacement field in the vicinity of the crack tip can be described by stress intensity factors.

By means of the Dundur's parameters,

$$\alpha = \frac{E^{(1)\prime} - E^{(2)\prime}}{E^{(1)\prime} + E^{(2)\prime}} , \quad \beta = \frac{\mu^{(1)}(\kappa^{(2)} - 1) - \mu^{(2)}(\kappa^{(1)} - 1)}{\mu^{(1)}(\kappa^{(2)} + 1) + \mu^{(2)}(\kappa^{(1)} + 1)} , \tag{2.21}$$

the bi-material constant can be defined as

$$\varepsilon = \frac{1}{2\pi} \ln\left(\frac{1-\beta}{1+\beta}\right) . \tag{2.22}$$

Here k denotes to the respective material and

$$\kappa^{(k)} = 3 - 4\nu^{(k)} , \qquad E^{(k)\prime} = \frac{E^{(k)}}{1 - \nu^{(k)\,2}} , \qquad \text{for plane strain,} \tag{2.23}$$

and

$$\kappa^{(k)} = \frac{3 - \nu^{(k)}}{1 + \nu^{(k)}} , \qquad E^{(k)\prime} = E^{(k)} , \qquad \text{for plane stress.} \tag{2.24}$$

Dundur's α implies the mismatch in plane tensile modulus across the interface whereas β is a mismatch in the in-plane bulk modulus [22]. The absolute value of β can reach values up to $|\beta| \leq 0.5$. The limits of the bi-material parameter reads $|\varepsilon| \leq 0.175$. Note that the critical interface in the semiconductor problem between die attach and mould compound show a bi-material constant of $\varepsilon_{\mathrm{MC/DA}} = 0.0315$.

Based on Rice's complex stress intensity factor of classical type [50] the stress field in the

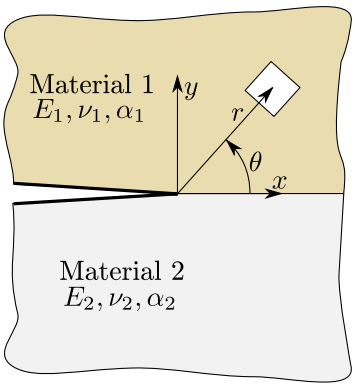

Figure 2.8: Crack in the interface of two materials.

vicinity of the crack tip is given as

$$(\sigma_{yy} + \mathrm{i}\sigma_{xy})_{\theta=0} = \frac{K_1 + \mathrm{i}K_2}{\sqrt{2\pi r}} \left(\frac{r}{l}\right)^{\mathrm{i}\varepsilon} , \tag{2.25}$$

where $\mathrm{i} = \sqrt{-1}$, θ and r are the cylindrical coordinates of the considered point (see Fig. 2.8), K_1 and K_2 are the components of the complex stress intensity factor (as discussed later) and l is an arbitrary reference length. This reference length is used to normalize the distance from the crack tip. Typically l is set to a fixed length, e. g. the crack length or uncracked ligament width.

The oscillation (see Fig. 2.9) of Eq. (2.25) can be revealed by using Euler's formula

$$r^{\mathrm{i}\varepsilon} = \cos(\varepsilon \ln r) + \mathrm{i}\sin(\varepsilon \ln r) . \tag{2.26}$$

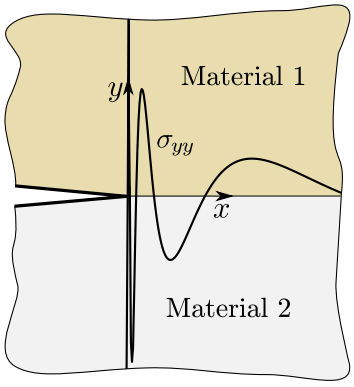

Figure 2.9: Stress distribution σ_{yy} of an interface crack at $\theta = 0$.

The displacement jumps for $\theta = \pm\pi$ can be expressed as [22]

$$\Delta u_y + \mathrm{i}\Delta u_x = 8\frac{K_1 + \mathrm{i}K_2}{(1+2\mathrm{i}\varepsilon)E^* \cosh(\varepsilon\pi)} \left(\frac{r}{2\pi}\right)^{1/2} \left(\frac{r}{l}\right)^{\mathrm{i}\varepsilon} , \tag{2.27}$$

where the average Young's modulus E^* is defined as

$$\frac{1}{E^*} = \frac{1}{2}\left(\frac{1}{E^{(1)\prime}} + \frac{1}{E^{(2)\prime}}\right) . \tag{2.28}$$

Here again the oscillation term $r^{\mathrm{i}\varepsilon}$ shows up and leads to the ambiguous crack face overlapping. Rice [50] presented a way to assess the size of the contact or oscillation zone as

$$r_\mathrm{c} = l \, \exp\left(\frac{-(\psi + \pi/2)}{\varepsilon}\right) , \tag{2.29}$$

where ψ is the mode mix.

For moderate values of the mode mix, the contact zone is neglectable small, but it may increase dramatically with rising mode mix. Rice stated that $r_\mathrm{c}/l < 0.01$ may a suitable restriction for small scale contact zone concept. Thus, for validity of LEFM approach one gets $|\psi| < 82°$ for $\varepsilon = \varepsilon_{\mathrm{MC/DA}}$.

2.2.3 Fracture parameters

Complex stress intensity factor

The real and imaginary part of the complex stress intensity factor, $\tilde{K} = K_1 + \mathrm{i}K_2$, play a similar role than the conventional mode I and mode II in homogeneous problems. If one assumes that $\beta = 0$, [22], they play precisely the same role since the normal and shear displacements of the crack faces are decoupled. In general ($\beta \neq 0$), this decoupling does not occur. Due to the oscillation term even a pure mode I loading leads to shear stresses at the crack tip, hence, the stress intensity factor parts are inherently coupled.

In Eq. (2.25) the complex stress intensity factor of classical type is used. With this formulation the stress intensity factor has the dimension $\mathrm{Pa}\sqrt{\mathrm{m}}$ equal to that of the homogeneous one. There exist other definitions of the complex stress intensity factor, e.g. Hutchinson et al. [23] introduce the stress field around the interface crack tip as

$$(\sigma_{yy} + \mathrm{i}\sigma_{xy})_{\theta=0} = \frac{K_{\mathrm{h}1} + \mathrm{i}K_{\mathrm{h}2}}{\sqrt{2\pi r}} r^{\mathrm{i}\varepsilon} . \tag{2.30}$$

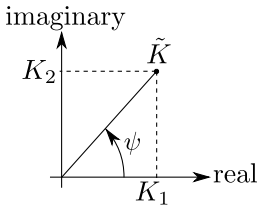

Figure 2.10: Complex stress intensity factor and mode mix.

This formulation assigns a dimension of $\mathrm{Pa}\sqrt{\mathrm{m}}\,\mathrm{m}^{\mathrm{i}\varepsilon}$ to the stress intensity factor $\tilde{K_{\mathrm{h}}} = K_{\mathrm{h1}} + \mathrm{i}K_{\mathrm{h2}}$, which is inconvenient for engineering application. Both definitions are essentially identical and can be linked by

$$\tilde{K} = \tilde{K_{\mathrm{h}}}\, l^{\mathrm{i}\varepsilon} \,. \tag{2.31}$$

The modulus of $\tilde{K}$ is an often used parameter to describe the crack. It is independent of l and defined as

$$K^{\mathrm{e}} = \sqrt{K_1^2 + K_2^2} \,. \tag{2.32}$$

Mode mix

As introduced in Sec. 2.1.5 the mode mix describes the ratio of mode II stress intensity factor to mode I stress intensity factor. With interface fracture mechanics the components of the complex stress intensity factor are not fully associated with the opening modes like in the homogeneous case. Still a mode mix can be defined as (see Fig. 2.10)

$$\tan\psi = \frac{K_2}{K_1} \,, \tag{2.33}$$

which is equivalent to

$$\tan\psi = \left(\frac{\sigma_{xy}}{\sigma_{yy}}\right)_{r=l} \,. \tag{2.34}$$

Since the stress intensity factors K_1 and K_2 are dependend on the reference length l, the mode mix is an l-dependend measure of the fracture mode mix. If the value l is changed to l' the mode angle is shifted as [22]

$$\psi' = \psi + \varepsilon \ln\frac{l'}{l} \,. \tag{2.35}$$

There exist different types of mode mixes [1]. When using the definition of Hutchinson

et al. [23] the associated mode mix is

$$\tan\psi_h = \frac{K_{\mathrm{h}2}}{K_{\mathrm{h}1}} \,, \tag{2.36}$$

and it is again linked with its counterpart as

$$\psi = \psi_{\mathrm{h}} + \varepsilon \ln l \,. \tag{2.37}$$

Furthermore, it is possible to introduce an energy release rate based mode mix definition

$$\tan^2\psi_G = \frac{\mathscr{G}_2}{\mathscr{G}_1} \,. \tag{2.38}$$

This definition has to be taken with care since the energy release rate components vary with da (different crack extensions Δa) as will be discussed below. If one applies $\beta = 0$ then $|\psi| = \psi_G$. Agrawal and Karlsson [1] presents further definitions and gives connections between them. Mantič and París [35] deals with energy release rate based mode mixities more in detail.

Energy release rate

The energy release rate for interface cracks is defined in the same way as for homogeneous conditions (Eq. (2.8)). According to Eq. (2.12), in a mixed mode situation the energy release rate can be divided into mode I and mode II contributions. Due to the oscillation of the stress and displacement field these components also oscillate with different crack extensions Δa (see Fig. 2.11). Qian and Sun [46] presented analytical solutions for $\mathscr{G}_1$ and $\mathscr{G}_2$ as

$$\mathscr{G}_{1,2} = \frac{1}{2}\mathscr{G} \pm \frac{C|\tilde{B}|\mathscr{G}}{D}\left[\cos(\zeta-\chi)\cos\left(2\varepsilon\ln\frac{\Delta a}{4a}\right) + \sin(\zeta-\chi)\sin\left(2\varepsilon\ln\frac{\Delta a}{4a}\right)\right] \,, \tag{2.39}$$

where C, $\tilde{B}$, D, ζ, and χ are related to material properties and mode mixity.

The total energy release rate $\mathscr{G} = \mathscr{G}_1 + \mathscr{G}_2$ converges and can be linked with the complex stress intensity factor by

$$\mathscr{G} = \frac{1-\beta^2}{E^*}|\tilde{K}|^2 \,. \tag{2.40}$$

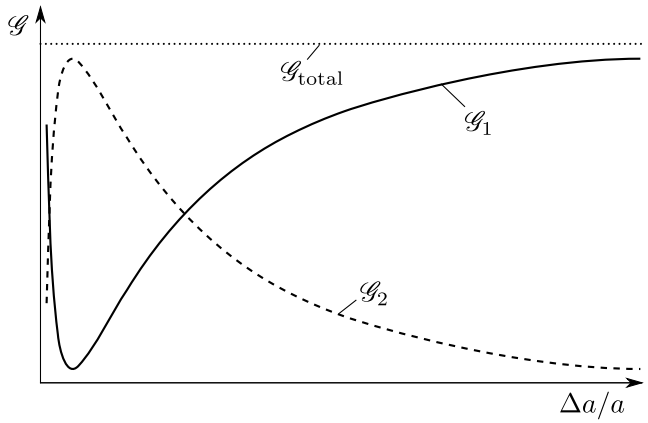

Figure 2.11: Dependence of computed energy release rate on the crack extension at the crack tip, after [63].

2.2.4 Fracture toughness

To predict crack initiation and propagation interface toughness values have to be measured. Similar to the homogeneous case different types of specimen and test set-up configurations were presented [18, 54, 66]. The main difference and at the same time main problem between homogeneous and interface situations is the strong dependence of the interface toughness values on the mode mix. Furthermore, since the crack tip experiences shear stresses even if pure tensile stresses are applied to the specimen, the correct determination of mode mix and fracture toughness is a tricky problem. Recent works usually perform a FEM-calculation simultaneous to the experiment to evaluate the actual mode mix. Due to the l-dependency of the mode mix the reference length has to be supplied with the toughness values.

Another basic problem is the creation of "infinitely" sharp crack tips. This is important to make sure where the crack initiates and to establish the correct $\frac{1}{\sqrt{r}}$ singularity for the FEM-calculation. Different methods are used like, e. g., initiation through a small weak layer which generally leads to blunted crack tips [70], razor blade peeling as done witch notched bar impact tests or fatigue initiated cracks.

2.2.5 Fracture criterion

When dealing with interfaces a mode-mix situation takes place in general and crack kinking like with homogeneous materials will occur just in special cases. Thus, the fracture criteria as introduced in section 2.1.7 can be used to classify the crack. As seen before at least two

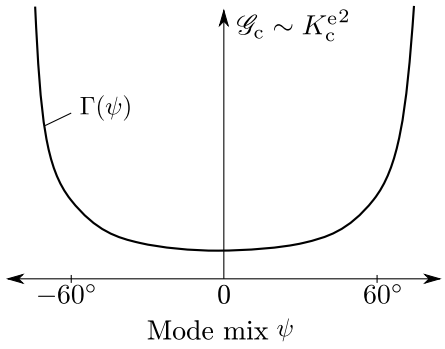

Figure 2.12: Energy release based fracture criterion.

interface toughness (K_{Ic} and K_{IIc}) values have to be defined and an appropriate fracture locus must be chosen. In general, it is very hard to obtain enough interface toughness data to define the correct fracture envelope.

A more common interface fracture criteria is the energetic approach. Here the critical interface toughness is defined as a function of the mode mix (see Fig. 2.12)

$$\mathscr{G} = \Gamma(\psi) \ . \tag{2.41}$$

In this context Hutchinson and Suo [22] have given two criteria for the simplified assumption of $\beta = 0$ which implies $\varepsilon = 0$ as

$$\Gamma(\psi) = \mathscr{G}_1^c \left(1 + \tan^2\left[(1-\lambda)\psi\right]\right) \ , \quad \text{or} \quad \Gamma(\psi) = \mathscr{G}_1^c \left(1 + (1-\lambda)\tan^2\psi\right) \ , \tag{2.42}$$

where λ adjusts the influence of the mode II contribution and $\mathscr{G}_1^c$ is the pure mode I toughness. Experimental results are necessary to choose the appropriate function.

For $\beta \neq 0$ Hutchinson and Suo [22] also presented a criteria in the form

$$\mathscr{G} = \Gamma(\psi, l) \tag{2.43}$$

There are several other interface fracture criteria defined, e. g., critical hoop stress criterion [64] or critical shear stress criterion. Banks-Sills and Ashkenazi [3] applied these criteria and compared them with the energy release rate criteria.

As mentioned before another issue with interface fracture is crack kinking out of the interface. Due to a mixed mode situation cracks tend to change direction to propagate in pure mode I. Especially in homogeneous materials this effect can be seen [71]. For typical

material combinations and bonding processes the interface toughness is lower than the toughness of the respective materials alone. Hence, interface cracks tend to grow in mixed mode condition along the interface. The interface toughness exhibits a strong dependency on the mode mix ψ, see Fig. 2.12. Thus, with increasing mode mix the interface toughness grows with respect to the bulk material toughness, until crack kinking occurs. Hutchinson and Suo [22] stated that kinking will be favored over continued interface cracking if

$$\frac{\mathscr{G}}{\mathscr{G}^{\mathrm{t}}_{\max}} < \frac{\Gamma(\psi)}{\mathscr{G}_{\mathrm{Ic}}} , \tag{2.44}$$

where $\mathscr{G}^{\mathrm{t}}_{\max}$ is the maximal energy release rate at the kinked crack tip and $\mathscr{G}_{\mathrm{Ic}}$ is the mode I toughness of the adjacent material.

2.2.6 Tri- and multi-material interfaces

Several researcher have focused their attention torwards the stress singularity field at tri- or multi-material junctions, e. g. [5, 46, 8]. But so far no fracture mechanics based treatise could be found in the open literature by the author. Shkarayev et al. [55] presented an interface approaching a multi-material junction but could not give equations for energy release rates or stress intensity factors.

2.3 Numerical fracture mechanics with FEM

2.3.1 Crack tip elements

Common 4- or 8-noded isoparametric elements do not offer special ability to represent singular points. Thus, they show a bad behavior when used to calculate stresses and displacements at a singularity. Hence, a common workaround is to use a very fine mesh around the singularity and skip the first few elements when interpreting the results.

A different approach is to include the singular behavior into the element formulation. With this idea in mind a few element types were created, which completely surround the crack tip and can establish an appropriate singularity [33]. The most common type of these singular elements is a collapsed and distorted 8-noded isoparametric element—the crack tip element. Every FEM-package with implemented 8-noded isoparametric elements is capable of using this singular element without any need of programming additional code.

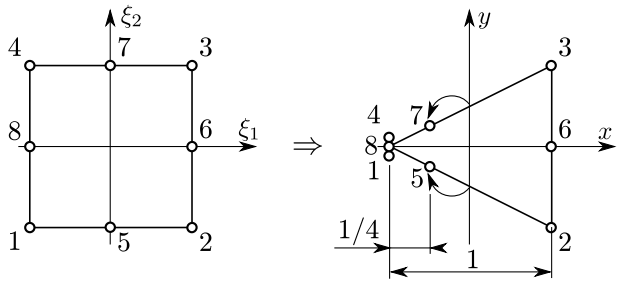

Figure 2.13: Transformation of a 8-noded isoparametric element (left) into a collapsed and distorted crack tip element (right).

The collapse and distortion is shown in Fig. 2.13. A collapse of one side (Nodes 1, 8, and 4) into a single point and a shifting of the midside nodes (Nodes 5 and 7) to the quarter point position leads to the following strains

$$\varepsilon_{11} = \frac{b_0}{r} + \frac{e_1}{\sqrt{r}} + e_2 \ , \tag{2.45}$$

$$\varepsilon_{22} = \frac{d_0}{r} + \frac{d_1}{\sqrt{r}} + d_2 \ , \tag{2.46}$$

$$\varepsilon_{12} = \frac{b_0 + d_0}{r} + \frac{f_1}{\sqrt{r}} + f_2 \ . \tag{2.47}$$

Here r is the radial distance from the singular point and the constants b_0, d_0, d_1, d_2, e_1, e_2, f_1, and f_2 depend on the actual node displacements and the normalized coordinate ξ_2. If the collapsed nodes are kinematically coupled, the constants b_0 and d_0 become zero and the strong $\frac{1}{r}$ singularity vanishes, revealing the desired $\frac{1}{\sqrt{r}}$ singularity. A complete derivation of this behavior can be found e. g. in [33].

It can be shown that all radius rays possess this $\frac{1}{\sqrt{r}}$ behavior [33] and therefore the angular distribution of the stresses and strains can be obtained by arranging multiple elements in a fan-shaped structure around the crack tip (e. g. Fig. 2.14, Note: Here the crack faces are shown in an opened stage for clarity purposes. A crack is always modeled with the crack faces touching each other, otherwise the crack would become a notch with a different type of singularity see, e. g. [55, 5]).

2.3.2 Numerical methods

The following gives a brief introduction in a few methods within the FEM used to calculate fracture mechanic parameters or fracture propagation.

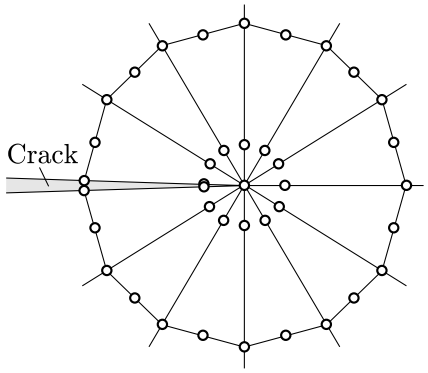

Figure 2.14: Singular elements arranged in a fan-shaped structure around the crack tip.

Displacement extrapolation method

The displacement extrapolation method (DE) is based on the analytical expressions of the crack face displacements according to a certain stress intensity factor, $\underset{\sim}{\boldsymbol{u}} = \mathrm{f}(K_i, r)$ with $i = \{\mathrm{I}, \mathrm{II}\}$, in an inverse manner. The displacements are taken at different locations along the crack faces and the associated stress intensity factors are extrapolated onto the crack tip as

$$K_i = \mathrm{g}(\underset{\sim}{\boldsymbol{u}}, r), \quad i = \{\mathrm{I}, \mathrm{II}\} \; . \tag{2.48}$$

By means of the FEM-method the displacements $\underset{\sim}{\boldsymbol{u}}$ can be predicted and with the transformed function g, the stress intensity factors can be obtained [72, 20]. This method was used by various other researchers in the field of semiconductor devices, e. g. [62].

Stress extrapolation method

Similar to the displacement extrapolation method the stress extrapolation method applies the analytical solution of the stress field in the vicinity of a crack tip $\underset{\sim}{\boldsymbol{\sigma}} = \mathrm{h}(K_i, r)$ to calculate the underlying stress intensity factor as [72]

$$K_i = \mathrm{m}(\underset{\sim}{\boldsymbol{\sigma}}, r), \quad i = \{\mathrm{I}, \mathrm{II}\} \; . \tag{2.49}$$

The obtained results are inaccurate compared to those of the displacement extrapolation method since the stresses are already extrapolated to the nodes by the finite element code.

Displacement ratio method

The Displacement ratio method [60] uses the ratio $\frac{\Delta u_y}{\Delta u_x}$ to calculate $\frac{K_{\mathrm{II}}}{K_{\mathrm{I}}}$ (this denotes the mode mix) without any extrapolation procedure. Thus another fracture mechanics method is necessary to obtain the complete stress intensity factor. Its accuracy depends on the chosen distance r and is strongly influenced by the mesh size.

Crack closure technique

The crack closure technique is based on Irwin's crack closure integral. It is an energy based method, hence, it calculates a scalar quantity—the energy release rate $\mathscr{G}$. The basic assumption is that the energy released when the crack extends by Δa is identical to the energy required to close the crack by this length.

$$\mathscr{G} = \lim_{\Delta a \to 0} \frac{\Delta W}{\Delta a \cdot 1} \tag{2.50}$$

The energy release rate is equal to the work ΔW necessary to close a crack over a certain crack length Δa divided by this crack closure length. For reasonable fine mesh sizes the limes can be dropped.

Similar to the displacement ratio method only one scalar quantity is obtained. Thus, an additional method or an enhanced crack closure technique is necessary.

Two-step crack closure technique – The original crack closure integral needs two simulation runs. One simulation run to establish the forces at the crack tip and another with changed crack size to get the displacements on the former crack tip position (see Fig. 2.15). With these two quantities the work and consequently the energy release rate can be computed.

Virtual crack closure technique – In most of the cases the virtual crack closure technique is used instead of the two-step crack closure technique since only one simulation is needed.

As an approximation it is possible to use the forces directly at the crack tip and the displacement behind the crack tip. This implies the assumption that the state at the crack tip does not alter significantly during crack growth. Thus, only one simulation run

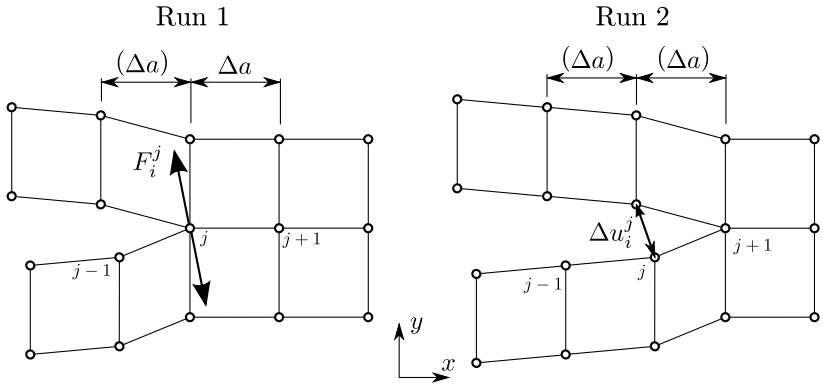

Figure 2.15: 2 step crack closure technique applied to linear 4-noded elements.

is necessary. This, as virtual (or modified) crack closure technique (VCCT, MCCI) known method is used very successfully to compute the energy release rates within the FEM

Virtual crack extension

The virtual crack extension method (VCE) uses a similar approach as the crack closure method to calculate the energy release rate. The crack tip node or a defined area around the crack tip is shifted by the crack extension Δa and the change of the potential energy is determined (see Fig. 2.16). This change can also be expressed as

$$\mathscr{G} = -\frac{d\Pi}{da} \approx -\frac{1}{2}\underset{\sim}{\boldsymbol{V}}^T \frac{\Delta \underset{\approx}{\boldsymbol{K}}}{\Delta a}\underset{\sim}{\boldsymbol{V}} \ , \tag{2.51}$$

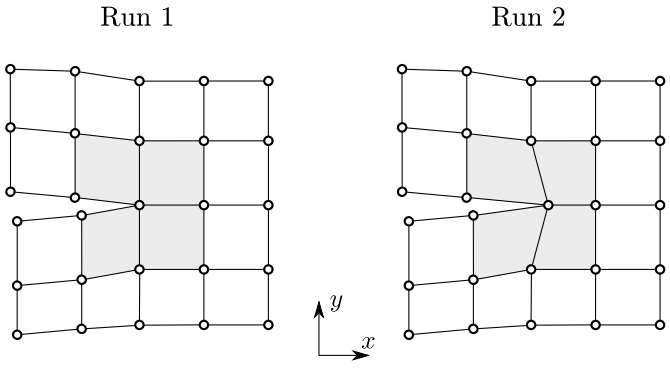

Figure 2.16: Virtual crack extension method applied to linear 4-noded elements with a possible subregion shaded in gray.

where $\underset{\sim}{\boldsymbol{V}}$ is the global vector of the nodal degrees of freedom, and $\frac{\Delta \underset{\approx}{\boldsymbol{K}}}{\Delta a}$ is the change of the stiffness matrix with respect to the crack extension Δa. Thus, the virtual crack extension method is also known as stiffness derivative method.

To save computation effort it is possible to consider only a subregion of relevant elements around the crack tip (see Fig. 2.16) Since two separate simulation runs are needed the VCE is in the majority of cases rejected and replaced by the VCCT. For additional information see [33].

J-Integral

The original definition of the J-integral by Rice [49] refers to a two-dimensional problem of a homogeneous body of linear or non-linear elastic material. Furthermore, this body is free of body forces, thermal loads and initial strains. Rice showed that the rate of the potential energy due to an infinitesimal crack extension is given by

$$-\frac{\partial \Pi}{\partial a} = \iint_A \frac{\partial W}{\partial a}\, dx\, dy - \int_\Gamma \sigma_{ij} \frac{\partial \underset{\sim}{\boldsymbol{u}}}{\partial a} n_x\, ds\ . \tag{2.52}$$

Here W is the strain energy density, defined as

$$W = \int_\varepsilon \sigma_{ij}\, d\varepsilon_{ij}\ , \tag{2.53}$$

σ_{ij} is the stress tensor, ε_{ij} is the strain tensor. Moreover, $\underset{\sim}{\boldsymbol{u}}$ is the displacement vector, Γ is an arbitrary path, starting at a crack face and moving counter-clock wise to the other crack face, see Fig. 2.17, and $\vec{n}$ is the normal vector of Γ. Choosing a coordinate system with the origin in the crack tip and its x-axis pointing into the uncracked area Eq. (2.52)

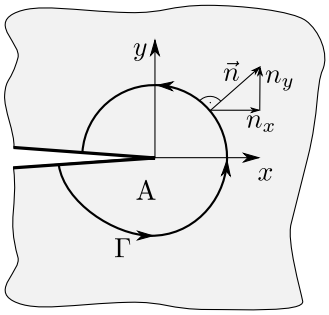

Figure 2.17: Definition of J-integral as line integral around crack tip.

can be expressed as [39]

$$-\frac{\partial \Pi}{\partial a} = \int_{\Gamma} W\, dy - \int_{\Gamma} \sigma_{ij} \frac{\partial \underset{\sim}{\boldsymbol{u}}}{\partial x} n_x\, ds \stackrel{\downarrow}{=} J\ , \tag{2.54}$$

where $-\frac{\partial \Pi}{\partial a}$ is known as the J-integral. It can be shown that the J-integral is independent of the chosen path, therefore it is possible to obtain the information regarding the stress and strain state around the crack at some distance of the crack tip without dealing with the stress singularity. Due to the applied assumptions during the derivation the derived J-integral can be applied to cracks in non-linear elastic or, under certain restrictions, plastic materials [33]. Furthermore, Eq. (2.54) can be extended to account for body forces, or initial strains and three-dimensional problems. In terms of linear elastic materials the J-integral reduces to the strain energy release rate $\mathscr{G}$ [39].

For the case of interface fracture mechanics additional considerations have to be made. The J-integral (Eq. (2.54)) is not capable of calculating the mode mix in a mixed mode situation. If Eq. (2.54) is written for a crack extension in y-direction a second set of equations can be derived. This approach is known as the J_k-integral technique. The integral J_k for $k = \{1, 2\}$, can be expressed as [27]

$$J_k = \lim_{\rho \to 0} \int_{\Gamma_\rho} (W n_k - \sigma_{ij} u_{i,k} n_j)\, d\Gamma, \quad k = \{1, 2\}\ , \tag{2.55}$$

where ρ is the radius of the inner path around the crack tip (see Fig. 2.18) With these two equations the stress intensity factors K_1 and K_2 can be derived as presented in [27].

The J_k-integral can be extended to deal with thermal problems [28] with the aid of the body-force-analogy [6]. The so developed conservative J_k-Integral uses the Duhamel Neumann constitutive equation which is a transformed version of the linear elastic law of Hook. Therefore, the advantage of the J-Integral as being independent of any material law is lost. The J_k-Integral is only applicable to linear elastic problems.

$$J_1 = \int_{\Gamma_0} (W_F n_1 - \sigma_{ij} u_{j,1} n_i)\, d\Gamma + \sum_{k=1}^{2} \beta^{(k)} \int_{A_k} \theta_{,1} \varepsilon_{ii}\, dA \tag{2.56}$$

$$\begin{aligned} J_{2\rho} = &\int_{\Gamma_0} (W_F n_2 - \sigma_{ij} u_{j,2} n_i)\, d\Gamma + \int_{\Gamma_c^+ + \Gamma_c^-} W_F n_2\, d\Gamma \\ &+ \int_{\Gamma_l^+ + \Gamma_l^-} (W_F - \sigma_{j2} u_{j,2}) n_2\, d\Gamma + \sum_{k=1}^{2} \beta^{(k)} \int_{A_k} \theta_{,2} \varepsilon_{ii}\, dA \end{aligned} \tag{2.57}$$

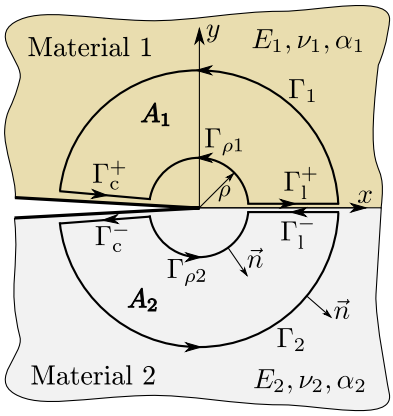

Figure 2.18: Integration path Γ for J_k-integral in a bi-material interface.

where

$$\begin{aligned} \beta &= \frac{E\alpha}{1-2\nu} \quad \text{for plane strain ,} \\ \beta &= \frac{E\alpha}{1-\nu} \quad \text{for plane stress ,} \end{aligned} \tag{2.58}$$

and the used pathes are plotted in Fig. 2.18 with $\Gamma_0 = \Gamma_1 + \Gamma_2$.

The expressions of J_1 and J_2 can be written as [27]

$$J_1 = \left[\frac{1+\kappa^{(1)}}{16\mu^{(1)}} + \frac{1+\kappa^{(2)}}{16\mu^{(2)}} \right] (K_1^2 + K_2^2) \,, \tag{2.59}$$

$$\begin{aligned} J_{2\rho} = &- \frac{1}{32\pi\varepsilon} \left[\frac{1+\kappa^{(1)}}{\mu^{(1)}} (1 - \mathrm{e}^{-2\pi\varepsilon}) + \frac{1+\kappa^{(2)}}{\mu^{(2)}} (\mathrm{e}^{-2\pi\varepsilon} - 1) \right] \\ &\cdot \left[(K_1^2 - K_2^2) \sin 2\varepsilon \log\rho + 2K_1 K_2 \cos(2\varepsilon \log\rho) \right] \,. \end{aligned} \tag{2.60}$$

With this set of equations K_1 and K_2 can be derived.

There exist several other variations of the J-integral like a combination of the J-integral and the superposition method known as the M-integral method [29] or the Interaction-Integral [33].

Cohesive zone elements

The idea behind the cohesive zone model is that the damage and separation during a fracture process only takes place in a small region in front of the crack tip [4, 43, 33]. In

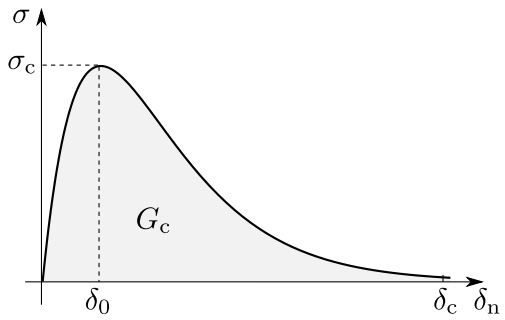

Figure 2.19: Traction-separation law by Needleman [43].

this zone only a certain amount of energy (G_c) can be dissipated until it looses its cohesion. The foundation of all cohesive materials is the traction-separation law. It describes the tractions acting due to certain separations between the two crack faces. Different types of traction-separation laws were developed for various types of materials (brittle, ductile). A common model for brittle metals, developed by Needleman [43], takes an exponential form like Eq. (2.61) (see Fig. 2.19).

$$\sigma(\delta_n) = \frac{G_\mathrm{c}}{\delta_0}\frac{\delta_\mathrm{n}}{\delta_0}\exp\left(-\frac{\delta_\mathrm{n}}{\delta_0}\right) , \qquad G_c = \mathrm{e}\,\sigma_\mathrm{c}\delta_0 , \tag{2.61}$$

where G_c is the dissipated work during fracture, σ is the traction, and δ_n is the separation (crack face displacement) respectively. The three essential properties σ_c, G_c and δ_c should be determined by means of experiments. Here σ_c and δ_0 can be derived of the rupture stress, and δ_c is obtained of the fracture process zone [33]. When dealing with LEFM there is a connection with the fracture parameters $G_\mathrm{c} \mathrel{\widehat{=}} \mathscr{G}_\mathrm{Ic}$. Where $\mathscr{G}_\mathrm{Ic}$ is the critical energy release rate for mode I, connected with the fracture toughness as given by Eq. (2.9). A similar relation can also be made in the field of elasto-plastic fracture mechanics (EPFM) [33].

A traction-separation law can also given for mode II and mixed mode situations [33].

In FEM the cohesive zone elements are intrinsically a form of damage behavior elements rather than a fracture mechanics method. Actually, the fracture mechanics data is needed to set up the cohesive zone element, e. g. $\mathscr{G}_\mathrm{Ic}$. Cohesive zone elements gain a lot of attention when it comes to the task of crack initiation and propagation (in homogeneous materials or interfaces). They have to be placed between the elements forming the expected (and designated) crack path, and when the dissipated energy in the element exceeds a certain value the element looses its cohesion. Their big advantage is that they can be used together with non-linear materials (visco-plastic) and for fatigue analysis or dynamic

fracture analysis without special considerations.

Even though there are big advantages, a few drawbacks also exist. Cohesive zone elements cannot be used to classify a crack if no material data is available. Another major issue is that in general it is very hard to know the crack paths in advance and since it is necessary to position the cohesive zone elements there is always some uncertainty left [12]. Furthermore, there is the need of a non-linear simulation with all the possible convergence problems and additional time consumption since a finer discretization is needed.

For further information see [33, 43, 13, 59, 11, 12, 45]. Special considerations of mixed mode situations can be found in [33, 17, 26, 30].

Chapter 3

Implemented fracture mechanics methods

Many state of the art Finite Element codes have a build in routine to compute stress intensity factors or energy release rates from the nodal displacements, J-integral, or VCCT. Unfortunately, most of these routines are focused on cracks in homogeneous materials. To apply displacement based stress intensity factor calculations to an interface crack, a different set of equations is necessary. Thus, the displacement extrapolation method was implemented from scratch in the present work. Furthermore, ANSYS has no build-in VCCT feature, hence this was implemented too. Both methods are written as postprocessing routines within the ANSYS APDL scripting language.

3.1 Displacement extrapolation method

As described in Sec. 2.3.2, the stress intensity factors are calculated from the nodal displacements of the crack faces. Here five positions along the crack face are used and the results are extrapolated onto the crack tip. A basic sketch of the implemented displacement extrapolation method is given in Fig. 3.1. It presents the crack face displacements used to assess corresponding stress intensity factors. These stress intensity factors are then extrapolated onto the crack tip.

In the following the displacement extrapolation method is presented for isotropic materials as well as orthotropic materials sharing an interface.

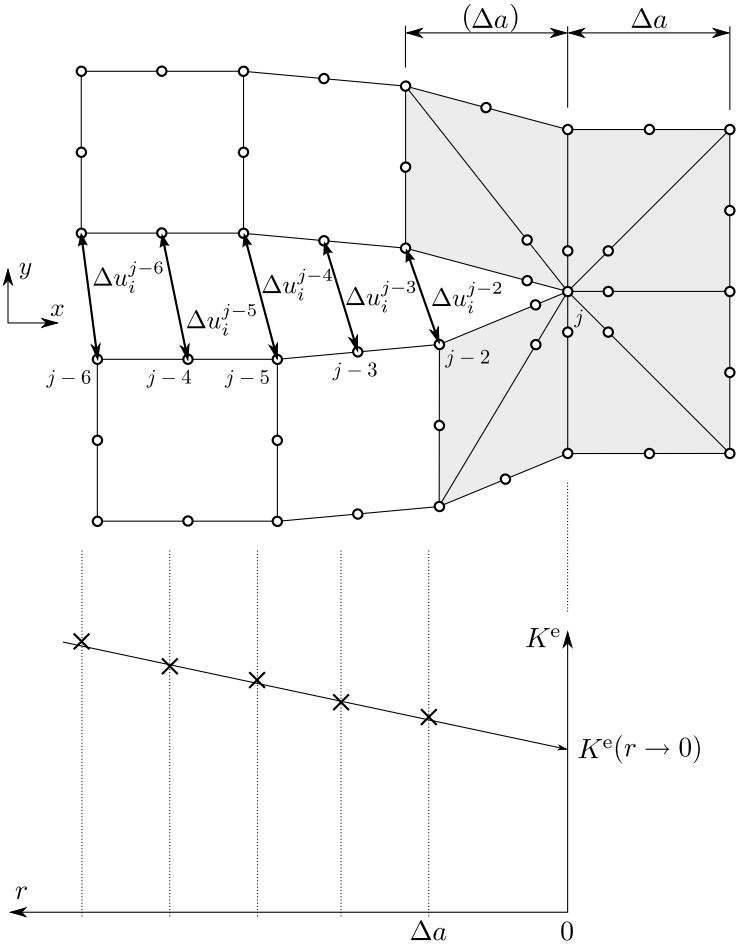

Figure 3.1: Sketch of the implemented displacement extrapolation method.

3.1.1 Isotropic materials sharing an interface

Following Yuuki and Cho [72] the displacement extrapolation method can be applied to interface cracks between two isotropic materials[1].

The relative displacements in the near tip region are given by [72] as

$$\Delta u_y + \mathrm{i}\Delta u_x = \frac{K_1 + \mathrm{i}K_2}{2(1+2\mathrm{i}\varepsilon)\cosh(\varepsilon\pi)} \left[\frac{\kappa^{(1)}+1}{\mu^{(1)}} + \frac{\kappa^{(2)}+1}{\mu^{(2)}} \right] \left(\frac{r}{2\pi}\right)^{1/2} \left(\frac{r}{l}\right)^{\mathrm{i}\varepsilon} , \tag{3.1}$$

where

$$\Delta u_j = u_j(r,\pi) - u_j(r,-\pi) , \qquad j = \{x, y\} . \tag{3.2}$$

[1] A note may be appropriate that there is a typo in equation (12) in [72].

After transformation of Eq. (3.1) the stress intensity factors can be expressed as [25]

$$K_1(r) = S\sqrt{\frac{2\pi}{r}}\left((\Delta u_y - 2\varepsilon\Delta u_x)\cos R + (\Delta u_x + 2\varepsilon\Delta u_y)\sin R\right) \ , \tag{3.3}$$

$$K_2(r) = S\sqrt{\frac{2\pi}{r}}\left(-(\Delta u_y - 2\varepsilon\Delta u_x)\sin R + (\Delta u_x + 2\varepsilon\Delta u_y)\cos R\right) \ , \tag{3.4}$$

with

$$S = \frac{2\cosh(\varepsilon\pi)}{(\kappa^{(1)}+1)/\mu^{(1)} + (\kappa^{(2)}+1)/\mu^{(2)}} \ , \qquad R = \varepsilon\ln\left(\frac{r}{l}\right) \ . \tag{3.5}$$

With Eq. (3.3) and Eq. (3.4) the stress intensity factors, K_1 and K_2, the norm K^{e}, and the mode mix, ψ, can be calculated at a certain distance r as

$$K^{\mathrm{e}}(r) = \sqrt{K_1(r)^2 + K_2(r)^2} \ , \tag{3.6}$$

$$\tan\psi(r) = \frac{K_2(r)}{K_1(r)} \ . \tag{3.7}$$

These values are extrapolated onto the crack tip to obtain the stress intensity factors and the mode mix

$$K^{\mathrm{e}} = \lim_{r\to 0} K^{\mathrm{e}}(r) \ , \tag{3.8}$$

$$\tan\psi = \lim_{r\to 0} \psi(r) \ . \tag{3.9}$$

3.1.2 Orthotropic materials sharing an interface

If at least one material of the interface pair shows an orthotropic behavior a different set of equations is necessary. Following Qian and Sun [46] it is possible to derive a displacement extrapolation method for orthotropic materials having one plane of symmetry parallel to x–y plane (see Fig. 3.2). Since the elasticity tensor exhibits 9 independent material constants a full set of properties have to be defined. $E_i^{(k)}$, $\nu_{ij}^{(k)}$, $\mu_{ij}^{(k)}$ with $i,j = \{x,y\}$, are the Young's moduli, the Poisson ratios and the shear moduli, respectively, with respect to the local coordinates. The superscript $(k) = \{1,2\}$ denotes to the upper and lower material. Due to the required symmetry

$$\frac{\nu_{ij}}{E_i} = \frac{\nu_{ji}}{E_j} \tag{3.10}$$

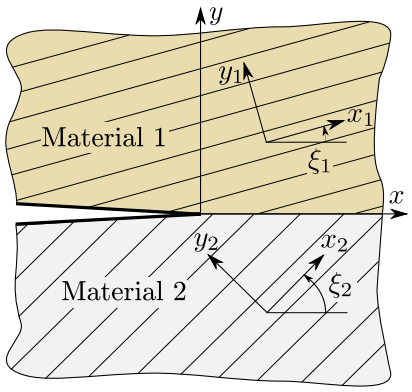

Figure 3.2: Interface crack between two orthotropic materials having one plane of symmetry parallel to x–y plane.

holds true (no Einstein notation). The elasticity tensor for each material can be written in the compact matrix form

$$\underset{\approx}{\boldsymbol{C}} = \begin{bmatrix} c_{11} & c_{12} & c_{13} & & & \\ & c_{22} & c_{23} & & \underset{\approx}{\mathbf{0}} & \\ \text{sym.} & & c_{33} & & & \\ & & & c_{44} & & \\ & \underset{\approx}{\mathbf{0}} & & & c_{55} & \\ & & & & & c_{66} \end{bmatrix} \tag{3.11}$$

with the corresponding vectors of stress and strain components

$$\sigma = \begin{bmatrix} \sigma_{11} \\ \sigma_{22} \\ \sigma_{33} \\ \sigma_{23} \\ \sigma_{13} \\ \sigma_{12} \end{bmatrix}, \quad \text{and} \quad \varepsilon = \begin{bmatrix} \varepsilon_{11} \\ \varepsilon_{22} \\ \varepsilon_{33} \\ 2\varepsilon_{23} \\ 2\varepsilon_{13} \\ 2\varepsilon_{12} \end{bmatrix}. \tag{3.12}$$

The engineering constants are related to the components c_{ij} for $i, j = \{1, 2\}$ by [7] as

$$c_{11} = E_1(1 - \nu_{yz}\nu_{zy}) \cdot \gamma \,, \tag{3.13}$$

$$c_{22} = E_2(1 - \nu_{xz}\nu_{zx}) \cdot \gamma \,, \tag{3.14}$$

$$c_{12} = E_1(\nu_{yx} - \nu_{zx}\nu_{yz}) \cdot \gamma \,, \tag{3.15}$$

$$c_{66} = \mu_{xy} \,, \tag{3.16}$$

with

$$\gamma = \frac{1}{1 - \nu_{xy}\nu_{yx} - \nu_{yz}\nu_{zy} - \nu_{zx}\nu_{xz} - 2\nu_{yx}\nu_{zy}\nu_{xz}} \,. \tag{3.17}$$

With these components the Barnett and Lothe tensors $\boldsymbol{S}$ and $\boldsymbol{L}$ [65] can be expressed as

$$S_{21} = \sqrt{\frac{c_{66}\left(\sqrt{c_{11}c_{22}} - c_{12}\right)}{c_{22}\left(c_{12} + 2c_{66} + \sqrt{c_{11}c_{22}}\right)}} \,, \quad S_{12} = -\sqrt{\frac{c_{22}}{c_{11}}} S_{21} \,, \tag{3.18}$$

$$L_{11} = \left(c_{12} + \sqrt{c_{11}c_{22}}\right) S_{21}, \quad L_{22} = \sqrt{\frac{c_{22}}{c_{11}}} L_{11} \,. \tag{3.19}$$

All other elements of the 3×3 matrices $\underset{\approx}{\boldsymbol{S}}$ and $\underset{\approx}{\boldsymbol{L}}$ are zero. Qian and Sun [46] derived an explicit form of the components of the $\underset{\approx}{\boldsymbol{D}}$ and $\underset{\approx}{\boldsymbol{W}}$ matrices which can be used to describe the stress and displacement field in the vicinity of the crack tip.

$$\begin{aligned}
D_{11} &= \sum_{k=1}^{2} \frac{L_{11}^{(k)} \sin^2 \xi^{(k)} + L_{22}^{(k)} \cos^2 \xi^{(k)}}{L_{11}^{(k)} L_{22}^{(k)}} \\
D_{22} &= \sum_{k=1}^{2} \frac{L_{11}^{(k)} \cos^2 \xi^{(k)} + L_{22}^{(k)} \sin^2 \xi^{(k)}}{L_{11}^{(k)} L_{22}^{(k)}} \\
D_{12} &= \sum_{k=1}^{2} \frac{\sin \xi^{(k)} \cos \xi^{(k)} (L_{11}^{(k)} - L_{22}^{(k)})}{L_{11}^{(k)} L_{22}^{(k)}} \\
W_{21} &= \frac{S_{12}^{(2)}}{L_{22}^{(2)}} - \frac{S_{12}^{(1)}}{L_{22}^{(1)}}
\end{aligned} \tag{3.20}$$

Here ξ_i denotes the rotation angle of the material coordinates with respect to the global coordinate system and superscript (k) gives the corresponding materials, respectively. With Eq. (3.20) the near-tip relative crack face displacements in the x–y plane are

$$\Delta u_x(r) = \sqrt{\frac{2r}{\pi}} \left[(A\Im(\eta) \operatorname{Sgn}(W_{21}) + D_{12}\Re(\eta)) K_{\mathrm{I}} + D_{11}\Re(\eta) K_{\mathrm{II}} \right] \,, \tag{3.21}$$

$$\Delta u_y(r) = \sqrt{\frac{2r}{\pi}} \left[D_{22}\Re(\eta) K_{\mathrm{I}} + (-A\Im(\eta) \operatorname{Sgn}(W_{21}) + D_{12}\Re(\eta)) K_{\mathrm{I}} \right] \,. \tag{3.22}$$

The complex constant η is defined as

$$\eta = \frac{(r/l)^{\mathrm{i}\varepsilon}}{(1+2\mathrm{i}\varepsilon)\cosh\pi\varepsilon} \,. \tag{3.23}$$

Furthermore, A is

$$A = \sqrt{D_{11}D_{22} - D_{12}^2} \,, \tag{3.24}$$

and the oscillation index ε and the Dundurs parameter β is defined as

$$\varepsilon = \frac{\ln\frac{1+\beta}{1-\beta}}{2\pi} \,, \tag{3.25}$$

$$\beta = \frac{W_{21}\,\mathrm{Sgn}(W_{21})}{A} \,. \tag{3.26}$$

After transformation of Eq. (3.21) and Eq. (3.22) the stress intensity factors can be expressed as

$$K_{\mathrm{I}}(r) = \frac{\Delta u_x}{\sqrt{\frac{2r}{\pi}}\left(A_2 + A_3 - \frac{A_4 A_1}{A_3 - A_2}\right)} - \frac{A_4 \Delta u_y}{\sqrt{\frac{2r}{\pi}}\left(A_3^2 - A_3^2 - A_4 A_1\right)} \,, \tag{3.27}$$

$$K_{\mathrm{II}}(r) = \frac{\Delta u_y}{\sqrt{\frac{2r}{\pi}}\left(A_3 - A_2\right)} - \frac{A_1}{A_3 - A_2} K_{\mathrm{I}} \,, \tag{3.28}$$

with

$$A_1 = D_{22}\Re(\eta) \,, \tag{3.29}$$

$$A_2 = A\Im(\eta)\,\mathrm{Sgn}(W_{21}) \,, \tag{3.30}$$

$$A_3 = D_{12}\Re(\eta) \,, \tag{3.31}$$

$$A_4 = D_{11}\Re(\eta) \,. \tag{3.32}$$

Since the isotropic material behavior is a special case of the orthotropic behavior both methods produce the same results if applied to a pair of isotropic materials.

3.1.3 Accuracy issues

Basically the stress intensity factors could be derived without extrapolation directly from Eqs. (3.3) and (3.4) or Eqs. (3.27) and (3.28). But it was stated that stress intensity factors are not reliable when obtained directly from the crack surface displacements without

extrapolation [38] and may vary considerably depending on the distance to the crack tip [60]. These problems can be seen in Fig. 3.8 in Sec. 3.3.2.

Another accuracy issue appears when quadratic elements are used. The first midside node—the nearest node to the crack tip—produces inaccurate results with non singular elements (see Fig. 3.8, gray triangle), therefore this node pulls the extrapolation result away from the exact solution and it has to be dropped in order to get reliable results. This error is a result of the incapability of the elements to describe the singular behavior. With singular elements this effect was also found, but with less severe effect (see Fig. 3.8, gray bullet). On that account the first midside node is always dropped in the determination of fracture parameters.

Moreover, due to the application of a trigonometric function only the modulus of mode mix is computed. Since the fracture criteria is insensitive to the sign of the mode mix this drawback is neglectable. If the sign of the mode mix is requested the individual stress intensity factors have to be checked.

Finally, it is important to mention that theoretically the displacement extrapolation method cannot be applied for a crack under thermal loading. But in the vicinity of the crack tip the thermal displacement can be neglected. So it is important to stay in an area very close to the crack tip. A similar statement holds for problems with body forces.

3.2 Virtual crack closure technique

As indicated in Sec. 2.3.2 the basic idea of the virtual crack closure technique is based on Irwin's crack closure integral. For a crack loaded in pure mode I, Irwin computed the work necessary to close the crack from $a + \Delta a$ to a as

$$\Delta W_{\mathrm{I}} = \frac{1}{2} \int_0^{\Delta a} \Delta u_y(r) \sigma_y(\Delta a - r)\, dr \;, \tag{3.33}$$

where $\Delta u_y(r)$ is the crack face displacement in y direction at a distance r. The stress $\sigma_y(r)$ can be derived from LEFM as

$$\sigma_y(r)_{\theta=0} = \frac{B_1}{\sqrt{r}} + B_2 + B_3\sqrt{r} + (O) \;, \tag{3.34}$$

where B_i are constants, and (O) are terms of higher order which are neglected in the following.

The work ΔW_{I} is assumed to be the same as the work released from a to $a + \Delta a$. Thus, Irwin obtained the strain energy release rate $\mathscr{G}$ as

$$\mathscr{G}_{\mathrm{I}} = \lim_{\Delta a \to 0} \frac{\Delta W_{\mathrm{I}}}{\Delta a} = \lim_{\Delta a \to 0} \frac{1}{2\Delta a} \int_0^{\Delta a} \Delta u_y(r) \sigma_y(\Delta a - r)\, dr \ . \tag{3.35}$$

Similar equations exist for mode II and mixed mode situation.

Due to the discretization within the FEM the integral in Eq. (3.35) is replaced by a sum. Furthermore, it is a common technique to set the crack closure length Δa equal to the mesh size. Thus, the virtual crack closure integral is replaced by a sum of nodal forces combined with nodal displacements of the elements next to the crack tip.

As apparent in Eq. (3.35) two simulation runs are necessary to obtain the displacement $u_y(r)_a$ for crack length a and the stress $\sigma_y(r)_{a+\Delta a}$ for crack length $a + \Delta a$. With the assumption of self similar crack growing, i.e no crack kinking takes place, and a small increment in crack length compared to the total crack length, the stress state at the crack tip won't alter significantly during this crack growth. Thus, it is possible to derive the displacement $u_y(r)_a \simeq u_y(r + \Delta a)_{a+\Delta a}$ and the stress $\sigma_y(r)_{a+\Delta a} \simeq \sigma_y(r)_a$ in one run. This procedure is known as the virtual crack closure technique whereas the former one is called two-step crack closure technique.

Rybicki and Kanninen [53] used Eq. (3.35) to derive the VCCT method within FEM for 4-noded quadrilateral elements. Raju [47] extended the work of Rybicki and Kanninen to higher order and singular elements. A detailed discussion about the VCCT gives Krueger [32].

3.2.1 Non-singular 8-noded elements

Based on the Eq. (3.34), Raju [47] derived the three constants B_1, B_2 and B_3 out of the nodal forces F_i^n for $n = \{j, j+1, j+2\}$. Together with the parabolic shape functions of an isoparametric element the strain energy release rates are obtained as

$$\mathscr{G}_{\mathrm{I}} = -\frac{1}{2\Delta a} \left(F_y^j \Delta u_y^{j-2} + F_y^{j+1} \Delta u_y^{j-1} \right) \ , \tag{3.36}$$

$$\mathscr{G}_{\mathrm{II}} = -\frac{1}{2\Delta a} \left(F_x^j \Delta u_x^{j-2} + F_x^{j+1} \Delta u_x^{j-1} \right) \ . \tag{3.37}$$

The nodal forces and displacements can be obtained easily from the FEM (see Fig. 3.3. Note, the figure shows the VCCT with singular elements.). Here the forces at node $j + 2$ are not used because the relative displacement at node j (the crack tip) is zero.

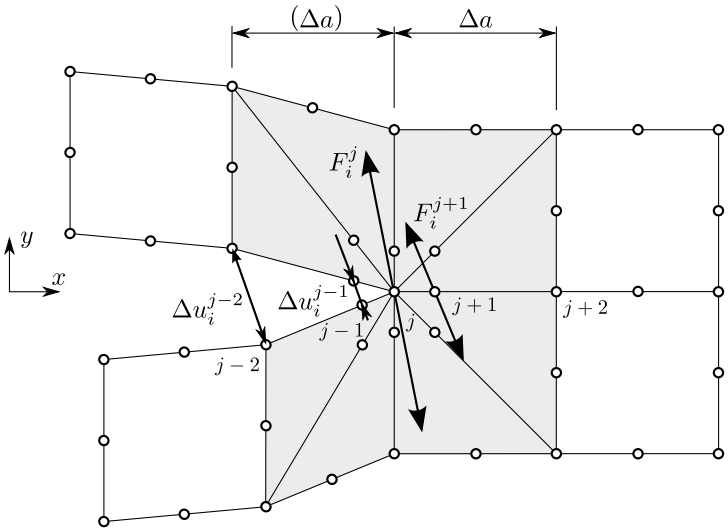

Figure 3.3: Simplified formulation of the virtual crack closure technique for singular elements.

3.2.2 Singular 8-noded elements

For singular elements Raju [47] derived a formulation consistent to the work of Rybicki and Kanninen [53]. This consistent formulation suffers a few drawbacks and thus a simplified formulation was subsequently developed. Both formulations are presented in the following but only the simplified one is implemented.

Consistent formulation – Similar to the non-singular elements the stress distribution ahead of the crack tip is given by Eq. (3.34). In conjunction with the shape functions the strain energy release rates can be expressed as

$$\begin{aligned}\mathscr{G}_{\mathrm{I}} = -\frac{1}{2\Delta a}[&F_y^j(t_{11}\Delta u_y^{j-2} + t_{12}\Delta u_y^{j-1}) \\ &+ F_y^{j+1}(t_{21}\Delta u_y^{j-2} + t_{22}\Delta u_y^{j-1}) \\ &+ F_y^{j+2}(t_{31}\Delta u_y^{j-2} + t_{32}\Delta u_y^{j-1})] \,.\end{aligned} \tag{3.38}$$

Here, t_{kl} $(k,l = \{1,2,3\})$ are constants, see e. g. [47]. A similar equation can be obtained for $\mathscr{G}_{\mathrm{II}}$ by replacing F_y with F_x and u_y with u_x. The forces at node $j+2$ have to be calculated with caution, see [42]. When dealing with a mode mix situation Eq. (3.38) has to be extended because the crack faces do not deform symmetrical or antisymmetrical with respect to the crack tip [47].

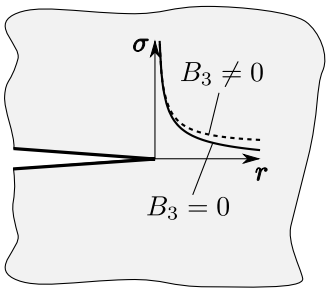

Figure 3.4: Stress distribution – consistent and simple formulation

Simple formulation – Compared to the equations of the non-singular elements the consistent formulation for singular elements is awkward even for pure mode I. This is due to the forces at node $j+2$. Thus, Raju [47] approximated this forces by setting the constant B_3 in Eq. (3.34) equal to zero. The change of the stress distribution is indicated in Fig. 3.4. For a small crack extension Δa the difference between the two curves is neglectable. With this approximation the strain energy release rate can be calculated as

$$\begin{aligned} \mathscr{G}_{\mathrm{I}} = &- \frac{1}{2\Delta a}[F_y^j(t_{11}\Delta u_y^{j-2} + t_{12}\Delta u_y^{j-1}) \\ &+ F_y^{j+1}(t_{21}\Delta u_y^{j-2} + t_{22}\Delta u_y^{j-1})] \ , \\ \mathscr{G}_{\mathrm{II}} = &- \frac{1}{2\Delta a}[F_x^j(t_{11}\Delta u_x^{j-2} + t_{12}\Delta u_x^{j-1}) \\ &+ F_x^{j+1}(t_{21}\Delta u_x^{j-2} + t_{22}\Delta u_x^{j-1})] \ , \end{aligned} \tag{3.39}$$

where

$$t_{11} = 6 - \frac{3\pi}{2}; \quad t_{12} = 6\pi - 20; \quad t_{21} = \frac{1}{2}; \quad t_{22} = 1 \ . \tag{3.40}$$

This equation is valid for mode I, mode II and mixed mode condition, and is considerably easier to use than Eq. (3.38).

Raju [47] recommends to use the simple formulation, since the resulting strain energy release rates are more accurate than their consistent counterpart. Nearly all of the available papers apply the simple formulation.

3.2.3 Interface cracks

When dealing with interface fracture mechanics the crack tip is generally loaded in a mixed mode condition. Furthermore, due to the oscillatory nature of the stress field the mode

I and mode II energy release rates start to oscillate when Δa approaches zero [63], see Fig. 2.11 in Sec. 2.2.3. However, the total energy release rate $\mathscr{G} = \mathscr{G}_1 + \mathscr{G}_2$ converges and can be computed by means of the VCCT. This implies that for interface cracks the mode mix (for a particular reference length) cannot be calculated by the VCCT out of the box.

To overcome this drawbacks several methods have been presented in the literature. Sun and Qian [60] used the VCCT in combination with the displacement ratio method to obtain the mode mix. Whereas Ikeda and Sun [25] applied a superposition procedure to the VCCT to calculate the mode mix with two simulation runs. Hwu and Hu [24] suggest to choose a finite value of $\Delta a/a > 0.05$ which results in nearly constant mixed mode ratios $\psi_G = \frac{\mathscr{G}_2}{\mathscr{G}_1}$. Agrawal and Karlsson [1] presents energy release rate based mode mixes and their relation to stress intensity factor based ones. Another approach is changing a less significant material properties so that Dundur's parameter β becomes zero [63]. It has been shown [63] that this method may yield inaccurate results.

In the current thesis a combination of DE method and VCCT is used. The mode mix is computed by means of the DE method and the norm of the stress intensity factor is derived by the VCCT.

3.2.4 Accuracy issues

The limes in Eq. (3.35) suggest that the elements surrounding the crack tip needs to be small. Furthermore, the elements in front of the crack tip should have the same size as the elements behind the tip, otherwise additional correction factors have to be applied [32].

The VCCT cannot be applied to thermal stress problems in the strict sense, but similar to the DE, the result should approach the exact values the smaller the distance to the crack tip becomes [25].

It is commonly accepted that energy based methods yield more accurate results than extrapolation methods. Thus, the VCCT method is used to calculate the energy release rate and to derive the corresponding norm of the complex stress intensity factor.

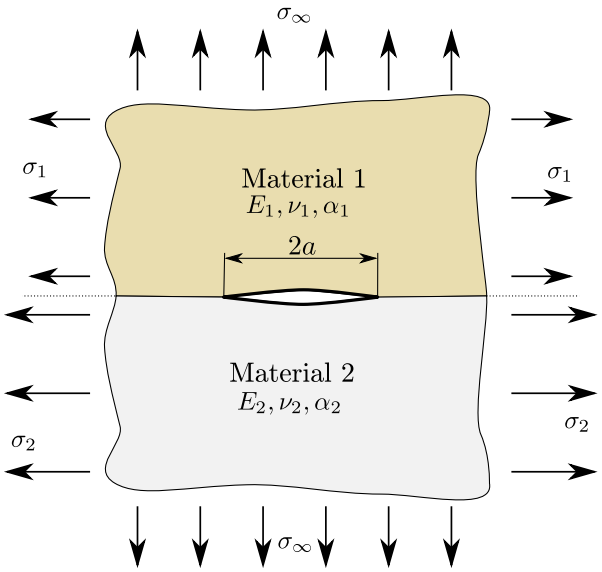

Figure 3.5: Verification problem: Interface crack subjected to tension.

3.3 Verification and comparison problems

Since the applied VCCT and DE methods had to be implemented a verification of the code was necessary. There exist a few analytically solutions for interface crack problems. The code was tested with, first, an interface crack subjected to tension, and, second, joined dissimilar semi-infinite plates with double edge cracks

The first example uses only mechanical loads whereas the second one is affected by thermal loads.

3.3.1 Interface crack subjected to tension

Two dissimilar semi-infinite planes share an interface (see. Fig. 3.5). This interface comprises a crack with length $2a$. The whole structure is loaded by far field tensile stresses. No shear stresses are applied. To ensure strain continuity along the bi-material interface a stress jump is considered according to [51], as

$$\sigma_2 = \Psi\sigma_1 + \frac{(3+\Psi)\mathrm{e}^{2\pi\varepsilon} - (3\Psi+1)}{1+\mathrm{e}^{2\pi\varepsilon}}\sigma_\infty \ , \tag{3.41}$$

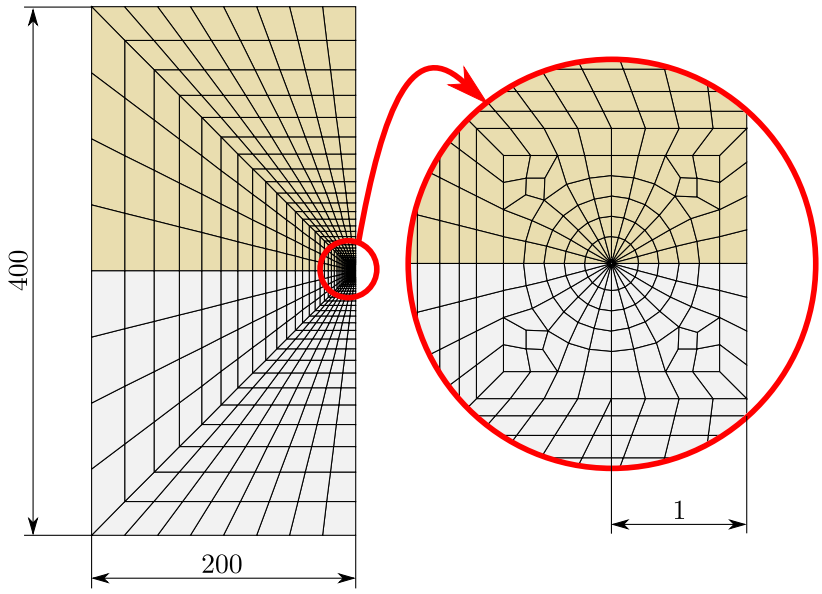

Figure 3.6: Mesh of the verification problem.

where

$$\Psi = \frac{\mu^{(2)}(\kappa^{(1)}+1)}{\mu^{(1)}(\kappa^{(2)}+1)},$$

and σ_∞ is the far field tensile stress perpendicular to the crack faces.

The geometry is build up using the ANSYS APDL language, where a is set to one unit. Regular 8-noded isoparametric elements with 2×2 integration scheme are used and for the elements surrounding the crack tip singular 8-noded elements are utilized, see Sec. 2.3.1. The materials used are linear elastic isotropic ones. Figure 3.6 shows the meshed geometry and gives the main dimensions. The material data is given in Tab. 3.1. With the shear modulus $\mu^{(k)} = \frac{E^{(k)}}{2(1+\nu^{(k)})}$ and $\kappa^{(k)} = 3-4\nu^{(k)}$, and $\eta^{(k)} = 1+\nu^{(k)}$, $k = \{1,2\}$ (for plane strain). A plane strain assumption is applied. The same model was used by various other papers, e. g. [27, 25].

The tensile loadings are $\sigma_\infty = 10$ and $\sigma_1 = 1$ unit of stress. With Eq. (3.41), σ_2 becomes -28.6 units. For simplicity the problem is considered in a dimensionless way.

An analytical solution for the given benchmark problem was proposed by Rice [51]. Rice introduce the stress intensity factors for the interface crack subjected to tension with a reference length $l = 2a$ as

$$K_1 + \mathrm{i}K_2 = \sigma_\infty(1+\mathrm{i}2\varepsilon)\sqrt{\pi a}\ . \tag{3.42}$$

Table 3.1: Material data used for the verification and comparison problems.

	Material 1	Material 2
Young's modulus E	10^{11}	10^{12}
Poisson ratio ν	0.3	0.3
Coefficient of thermal expansion α	10^{-7}	10^{-6}
Shear modulus	3.846×10^{10}	3.846×10^{11}
κ	1.8	1.8
η	1.3	1.3
ε	0.0758	

Table 3.2: Analytical and numerical values of K, for different element sizes, verification model 1

	Δa	K_1	K_2	K^{e}	Mode mix $\lvert\psi\rvert$
Analytic	-	17.724	2.687	17.927	0.150
DE	0.1	17.821	2.599	17.925	0.146
DE	0.05	17.690	2.599	17.915	0.146
VCCT	0.1	-	-	17.863	-
VCCT	0.05	-	-	17.875	-

The simulation results are presented in Tab. 3.2. Two cases with different element sizes around the crack tip are investigated. As stated before the VCCT is not capable of calculating the mode mix, thus only the norm of the complex stress intensity factor K^{e} is given. The error of K^{e} ($= \frac{K^{\mathrm{e}}}{K^{\mathrm{e}}_{analytic}}$) is for all tested configurations below 0.5% which is a very good value. Whereas the error of the mode mix ψ ($= \frac{\psi}{\psi_{analytic}}$) is about 2.7% which is acceptable.

3.3.2 Joined dissimilar semi-infinite plates with double edge cracks

The second verification example is two dissimilar semi-infinite plates with double edge cracks, resulting in just a small ligament (length $= 2b$) of the interface intact, see Fig. 3.7. The plates are loaded by a uniform change of temperature $\Delta\vartheta = 100$.

Again 8-noded isoparametric elements with a 2×2 integration scheme are used and for the elements surrounding the crack tip singular as well as non-singular 8-noded elements are used. The latter ones are for comparison reasons. By switching the boundary conditions

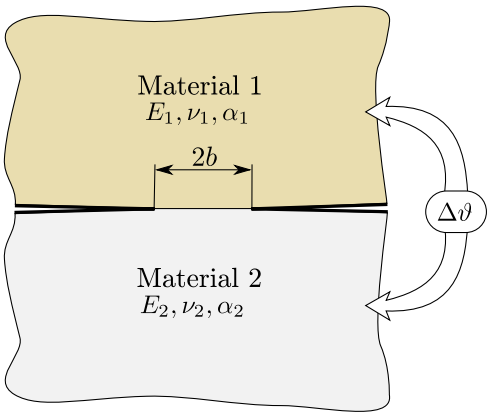

Figure 3.7: Verification problem: Joined dissimilar semi-infinite plates with double edge cracks.

the same mesh as created for the first example (Fig. 3.6) can be used. The materials used are the same as in the first verification problem, given in Tab. 3.1. Again a plane strain assumption is applied.

Erdogan [15] presented an analytical solution of the stress along the x-axis near the left crack tip as

$$\sigma_{yy} + \mathrm{i}\sigma_{xy} = \frac{\sigma_0(\alpha^{(2)}\eta^{(2)} - \alpha^{(1)}\eta^{(1)})\Delta\vartheta\sqrt{\pi b}}{\sqrt{2\pi x}}\,[2\varepsilon - \mathrm{i}]\left(\frac{x}{2b}\right)^{\mathrm{i}\varepsilon}\,, \tag{3.43}$$

where

$$\sigma_0 = \frac{4\mu^{(1)}\mu^{(2)}\cosh(\varepsilon\pi)}{\mu^{(1)} + \mu^{(2)}\kappa^{(1)} + \mu^{(1)}\kappa^{(2)} + \mu^{(2)}}\,. \tag{3.44}$$

From this equations the stress intensity factors with a reference length $l = 2b$ are

$$K_1 = \sigma_0(\alpha^{(2)}\eta^{(2)} - \alpha^{(1)}\eta^{(1)})\Delta\vartheta\sqrt{\pi b}2\varepsilon\,, \tag{3.45}$$

$$K_2 = -\sigma_0(\alpha^{(2)}\eta^{(2)} - \alpha^{(1)}\eta^{(1)})\Delta\vartheta\sqrt{\pi b}\,. \tag{3.46}$$

In Tab. 3.3 the simulation results are presented. The error of the stress intensity factor, K^{e}, and the mode mix, ψ, is for all runs with singular elements used below 0.3%. The non-singular elements show a suboptimal result with an error of about 3%. In Fig. 3.8 the extrapolation process is plotted for singular and non-singular elements with an element size of $\Delta a = 0.1$. As mentioned in Sec. 3.1 the first midside nodes are dropped due to a falsification of the result. It can be clearly seen that the computed values can be well fitted wit a linear extrapolation function.

Table 3.3: Analytical and numerical values of K, for different element sizes, verification model 2

	Δa	K_1 $[\times 10^6]$	K_2 $[\times 10^7]$	K^{e} $[\times 10^7]$	Mode mix $\lvert\psi\rvert$
Analytic	-	-1.615	1.065	1.078	1.721
DE singular	0.1	-1.652	1.064	1.081	1.723
DE singular	0.05	-1.645	1.065	1.080	1.723
VCCT singular	0.1	-	-	1.080	-
VCCT singular	0.05	-	-	1.079	-
DE non-singular	0.1	-1.364	1.034	1.044	1.702
VCCT non-singular	0.1	-	-	1.084	-

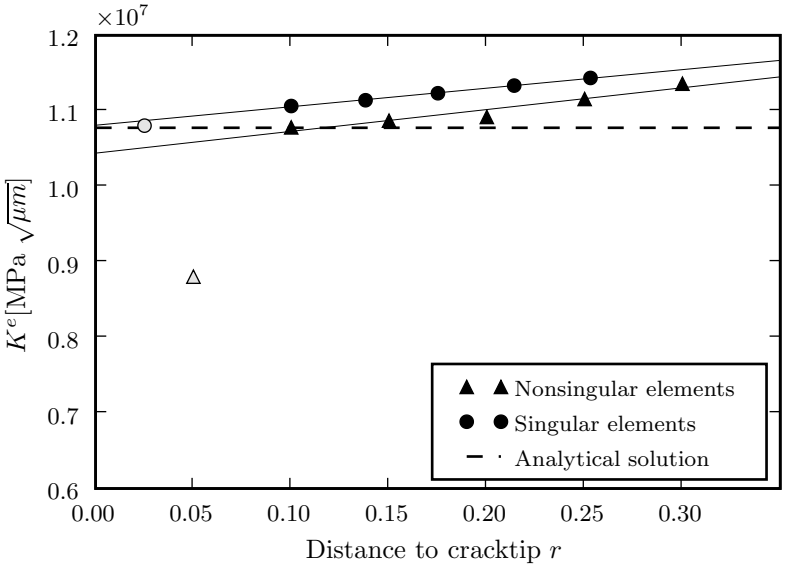

Figure 3.8: Stress intensity factor with displacement extrapolation method for non-singular and singular elements compared to the analytic solution for an element size of $\Delta a = 0.1$. The dropped first midside nodes are indicated in gray.

Chapter 4

Semiconductor modeling

As indicated in the introduction the multi-material structure of semiconductor devices is susceptible to interface debonding due to the mismatch of thermo-mechanical properties of the individual components. Devices fail by loosing the electrical or thermal conductivity due to interface delamination. Since relability concerns gain attraction the aim of this thesis is to examine the influences of certain geometry parameters on existing cracks.

The die-attach semiconductor device consists of various materials as sketched in Fig. 4.1. Due to a thermal loading, tractions at the interfaces arise and may lead to crack initiation and subsequent delamination.

The triangular shaped part of the die-attach in Fig. 4.1 represents the die-attach which is pushed out of the adhesive gap during the joining process. This surplus material is called bleed-out. Typical dimensions of the cross section are given in Tab. 4.1, for the associated components see Fig. 4.1.

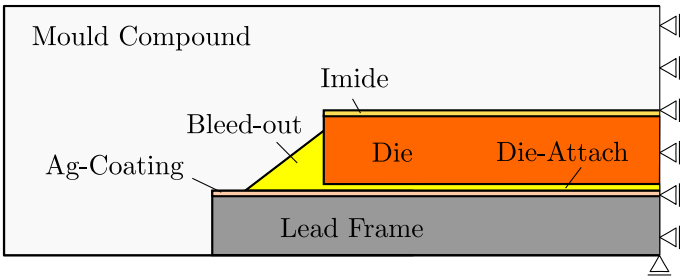

Figure 4.1: Sketch of the cross section of a glued die-attach device with boundary conditions.

Table 4.1: Typical dimensions of a semiconductor device cross section.

Component	Dimension [µm]
Die	2130×220
Lead frame	2650×200
Mould compound	4000×300
Imide-layer	thickness 8
Ag-coating	thickness 6.5
Die-attach	thickness 12
Bleed-out	various geometries

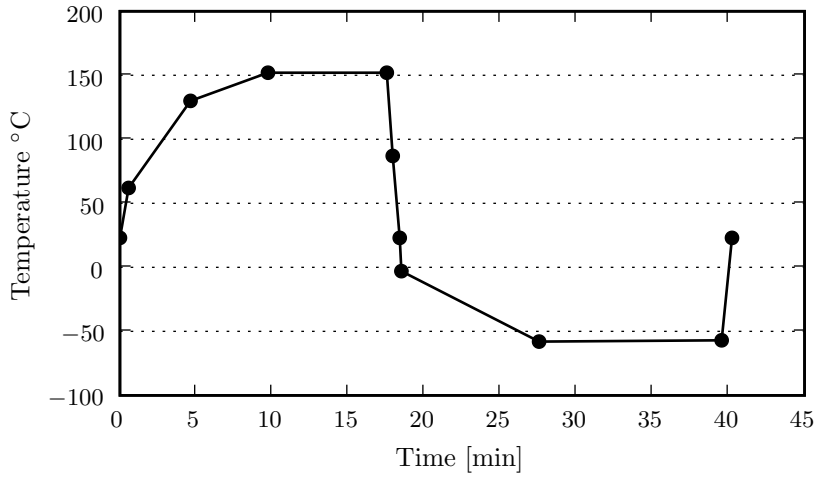

Figure 4.2: Typical temperature cycle for reliability testing.

The device is manufactured using various complex processes inducing considerably residual stresses. Thus, they should not be neglected in the simulation. After the production the device is subjected to several hundred thermal cycles (see Fig. 4.2) to assess the reliability of the device.

All interfaces are affected by thermal loads. For specific interfaces K-AI estimated the affinities to interface delamination relative to each other based on various device experiments. These interfaces are (see Fig 4.3)

(A) Imide – Mould compound

(B) Die – Mould compound

(C) Die-attach – Mould compound

(D) Ag-coating – Mould compound

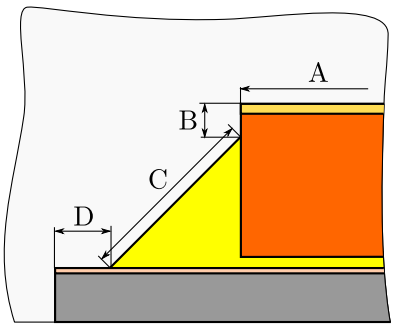

Figure 4.3: Interfaces with classified fracture affinity defined by K-AI.

The weakest interface is known to be the one shared by the mould compound and the die-attach (C). The other interface toughnesses are related as

$$\mathrm{C} \ll \mathrm{B} < \mathrm{D} < \mathrm{A} \,.$$

The missing not explicitly mentioned interfaces are not classified so far.

4.1 Level of abstraction

Using the ANSYS APDL language a fully parametrized plane model of the devices' cross-section is build up. Due to the symmetry in geometry and loading only half of the device is modeled (see Fig. 4.1). Thus, it has to be mentioned that intrinsically two cracks, one on each side, are simulated. This does not alter the result since the effect of the cracks on the stress and displacement fields is localized for the applied crack and geometry configurations. generalized plane strain assumption (GPS) for the main study, and plane strain assumption for the preliminary study, respectively, is applied. The GPS assumption allows for a linear distribution of out-of-plane normal strains ε_{zz}, however, the out-of-plane shear stresses, ε_{xz} and ε_{yz}, are zero. This way, out-of-plane bending is permitted. Since the implemented fracture mechanics methods are based on plane strain conditions the GPS may lead to some inconsistency in the calculation of the fracture mechanics parameters. But the gain in accuracy of the stress and strain field due to GPS is expected to exceed this shortcoming. Furthermore, the plane strain assumption applied within the determination of the fracture parameters is conservative in terms of fracture mechanics, hence, leading to an overall conservative result.

The device is loaded by a uniform temperature change $\vartheta_{\text{uniform}}$ based on room temperature. Hence, any whatsoever temperature gradient is prohibited. This leads to considerably easier implementation of fracture mechanics methods and removes a potential source of time dependency.

4.1.1 Material issues

The materials by which the device is composed need special attention. The basic set of material properties was supplied by K-AI as

Die – orthotropic, linear elastic material with temperature dependent coefficient of thermal expansion.

Lead frame – isotropic, elasto-plastic material with kinematic hardening.

Die-attach – isotropic, linear elastic material with temperature dependent Young's modulus, Poisson ratio and coefficient of thermal expansion.

Mould compound – isotropic, visco-elastic material with temperature dependent coefficient of thermal expansion.

Ag-plating – isotropic, elasto-plastic material with temperature dependent kinematic hardening and coefficient of thermal expansion.

Imide – isotropic, elasto-plastic material with temperature dependent multilinear isotropic hardening and Young's modulus.

A complete list of the employed material data cannot be given due to a confidentiality obligation. All materials were supplied with a reference temperature (a temperature free of thermal strains) as presented in Tab. 4.2. The FEM code ANSYS uses this temperatures to compute the secant coefficient of thermal expansion out of the instantaneous coefficient of thermal expansion or thermal strains given in the material definitions. For simplification purpose the imide and Ag-coating is not considered, see later. Since the present thesis involves linear elastic fracture mechanics the whole system is assumed to behave linear elastic (see Sec.2.1). Therefore, the plastic behavior of the materials is not considered. A plot of the tractions along the interface after the manufacturing process reveals that this is feasible in a conservative way (see later).

Table 4.2: Temperatures of zero thermal strain for the materials used.

Die	293 K
Lead-frame	473 K
Die-attach	473 K
Mould compound	468 K
Ag-coating	473 K
Imide	653 K

The visco-elastic material behavior of the mould compound cannot be neglected since the manufacturing process includes elevated temperatures. This leads to relaxation effects that generate significantly different result as simple linear elastic materials under the same conditions. As mentioned before linear elastic fracture mechanics is based on linear elastic material data. To overcome this problem the simulation is build up in two parts. At first the manufacturing process is simulated including visco-elastic material behavior and afterwards a linear thermo-elastic simulation with subsequent fracture mechanics analysis with appropriate linear elastic material data is carried out. To establish appropriate linear elastic material data for the mould compound the visco-elastic data is transformed using the Prony series representation of the relaxation moduli in conjunction with the Williams-Landau-Ferry shift function and the basic relations of elastic material properties (see below).

For the preliminary study a simplified version of the linear elastic material data is applied with the instantaneous material properties $E = E_0$ and $\nu = \nu_0$, and temperature dependent coefficients of thermal expansion.

Calculation of linear elastic data out of the Prony parameters

A general representation of visco-elastic material behavior is a parallel array of multiple maxwell elements (generalized maxwell model) and a single spring, see Fig.4.4. This generalized maxwell model with a spring in parallel denotes the Prony series [7].

The core equation of the shear relaxation modulus with Prony parameters (see [58]) reads

$$G(t) = G_0 \cdot \left(\alpha_\infty^G + \sum_{i=1}^{N} \alpha_i^G \cdot \mathrm{e}^{-t/\tau_i^G} \right) , \tag{4.1}$$

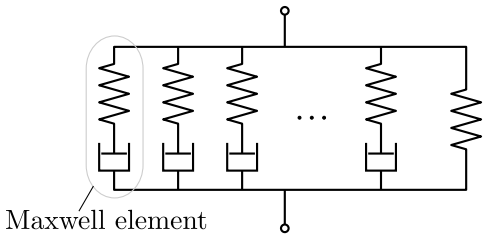

Figure 4.4: Rheological model of a visco-elastic material behavior in form of an generalized maxwell model with a spring in parallel.

with G_0 is the instantaneous shear relaxation modulus defined as

$$G_0 = \frac{E_0}{2(1+\nu_0)} \,, \tag{4.2}$$

where E_0 and ν_0 are the instantaneous Young's modulus and Poisson ratio, respectively. Moreover, G_∞ is the long-time shear relaxation modulus written as

$$G_\infty = G_0 \cdot \left(1 - \sum_{i=1}^{N} \alpha_i^G\right) \,, \tag{4.3}$$

and α_∞ is the normalized long-time shear relaxation modulus which reads

$$\alpha_\infty^G = \frac{G_\infty}{G_0} \,. \tag{4.4}$$

Here τ_i^G is the time constant for the shear relaxation modulus and $\alpha_i^G = \frac{G_i}{G_0}$ is the normalized shear relaxation modulus. Both properties together are called a Prony pair and N denotes the number of Prony pairs. The Prony coefficients are experimentally determined at a certain temperature. This temperature (T_{Prony}) is obviously different from the temperatures of zero thermal strains mentioned before. Figure 4.5 shows a typical variation of the shear relaxation modulus $G(t)$ over the time t.

A similar equation can be given for the bulk relaxation modulus with Prony parameters

$$K(t) = K_0 \cdot \left(\alpha_\infty^K + \sum_{i=1}^{N} \alpha_i^K \cdot \mathrm{e}^{-t/\tau_i^K}\right) \,, \tag{4.5}$$

with K_0 is the instantaneous bulk relaxation modulus defined as

$$K_0 = \frac{E_0}{3(1-2\nu_0)} \,, \tag{4.6}$$

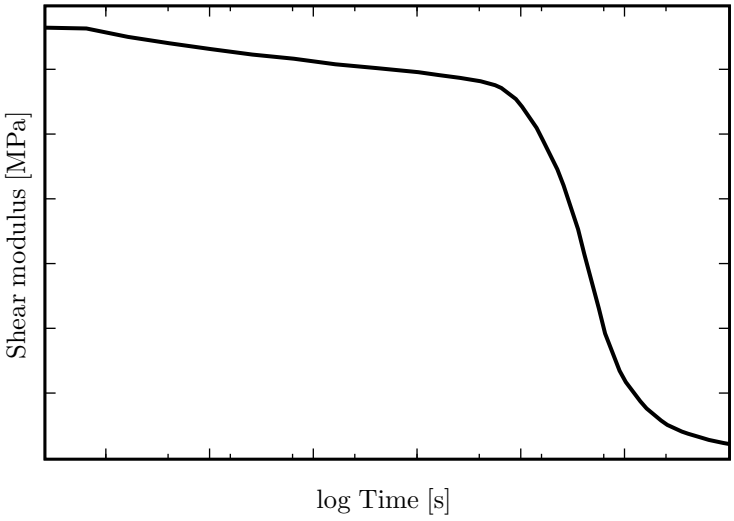

Figure 4.5: Shear relaxation modulus of the mould compound over time.

K_∞ is the long-time bulk relaxation modulus written as

$$K_\infty = K_0 \cdot \left(1 - \sum_{i=1}^{N} \alpha_i^K\right) , \tag{4.7}$$

and α_∞ is the normalized long-time bulk relaxation modulus given as

$$\alpha_\infty^K = \frac{K_\infty}{K_0} . \tag{4.8}$$

Here τ_i^K is the time constant for the bulk relaxation modulus and $\alpha_i^K = \frac{K_i}{K_0}$ is the normalized bulk relaxation modulus. The variation of the bulk relaxation modulus $K(t)$ over the time resembles the variation of the shear relaxation modulus (see Fig. 4.5).

The given time dependent material parameters $G(t)$ and $K(t)$ exhibit no temperature dependence so far. Since the mechanisms causing the relaxation effects are the same for long times and high temperatures, it is possible to shift the material parameters to include the temperature dependence [58]. The mould compound material supplied by K-AI uses the Williams-Landau-Ferry (WLF) shift function [68] written as

$$\log_{10} A(T) = \frac{C_1 \cdot (T - T_{\text{Prony}})}{C_2 + T - T_{\text{Prony}}} \tag{4.9}$$

where K-AI defines the constants as $C_1 = 71.42857143$ and $C_2 = 330.9357143$.

The insertion of the shift function $A(T)$ (4.9) into the equations of the shear and bulk relaxation modulus, Eq. (4.1) and Eq. (4.5), respectively, leads to

$$G(t,T) = G_0 \cdot \left(\alpha_\infty^G + \sum_{i=1}^{N} \alpha_i^G \cdot \mathrm{e}^{-t \cdot A(T)/\tau_i^G} \right) , \tag{4.10}$$

and

$$K(t,T) = K_0 \cdot \left(\alpha_\infty^K + \sum_{i=1}^{N} \alpha_i^K \cdot \mathrm{e}^{-t \cdot A(T)/\tau_i^K} \right) . \tag{4.11}$$

For linear (visco) elastic materials the elastic constants are related as [7]

$$E = \frac{9KG}{3K+G} , \tag{4.12}$$

and

$$\nu = \frac{3K-2G}{6K+2G} . \tag{4.13}$$

The combination of Eq.(4.12) and Eq.(4.13) with Eq. (4.10) and Eq. (4.11) yields

$$E(t,T) = \frac{9K(t,T)G(t,T)}{3K(t,T)+G(t,T)} , \tag{4.14}$$

and

$$\nu(t,T) = \frac{3K(t,T)-2G(t,T)}{6K(t,T)+2G(t,T)} . \tag{4.15}$$

For fixed times t the graph of the Young's modulus over the temperature, Eq. (4.14), is given in Fig. 4.6. The plot shows the times $t = 1000, 100, 10, 1, 0.1\,\mathrm{s}$ (from left to right). Furthermore, Fig. 4.7 presents the variation of the Poisson ratio (Eq. (4.15)). Again $t = 1000$, 100, 10, 1, $0.1\,\mathrm{s}$ is chosen (from left to right).

Since the designated thermo-elastic material behavior for the thermo-elastic simulation and fracture mechanics analysis is time-independent a reasonable value of t has to be chosen. Thus, a linear elastic material without any time dependence is obtained. With this fixed time the values for the Young's modulus and Poisson ratio for a specific temperature range can be extracted from Eq. (4.14) and Eq. (4.15), respectively. Here, a time of $t = 1\,\mathrm{s}$ is chosen. The temperature range is set to 193 K to 492 K based on the temperature loading range during simulation.

One must be aware that the computed set of linear elastic material data is far from being a comprehensive replacement of the visco-elastic material, since there is no time

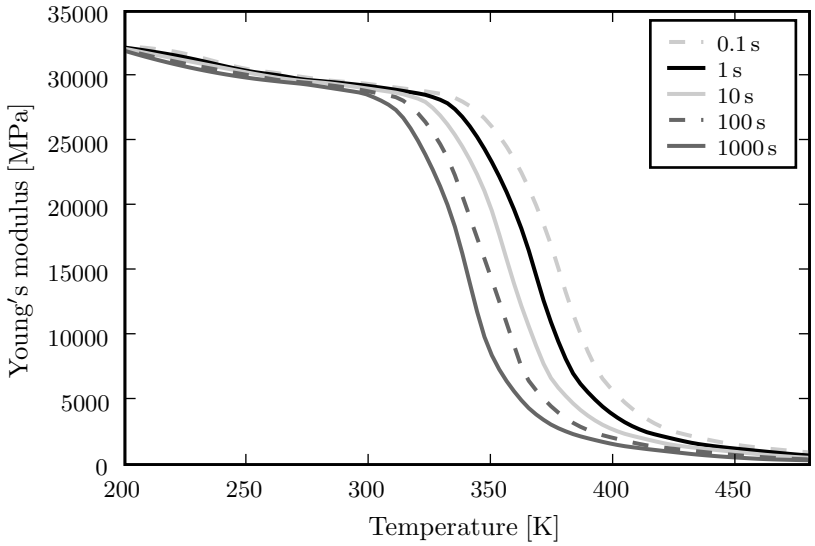

Figure 4.6: Young's modulus of the mould compound over temperature for different times t.

dependence modeled. Thus, depending on the simulated time range the accuracy of the simulation results may vary. Especially at temperatures around the transition range the derived material model may produces severe errors! Nevertheless, for the applications at low temperatures the obtained material model leads to good results compared with an visco-elastic comparative simulation.

It may be noted that during the computation of the Young's modulus and Poisson ratio numerical problems occurred. The values exceeded the margins of the usual number range, since the equations lead to terms like $e^{10^{38}}$. The computation was done with MATHEMATICA 7 (Wolfram Research Inc., Champaign, IL). How ANSYS deals with such large numbers is not known to the author.

4.2 Geometry and mesh

By means of the ANSYS APDL scripting language the geometry is build up. To enable a simple variation of the design all dimensions including the crack length and position are parameterized. The corresponding values are read from a parameter file. Special focus is put on the crack tip and crack surrounding area. Here the geometry is divided into equal rectangles (see Fig. 4.8) to achieve a consistent mesh with constant mesh quality all around the crack for all different design variations. If a crack tip is modeled near an

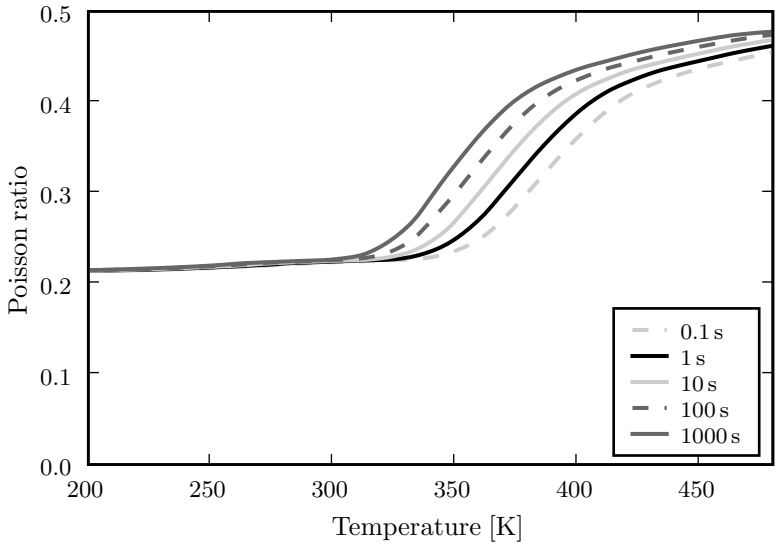

Figure 4.7: Poisson ratio of the mould compound over temperature for different times t

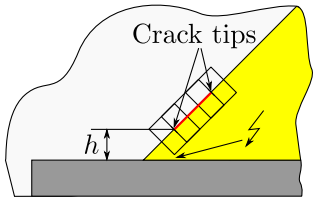

Figure 4.8: Underlying rectangles of a crack with critical location marked.

interface the perpendicular distance between the crack tip and the interface, h, is held approximately constant (see Fig. 4.8). Slight variations of h are necessary to retain the mesh quality. Here, the indicated point (↯) needs special attention. The mesh tends to be severely distorted due to the automeshing if the bottleneck gets to narrow.

The geometry is meshed with 8-noded isoparametric elements with a 2×2 integration scheme and a (generalized) plane strain assumption (PLANE183 in ANSYS notation). Crack tip elements are applied with a "radial" size of 2.5 µm. This element size is confirmed by means of a convergence study based on the stress intensity factor. The global element size is set to 8 µm. A sample mesh is given in Fig. 4.9.

For simplification the imide and the Ag-layer are not modeled. A plot of the tractions along the die-attach – mould compound interface after the manufacturing simulation indicates that this simplification in addition with the removal of the plasticity behavior results in a conservative approximation, see Fig. 4.10. Here the simulation with plasticity, imide

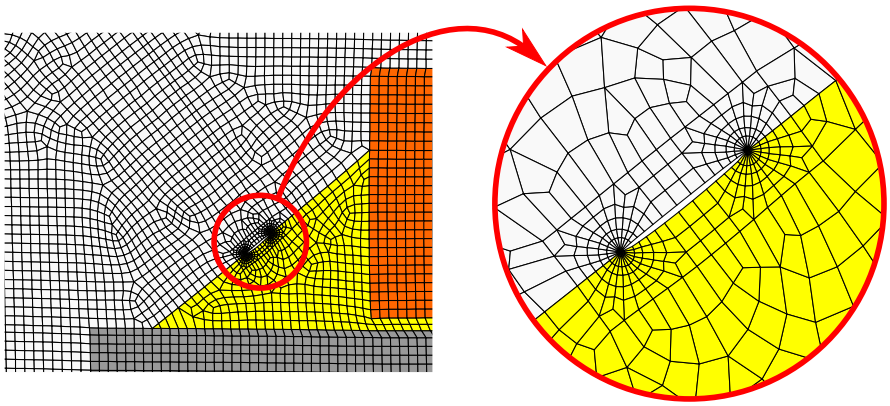

Figure 4.9: Example of a deformed mesh.

and Ag-layer enabled is denoted as “original” and whereas the simulation without these features is indicated as “simplified”. Moreover a typical geometry configuration without a crack is used.

As mentioned before only the half of the model is build due to the symmetry. Symmetric boundary conditions are applied on the nodes along the symmetry line. To prevent a rigid body movement the lower node on the symmetry line is fully constrained, see Fig. 4.1. Furthermore, the crack faces are tied together using multiple point constraints. This is necessary to simulate the manufacturing of a crack-free device. For the thermo-elastic simulation these multiple point constraints are removed.

4.2.1 Geometry variations and Crack configurations

Several variations of the geometry and crack configuration are prepared, see Fig. 4.11. Here, two different cracks are presented for all possible configurations. In this thesis a crack is always indicated as a highlighted line with two stop marks (⊢—⊣).

Basic configuration

The basic configuration denotes a simple triangular bleed-out shape with a crack located at the die-attach – mould compound interface, see Fig. 4.11a. This crack cannot be extended into a different interface by changing the underlying parameters.

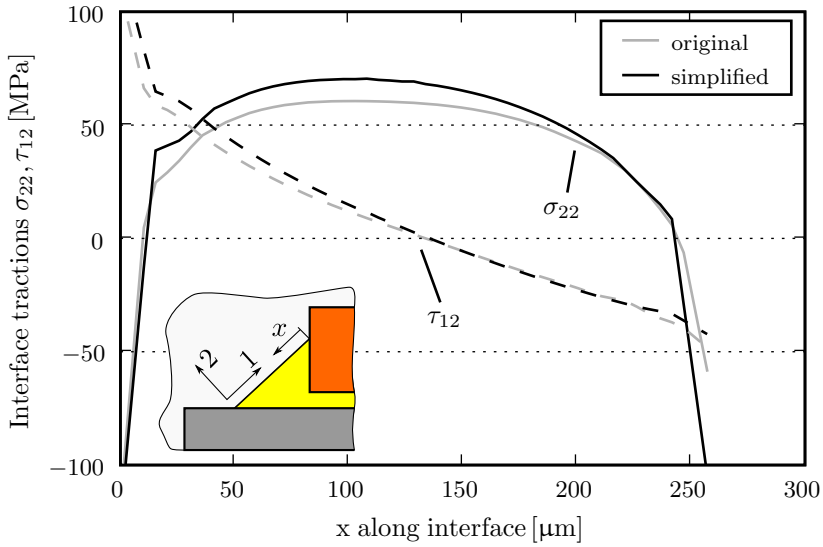

Figure 4.10: Interface tractions of the simplified and original device after the manufacturing process at 23°C without a crack.

Double edge configuration

The double edge configuration implies a variation of the bleed-out geometry. To get a more realistic bleed-out representation, the triangular shape of the basic configuration is changed into a concave but piecewise linear one (see Fig. 4.11b).

Crack configuration 1 and 2

In addition to these configurations with a small initial crack at the die-attach – mould compound interface, two more crack configurations with the basic bleed-out geometry are prepared. In crack configuration 1 the crack extends from the die-attach – mould compound interface into the lead frame – mould compound interface, see Fig. 4.11c. Here, two different crack lengths are presented.

In crack configuration 2 the crack is modeled starting at the lead frame – mould compound interface and reaching into the die – die-attach interface. Thus, the whole bleed-out is delaminated. Based on SEM images of cracked devices crack kinking out of the die-attach – mould compound interface is modeled at about three thirds of the bleed-out height (see Fig. 4.11d). Here, again two different crack length are presented. Furthermore, two special variations of crack configuration 2 are implemented. First, a delamination of the effective

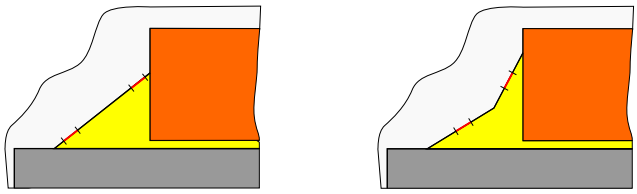

a) Basic configuration b) Double edge configuration

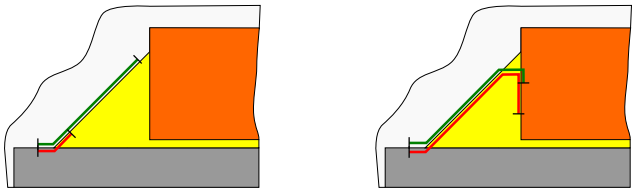

c) Crack configuration 1 d) Crack configuration 2

Figure 4.11: Different configurations of the main study with different crack positions indicated.

clearance, this means the crack extends over the whole horizontal lead frame – mould compound interface, and second, a delamination of the whole lead frame.

Certain variations of crack configuration 1 and 2 necessitate to consider contact between the crack faces. Therefore, contact elements (CONTA172 in ANSYS notation) and target elements (TARGE169 in ANSYS notation) are included at the crack faces in a symmetrical way e. g. both sides contain contact as well as target elements. This symmetric contact is typically used to reduce penetration. Thus, for these variations the FEM simulation becomes non-linear with an increment size of 0.125.

4.3 Manufacturing process

The simulation procedure and the corresponding input file of the non-linear manufacturing simulation was provided by K-AI.

The simulation procedure is basically divided into a die-attach step and a moulding step. During the die-attach step the die is heated up from room temperature to the die-attach (glue) deposition temperature (473 K). This is achieved by applying the corresponding temperature load. At this temperature the die-attach and the lead frame are added. The whole chip is then cooled down to room temperature.

In the moulding step the device is heated up to a point slightly below the mould compound deposition temperature (448 K) and the mould compound is added. A high temperature curing process is carried out by holding the temperature for four hours. Finally, the system is cooled down to room temperature and a low temperature curing process completes the manufacturing simulation. Thus, the device is kept for 24 hours at room temperature.

For the simulation of the manufacturing process the non-linear material data set, without any plasticity, is used. During the manufacturing a crack-free system is assumed. Thus, the crack faces prepared in Sec. 4.2 are kept tied together by the multiple point constraints.

After the last non-linear step the stress state is written to a file. This stress state is used as an initial stress field for the subsequent thermo-elastic analysis.

4.4 Thermo-elastic simulation

Since the crack is assumed to initiate during the thermal cycling after the manufacturing process this thermal cycling is considered next.

To get rid of any non-linearity a new simulation run is started. Due to the assumption of LEFM, linear material data is used (see Sec. 4.1.1). The mesh created in Sec. 4.2 is loaded and the crack is introduced by removing the multiple point constraints at the crack face nodes. To account for the manufacturing the residual stresses obtained out of the manufacturing simulation are applied. Finally, the thermal cycles are represented by a colling down of the system to the lowest temperature in the cycle (213 K). The high temperature part of the cycle is skipped due to the application of the LEFM and the underlying assumptions. Higher temperatures lead to distinct visco-elastic and, in reality, to visco-plastic effects, which clearly violates the assumptions of the linear elastic fracture mechanics. Moreover, the lowest temperature during the cycle is considered as the most severe case since toughness values increase with higher temperatures. Here, no cyclic crack extension can be considered, since the necessary material data is not available.

4.5 Fracture mechanics

After the linear solution step the implemented fracture mechanics methods (Sec. 3) are applied to both crack tips, where N (north) always denotes the upper (right) position and

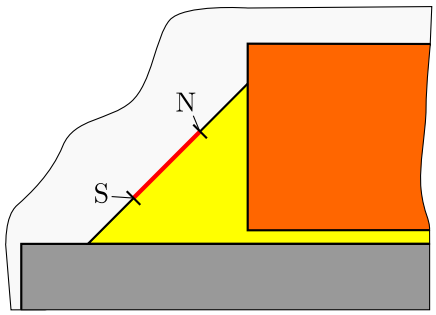

Figure 4.12: A crack with the crack tip identification letters.

S (south) is the lower (left) position, see Fig. 4.12. The results of the DE and VCCT are written into respective files and two summary files, one for each crack tip, are also created.

For the two additional variations of crack configuration 2 (delamination of the whole effective clearance or of the whole lead frame) the crack tip S cannot be evaluated due to a crack tip situation which is out of scope of the implemented fracture mechanics tools. A crack extending the whole effective clearance exhibits a complicated crack tip configuration at the corner of the lead frame. Whereas the entirely delaminated lead frame has no crack tip S at all.

4.6 Simulation procedure

4.6.1 Preliminary study

Here, only the basic configuration (triangular bleed-out with a small crack) is used. The manufacturing process is not included and only a linear simulation of the thermo-elastic problem is carried out. Linear elastic materials are used as described above.A further simplification is the assumption of a plane strain condition which implies $\varepsilon_{zi}(x, y) = 0$ for all x, y and $i = \{x, y, z\}$. Contact is not considered.

The mesh described in Sec. 4.2 is used with the variations presented in Sec. 4.7.1 The subsequent the linear simulations follow Sec. 4.4 and the fracture mechanics methods are applied according to Sec. 4.5.

4.6.2 Main study

As mentioned before the manufacturing process should not be neglected due to the resulting residual stresses. Thus, the main study accounts for this effect.

The simulation procedure is divided into 6 sub steps (see Fig. 4.13) and embedded in a batch controller to enable multiple runs with different parameters in an automated way.

First, the geometry is built up according to Sec. 4.2 with the variations given in Sec. 4.7.2. Due to some limitations with the application of residual stress fields within the FEM code ANSYS the mesh including all constraints is stored. The next sub step is the non-linear manufacturing simulation described in Sec. 4.3. Here, the resulting residual stress field is stored as mentioned before. The thermo-elastic simulation uses the previously stored mesh and the obtained residual stresses to compute the stress and displacement field at the coldest point of a thermal cycle. By means of these results the implemented fracture mechanics methods compute the stress intensity factors and the mode mix which are written into outfiles.
A detailed discussion of the applied configurations and variations is given in the following section.

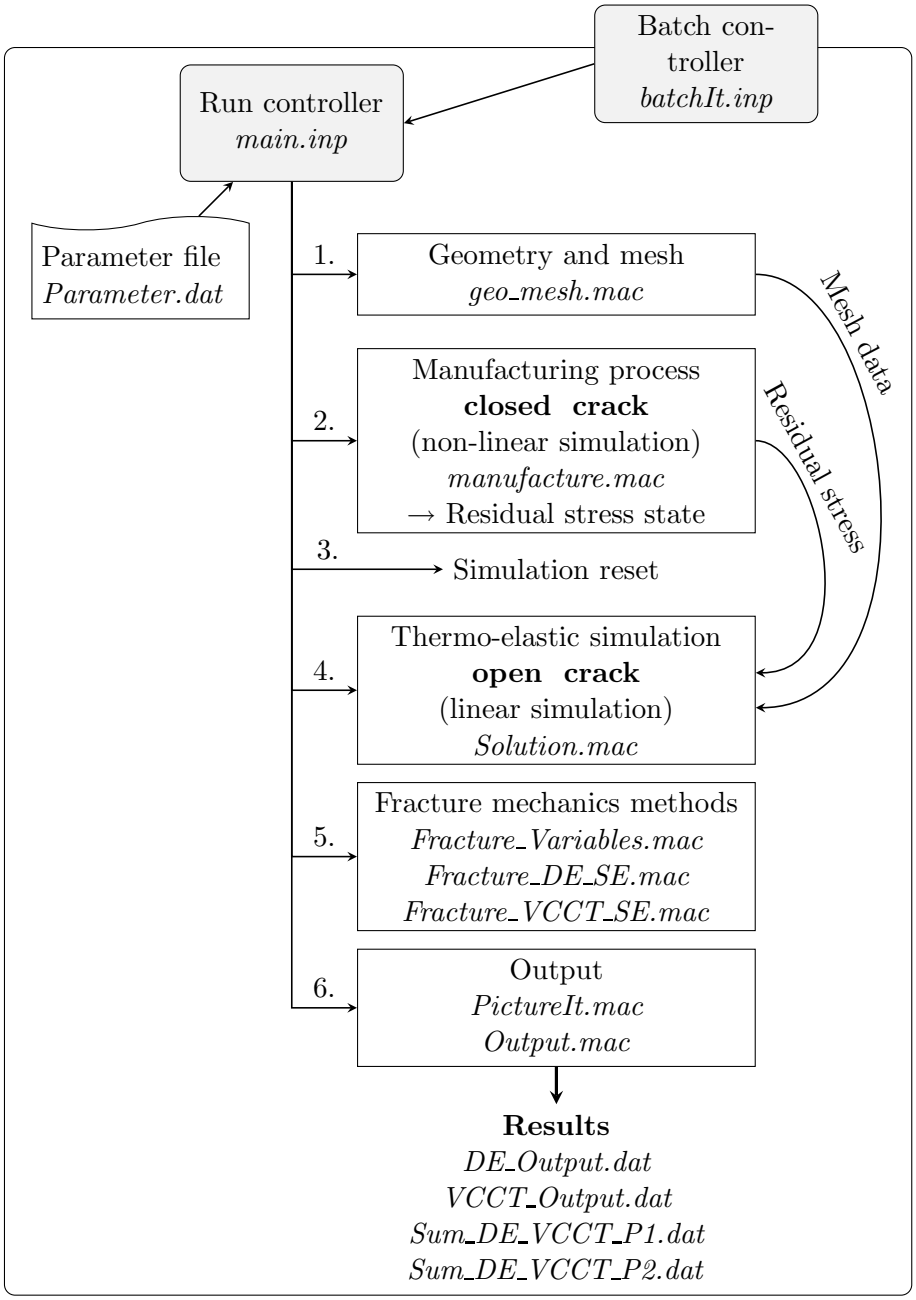

Figure 4.13: Flowchart of the simulation procedure including the appropriate file names and results for the main study.

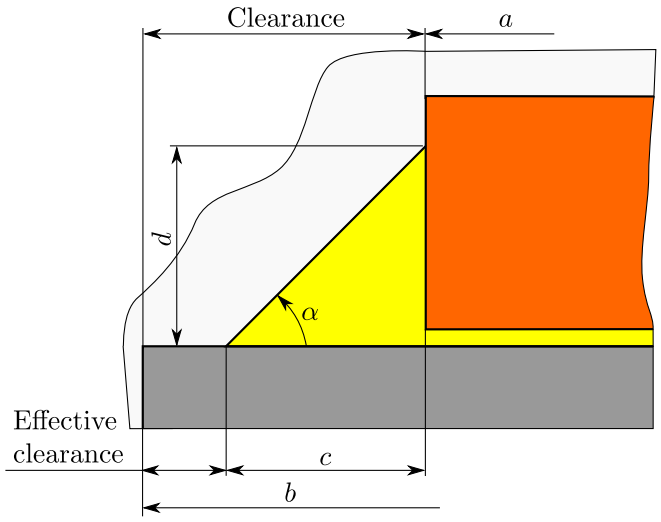

Die length	a
Lead frame length	b
Bleed-out length	c
Fillet height	d
Bleed-out angle	α
Clearance	
Effective clearance	

Figure 4.14: Geometry parameters for the design study.

4.7 Design study

To assess the influence of selected geometry parameters a design study is performed. Since the whole geometry including the crack is parametrized, the study can be performed in an automated way. Based on the real manufacturing process, special focus is set on the

- clearance,
- effective clearance, and
- bleed-out geometry.

Thus, the main geometry parameters are the corresponding dimensions die length, lead frame length, bleed-out length, and fillet height as presented in Fig. 4.14.

To avoid the problem with tri-material junction points all cracks are modeled in a certain distance from those. This is basically achieved due to the required space around the crack tip described in Sec. 4.2.

4.7.1 Preliminary study

As defined before the aim of the preliminary study is to assess the influence of the effective clearance on the fracture mechanics quantities like the stress intensity factors, and mode

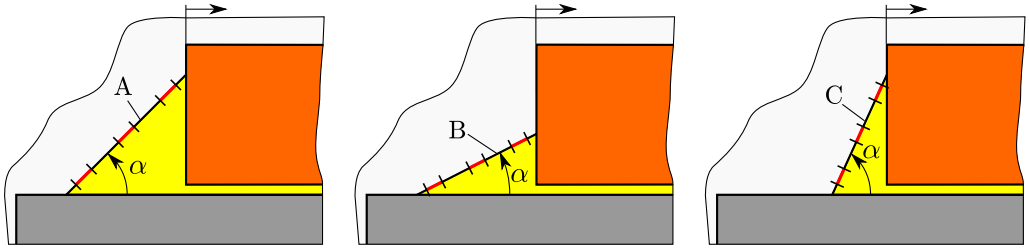

Figure 4.15: Bleed-out shapes and crack positions for the clearance variation of the preliminary study.

Table 4.3: Different bleed-out geometries for the clearance variation of the preliminary study.

Bleed-out	Bleed-out angle α	Bleed-out length c
A	40°	204 µm
B	20°	204 µm
C	60°	100 µm

mix. The effective clearance can be altered by changing the clearance, by assuming a different bleed-out length with constant clearance, or by a combination of both. The last option is not considered due to the obvious dependence of the results on more than one variable.

To assess the influence of the effective clearance caused by a change of the clearance four different die lengths are examined. These simulations are carried out with a constant lead frame length as defined in Tab. 4.1. To get more information three different bleed-out geometries (A, B, and C) and three different crack positions, see Fig. 4.15 are used together with these variations. The different bleed-out shapes are given in Tab. 4.3. The crack positions are always on the upper side, lower side, or one in the middle of the die-attach – mould compound interface. For all 36 runs an initial crack length of 20 µm is used. With this setup the variation of the clearance and the variations of the effective clearance are the same. Thus, the results are valid for both parameters.

The next part of the preliminary study is a variation of the effective clearance with a constant clearance. Thus, the bleed-out length has to be altered. Compared to the previous runs, here, the bleed-out length is used directly to alter the effective clearance. Whereas before, it was used to change the bleed-out geometry in three defined ways but the variation was obtained by a change of the clearance. As seen before a variation of the bleed-out length implies a change of the bleed-out angle. Thus, the influences of the effective clearance with constant clearance on the fracture mechanics parameters is

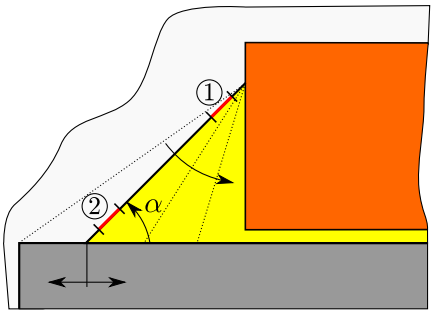

Figure 4.16: Variation of the bleed-out length and the resulting chance of the bleed-out angle α.

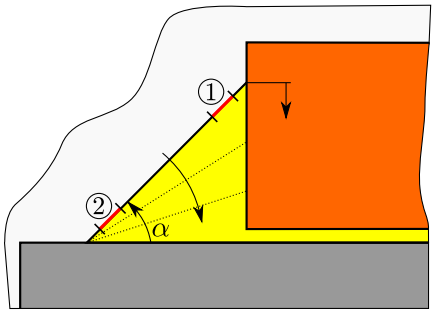

Figure 4.17: Variation of the fillet height and the resulting change of the bleed-out angle α.

ambiguous and cannot be separated from the bleed-out geometry. For the following runs a die-length of 2130 µm is used.

The variation of the bleed-out length is done in 8 steps with a constant fillet height resulting in a bleed-out angle of $37° - 69°$. Two different crack positions, one on the upper and one on the lower side of the die-attach – mould compound interface (Position ① and ②, see Fig. 4.16) are assumed. Due to the ambiguous character of the effective clearance, the bleed-out angle is used to describe the geometry situation. To increase the variation range of the bleed-out angle it has to be altered independently of the two clearances by changing the fillet height (see Fig. 4.17). In this case the effective clearance remains constant as long as the clearance is not changed. The variation of the fillet height is simulated in 8 steps representing a bleed-out angle in the range $16° - 37°$ with a constant effective clearance of 56 µm thus, a wide range of bleed-out angles is simulated. Again, two different crack positions are examined for each bleed-out angle. For all simulation runs an initial crack length of 20 µm is applied. Here, the main focus is moved to the bleed-out geometry and both variations can be plotted by a single graph for simplicity.

4.7.2 Main study

Based on the findings of the preliminary study the main study is extended to different geometry and crack configurations.

Four different crack and geometry configurations are used (see Fig. 4.11). The basic configuration is a simple triangular bleed-out with two possible crack positions. The double edge configuration represents the real bleed-out geometry in a more realistic way. In configuration 1 the crack is extended into the lead frame – mould compound interface. A

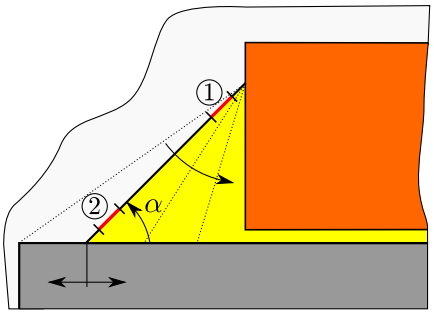

Figure 4.18: Variation of the effective clearance with constant fillet height.

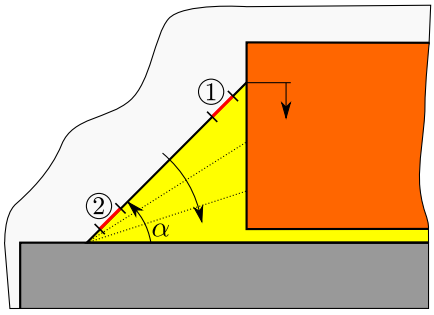

Figure 4.19: Variation of the bleed-out angle α with constant bleed-out length.

further crack extension is modeled in crack configuration 2, where the crack also reaches the die attach – die interface. Additionally, crack configuration 2 is used to examine the effect of the delamination length of the effective clearance on the fracture mechanics parameters of the crack tip N.
The variations of the different configurations are described in the following.

Basic configuration

Following the simulation scheme described in Sec. 4.6.2 the basic configuration is applied in a similar way as in the preliminary study. Thus, in comparison with the preliminary study the effect of the residual stresses and the generalized plane strain assumption can be obtained.

The effective clearance and the bleed-out geometry is varied in the following manner.

- Variation of the effective clearance with constant fillet height of 156.5 µm, (implies a variation of the bleed-out angle α), Fig. 4.18.
- Variation of the fillet height with constant bleed-out length of 200 µm, (implies a variation of the bleed-out angle α), Fig. 4.19.
- Variation of the bleed-out angle α with constant bleed-out area $A \approx 24000\,\mu m^2$, Fig. 4.20.

As indicated in Fig. 4.18 and Fig. 4.20 the effective clearance is varied starting with length zero for this two cases. Two different crack positions (one on the upper and one on the lower side, respectively) are simulated. Additionally, all of the simulation runs are carried

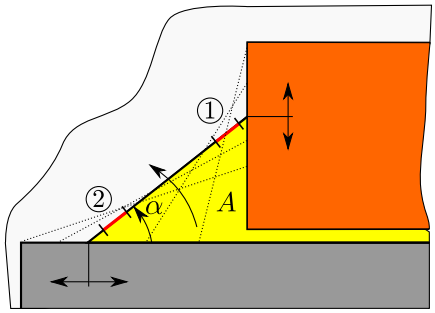

Figure 4.20: Variation of the bleed-out angle α with constant bleed-out area A.

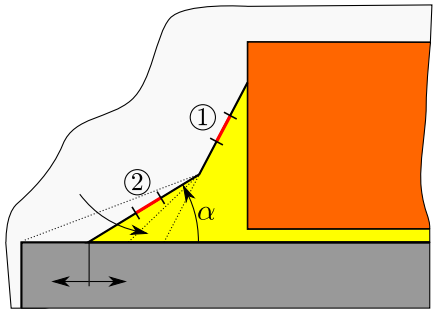

Figure 4.21: Variation of the effective clearance with constant fillet height and bleed-out center point.

out with a die length of 2130, 1950, and 1800 µm. Unlike in the preliminary study the results of the variation of the bleed-out length and the fillet height are not combined since the underlying mechanisms are different. Thus, three independent plots are obtained. All undefined dimensions are taken from Tab. 4.1.

Double edge configuration

To appraise the influence of different bleed-out angles in a more realistic way the double edge configuration is used. The main aim is to assess if a concave shaped bleed-out is acceptable and if a change of the lower bleed-out angle affects an interface crack at the upper side of the bleed-out. Here, the upper part of the bleed-out is modeled with a fixed angle and length and only the lower part is varied, see Fig. 4.21. Investigated crack positions are the centers of the respective bleed-out faces. The die length is 1800 µm, the upper bleed-out angle is modeled as 57°. The other dimensions are chosen according to Tab. 4.1.

Crack configuration 1

Crack configuration 1 represents an extended crack. Here, the crack extension length at the lead frame – mould compound interface is always modeled as 20 µm. All other, not explicitly varied, dimensions are given in Tab. 4.1. For this configuration two different variations are carried out. First, the influence of the clearance is assessed with a constant bleed-out geometry, Fig. 4.22. Here, the die length is varied in five steps according to typical die dimensions. In the second variation the bleed-out length is altered with a constant fillet height and die length (see Fig. 4.23). All runs for both variations are simulated twice. First, with a long crack extending nearly the whole die-attach – mould compound interface (①), and second, with a shorter crack just entering the bleed-out (②).

Crack configuration 2

Similar to the crack configuration 1 the bleed-out length is varied to assess its influence on the fracture mechanics parameters of a further extended crack, see Fig. 4.24. There are two different crack length simulated. For both the die-attach – mould compound interface is completely delaminated. The crack extension along the lead frame – mould compound interface is constant for all runs and equals 20 µm. Thus, only the crack extension along the die-attach – die interface is modeled in two different length. Again, all other dimensions are taken from Tab. 4.1.

Additional runs are added to assess if an intact effective clearance helps to prevent the crack from growing along the die-attach – die interface. Thus, the variation of the bleed-out length is carried out with two further extension of the crack at the lead frame – mould compound interface. This time the crack delaminates the whole effective clearance and

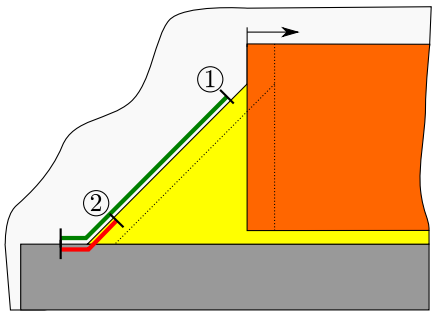

Figure 4.22: Variation of the clearance with constant bleed-out geometry.

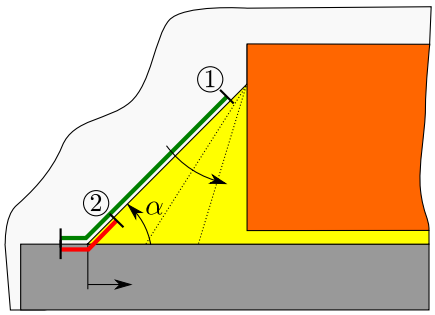

Figure 4.23: Variation of the bleed-out angle with crack configuration 1.

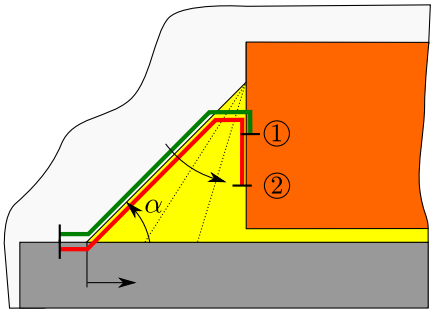

Figure 4.24: Variation of the bleed-out angle with crack configuration 2.

the whole lead frame, respectively (see Fig. 4.25 and Fig. 4.26). For these two cases the crack parameters can only be obtained at the N crack tip since the other crack tip changes its singularity or does not exist at all.

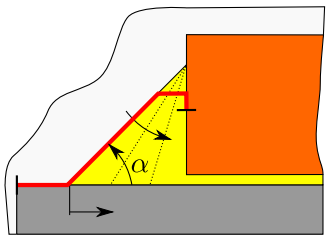

Figure 4.25: Extended crack configuration 2 over whole effective clearance.

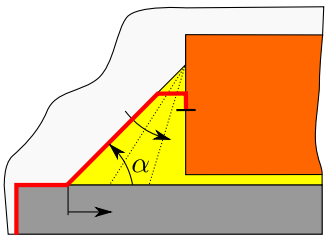

Figure 4.26: Extended crack configuration 2 over whole lead frame.

Chapter 5

Results and discussion

As mentioned before only a single temperature of the thermal cycle could be investigated due to the limitations of the LEFM. Since most of the available materials show a tougher behavior at higher temperatures this handicap is expected to give conservative predictions. Furthermore, a auxiliary simulation shows that for higher temperatures the resulting interface tractions are less severe in terms of fracture mechanics.

Another limitation is that due to a lack of interface toughness data only crack tip stress intensities can be given. Thus, a "crack initiates / crack does not initiate" statement cannot be given. Moreover, it cannot be ruled out that the crack may kink out of the interface instead of growing along the interface in mixed mode condition.

In this thesis all stress intensity factors and mode mixes are computed with a reference length of $l = 20\,\mu\text{m}$ (see Sec. 2.2.2). For all not explicitly denoted crack tip results the upper crack tip (N) is used. This is feasible since the difference of the stress intensity factors and the mode mix for the two crack tips (N, S) is acceptable small due to the short crack length. Furthermore, instead of the mode mix (ψ), the norm of the mode mix ($|\psi|$) is used in the following. Since typical interfaces exhibit a symmetrical fracture toughness (see Sec. 2.2.5) this does not affect the quality of the results.

5.1 Preliminary study

As introduced in Sec. 4.7.1 only linear thermo-elastic simulations are carried out and the die length, bleed-out length and/or fillet height are varied. Linear thermo-elastic materials

are used and a plane strain assumption is applied.
This study is split into two sub studies, first the clearance and afterwards the bleed-out is varied.

5.1.1 Variation of the clearance

As described in Sec. 4.7.1 the die length is varied in four steps. Additionally, three different bleed-out geometries (A, B, and C) and three different crack positions, see Fig. 4.15, are used. The results for the different crack positions are presented in the following subsections.

Lower crack position

Here a crack in a lower position at the die-attach – mould compound interface is assumed. Figure 5.1 shows the predicted stress intensity factors and mode mixes for three different bleed-out geometries with respect to a variation of the clearance. It can be seen that only for bleed-out A and B the increase of the clearance leads to a marked effect on the norm of the stress intensity factor K^{e}. However, Bleed-out C is nearly unaffected by this variation. These trends are a result of the singular stress field at the corner of the lead frame. Due to the limited size of this singularity only the cracks of bleed-out A and B can be affected. The crack of bleed-out C, which shows a higher effective clearance due to the lower bleed-out length is not in the spear of influence of this singularity.

Moreover, Fig. 5.1 shows that the mode mixes remain nearly constant. The higher mode mix of bleed-out C is explained by the strong influence of the die, i. e. the mismatch of the coefficient of thermal expansion and the orientation of the crack with respect to the die. Bleed-out A and B show a mode I dominated behavior, where the slightly increased mode mix of bleed-out B is explained by the influence of the lead frame. Since all mode mixes stay below 87° the results are valid, because no crack face contact will occur, see Sec. 2.2.2.

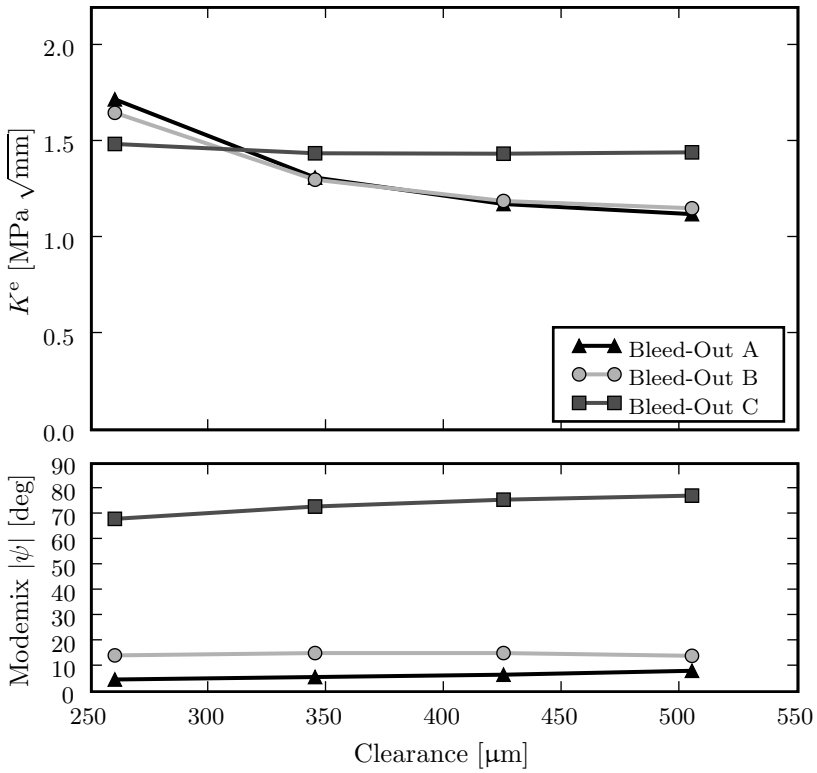

Figure 5.1: Predicted stress intensity factors and mode mixes for different bleed-out geometries with respect to a variation of the clearance for the lower crack position.

Middle crack position

A crack in a middle position of the interface shows a similar behavior than a crack at the lower position. Again, Fig. 5.2 presents the predicted stress intensity factors and mode mixes for three different bleed-out geometries with respect to a variation of the clearance. It can be seen that the overall stress intensity factor level is a bit increased compared to the lower crack position but the characteristics remains similar. The effect of the variation of the clearance on the stress intensity factors for bleed-out A and B is less pronounced compared to a crack in a lower position.

Furthermore, Fig. 5.2 shows that the mode mixes are independent of the clearance. Due to the high value of the mode mix of the crack in bleed-out C ($|\psi| > 100°$) a crack face penetration will occur and additional considerations are necessary. Thus, the corresponding stress intensity factor is theoretically not valid and should be treated with caution.

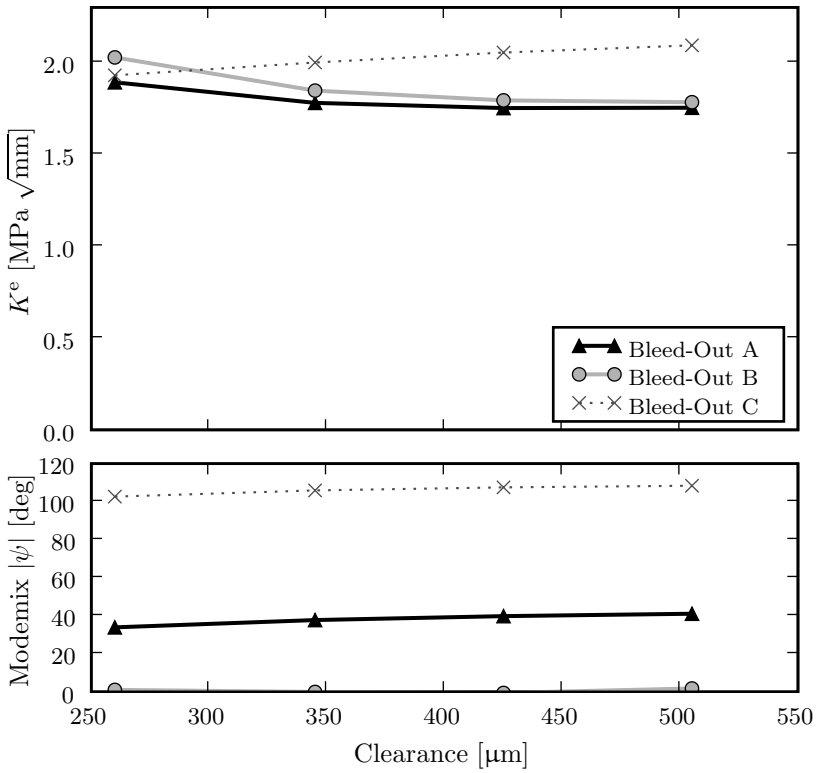

Figure 5.2: Predicted stress intensity factors and mode mixes for different bleed-out geometries with respect to a variation of the clearance for the middle crack position.

Upper crack position

Figure 5.2 presents the predicted stress intensity factors and mode mixes for three different bleed-out geometries with respect to a variation of the clearance for a crack in an upper position of the interface. The figure indicates that there is nearly no influence of the clearance variation on the stress intensity factors of the cracks at the upper position. The same applies for the mode mixes. Here, again, bleed-out C shows a mode mix which is beyond the limit introduced by the assumption of small scale contact (see Sec. 2.2.2), thus the corresponding values have to be treated with caution.

Comparing the three different crack positions, a global increase of the stress intensity factors with increasing crack position at the interface can be seen. This results from a combination of the increasing vertical position of the crack tips and the more distinct influence of the die due to the decreasing distance.

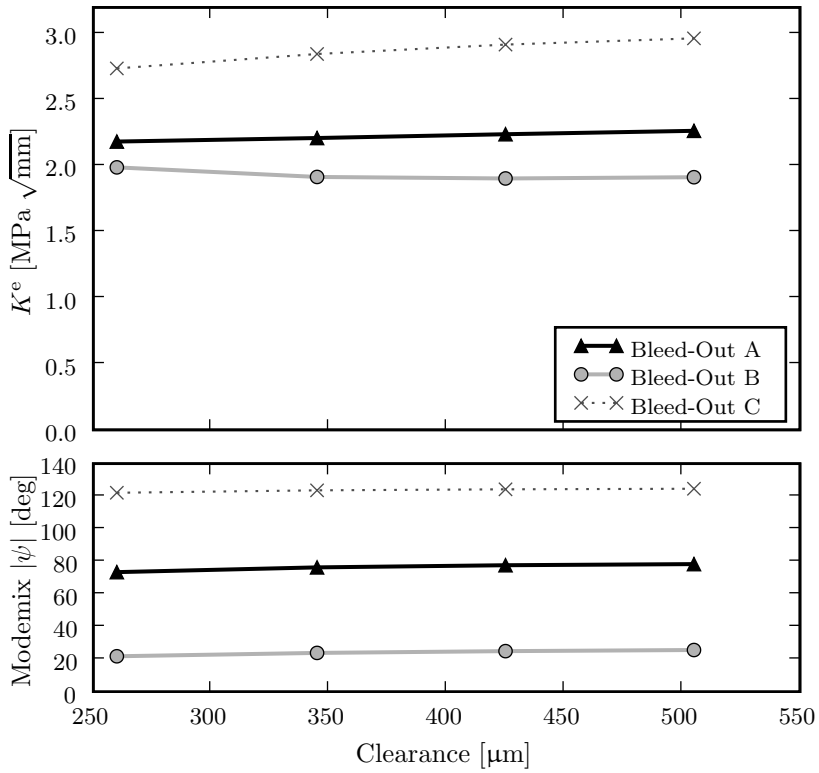

Figure 5.3: Predicted stress intensity factors and mode mixes for different bleed-out geometries with respect to a variation of the clearance for the upper crack position.

5.1.2 Variation of the bleed-out

As discussed in Sec. 4.7.1 the influence of the effective clearance with constant clearance is superseded by a variation of the bleed-out angle. Thus, a variation of the bleed-out angle (with constant fillet height or constant bleed-out length) is examined in this step. A constant die length of 2130 µm is used which implies a constant clearance. Here the main focus is laid upon the mode mix behavior. As described earlier the results for bleed-out angles smaller than 37° are obtained by altering the fillet height (Fig. 4.17) whereas the bigger angles are created by a change of the bleed-out length (Fig. 4.16). The results of these two methods are plotted in Fig. 5.4 (gray versus black symbols).

The first obvious result in Fig. 5.4 is the strong dependence of the mode mix on the bleed-out angle. It can be clearly seen that for the crack in position ② there exists a minimum at about $\alpha = 33°$. The increase of the mode mix towards a lower bleed-out angle results from the escalating influence of the lead frame and the orientation of the crack with respect to

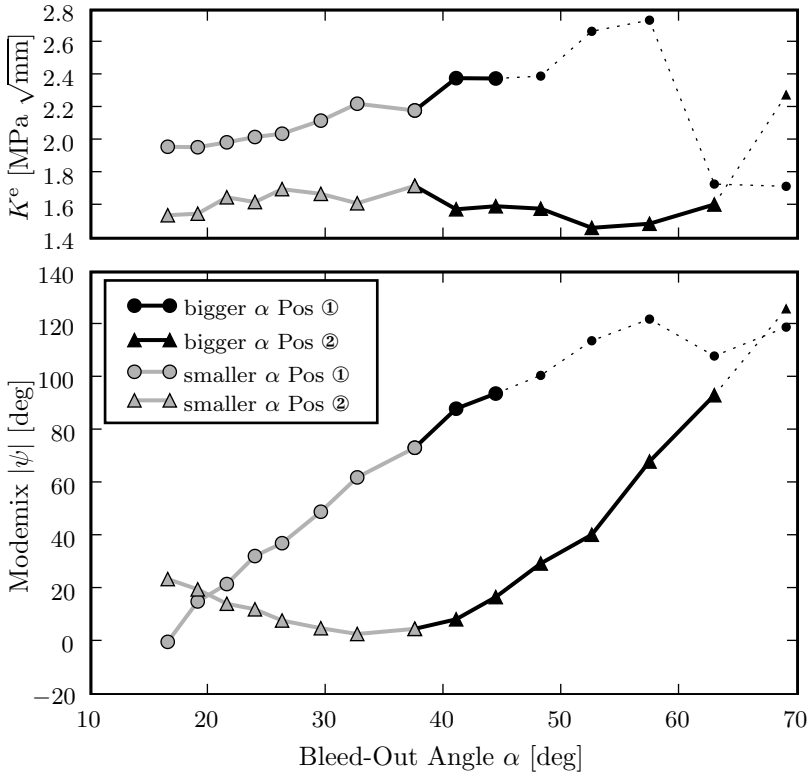

Figure 5.4: Predicted stress intensity factors and mode mixes with respect to a variation of the bleed-out angle for two different crack positions and two different variation methods.

the lead frame. For higher bleed-out angles the influence of the die increases the mode mix even further. A higher mode mix indicates an increased contribution of the shear stresses. The higher crack position ① generally leads to higher values of the mode mix because of influence of the die is more pronounced.

A second result is that similar to the mode mixes the stress intensity factors are higher for a increased vertical crack tip position. This has already been found at the clearance tests before.

Due to the limitations of linear elastic fracture mechanics the mode mixes greater than 87° and the corresponding stress intensity factors have to be treated with caution since they are theoretically invalid. Like before, additional considerations would be necessary.

5.2 Main study

Based on the results discussed above the main study is carried out as defined in Sec. 4.7.2. It contains the residual stresses derived from the manufacturing simulation and various crack and geometry configurations. Furthermore, a generalized plane strain assumption is used. Here, the basic and double edge geometry configurations as well as the crack configurations 1 and 2 are applied as defined in Sec. 4.7.2.

Since a change of the effective clearance with constant clearance implies a change of the bleed-out angle the following interpretations will focus on this bleed-out angle. The same applies for the variation of the fillet height.

5.2.1 Basic configuration

Here, similar characteristics for the stress intensity factors and mode mixes are expected compared to the preliminary study. However, the overall stress intensity factor level will be increased. Thus, the effect of the residual stresses based on the manufacturing process will be visible.

The basic configuration is modeled with three different die lengths as discussed in the following. For each die length the bleed-out geometry is varied and the three resulting plots are given. They present a variation of either the bleed-out length, the fillet height or both, see Sec. 4.7.2.

Basic configuration – 2130 µm die length

Here a basic triangular shaped bleed-out is modeled. The die length is 2130 µm resulting in a clearance of 260 µm.

Figure 5.5 shows the influence of a variation of the effective clearance or the bleed-out angle on the stress intensity factor and mode mix for two different crack positions. The increase of the bleed-out angle leads to a distinct change of the stress intensity factors and mode mixes. Here, for the upper and lower crack position the predicted stress intensity factors and mode mixes show opposite trends. For the higher crack position ① the stress intensity factor decreases with increasing bleed-out angle. At the same time, the mode mix increases. Thus, a crack at position ① shows a “good” behavior in terms of fracture

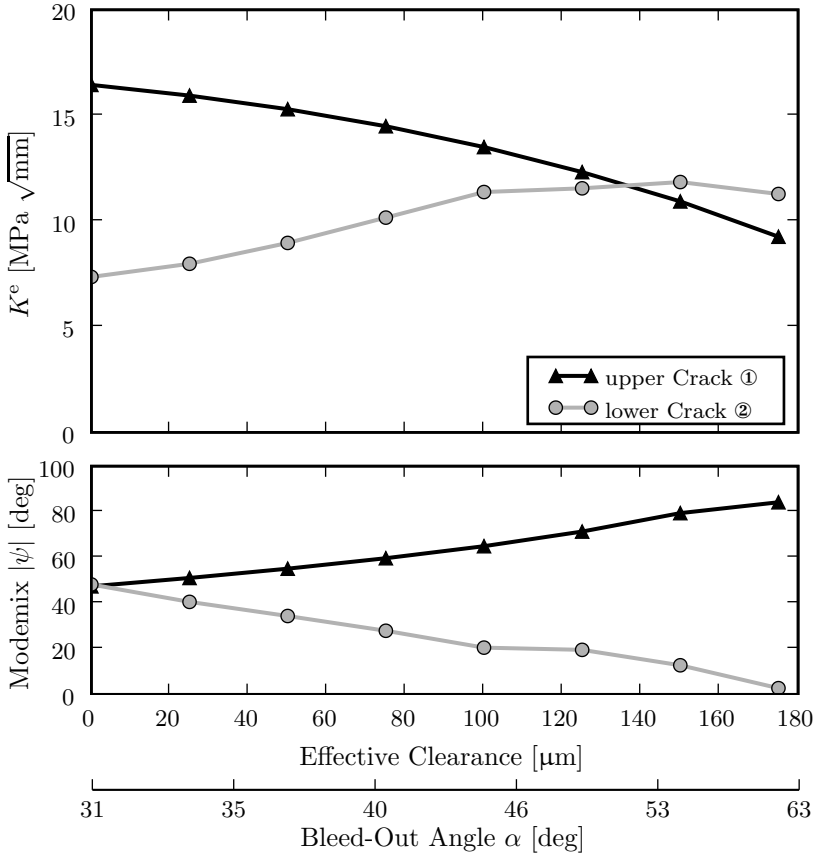

Figure 5.5: Predicted stress intensity factors and mode mixes with respect to a variation of the effective clearance with constant fillet height, and 2130 µm die length for two different crack positions.

mechanics, if the corresponding bleed-out angle has a high value. On the contrary, a small bleed-out angle results in high stress intensity factors and low mode mixes, hence, revealing a more critical situation. As mentioned before the lower crack (position ②) exhibits an inverse behavior. Thus, the stress intensity factor increases and the mode mix decreases with an increasing bleed-out angle.

A combined consideration of these results indicate that a concave shaped bleed-out will lead to good overall results (see Fig. 5.6). Compared to the preliminary study the stress intensity factors are increased by a factor of about seven and show a clean characteristics. The plots of the mode mixes are shifted towards higher bleed-out angles but show similar characteristics as expected from the preliminary runs.

The predicted stress intensity factors and mode mixes with respect to a variation of the fillet height with constant clearance is presented in Fig. 5.7, which, basically, shows a

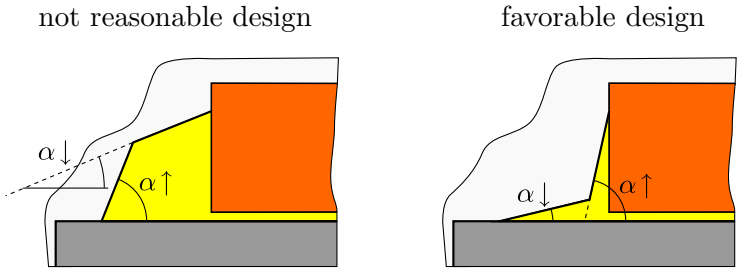

Figure 5.6: Sketch of a not reasonable and favorable design of the bleed-out geometry.

similar result than Fig. 5.5. Again, the stress intensity factors and mode mixes of the two crack positions are affected in an opposite way. One interesting point here is that the mode mix of the lower crack position does not change markedly with the variation of the fillet height. This implies that a change of the angle with a constant position has a lower impact on the mode mix of a crack in the vicinity of the lead frame than a change of the horizontal position (compare with Fig. 5.5). The upper crack position does not show this dominant position depended behavior.

Figure 5.8 shows the predicted stress intensity factors and mode mixes with respect to a variation of the bleed-out angle with constant bleed-out area for two different crack positions. The variation of the bleed-out angle implies a change of the bleed-out length and the fillet height. Thus, the interpretation of the result is difficult. Basically, Fig. 5.8 shows a similar behavior for the stress intensity factors and mode mixes during the variation as the former two results. Here, the mode mix exceeds the limit of 87° hence, results have to be treated with caution due the assumptions of LEFM.

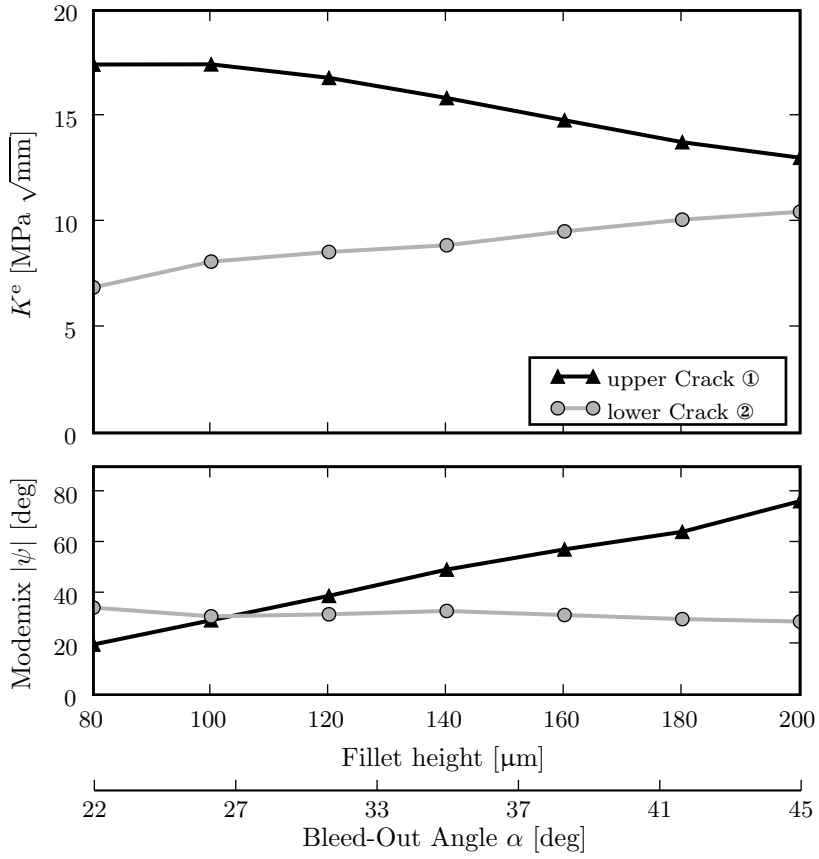

Figure 5.7: Predicted stress intensity factors and mode mixes with respect to a variation of the fillet height with constant bleed-out length, and 2130 µm die length for two different crack positions.

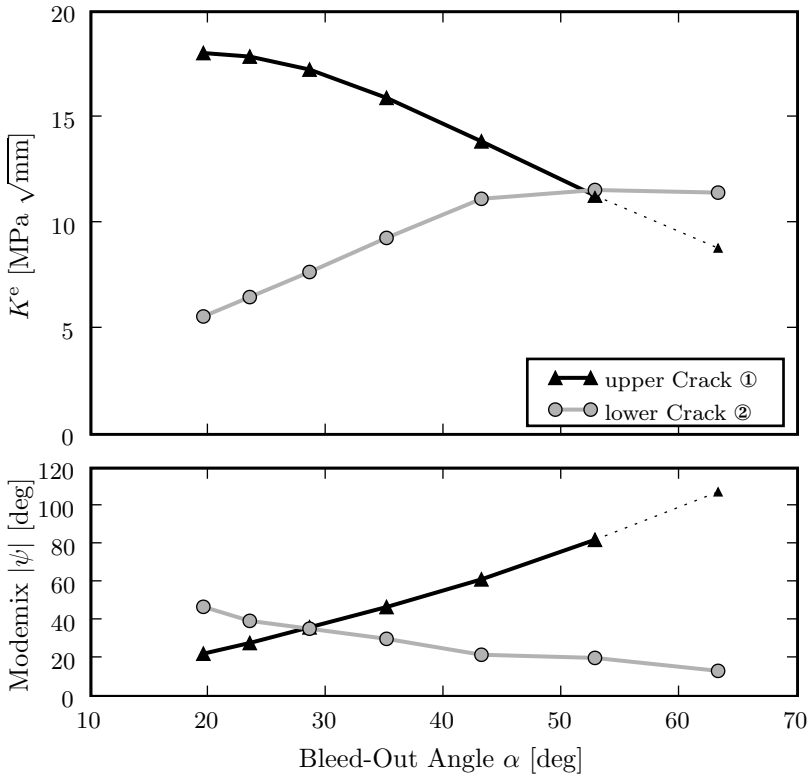

Figure 5.8: Predicted stress intensity factors and mode mixes with respect to a variation of the bleed-out angle with constant bleed-out area, and 2130 µm die length for two different crack postions.

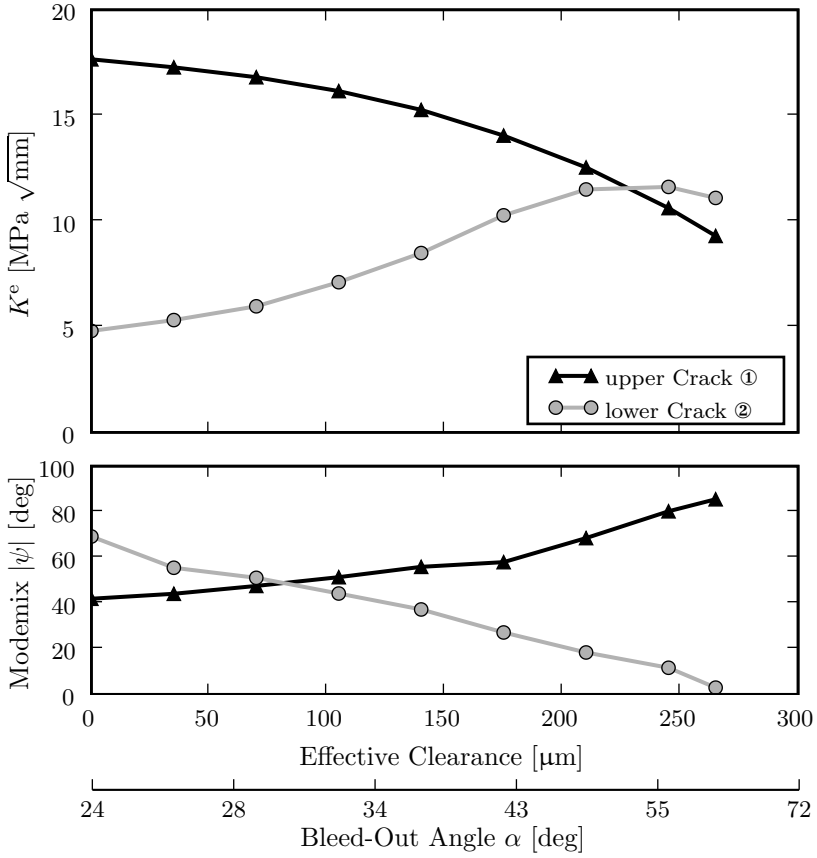

Figure 5.9: Predicted stress intensity factors and mode mixes with respect to a variation of the effective clearance with constant fillet height, and 1950 µm die length for two different crack positions.

Basic configuration – 1950 µm die length

Now the die length of 1950 µm is considered which results in a clearance of 350 µm. Figure 5.9 shows the predicted stress intensity factors and mode mixes with respect to a variation of the effective clearance. A comparison of Fig. 5.9 with Fig. 5.5 indicates that the die length has no effect on the fracture mechanics parameters. This can be particularly visualized if the plot is scaled to match with the plot of the former die length (Fig. 5.5) in terms of the bleed-out angle.

The characteristics of the stress intensity factors and mode mixes due to a variation of the fillet height (Fig. 5.10) and the bleed-out angle with constant bleed-out (Fig. 5.11), respectively, show basically the same behavior like before with a die length of 2130 µm.

An interesting point with Fig. 5.11 is that the stress intensity factor decreases for bleed-out

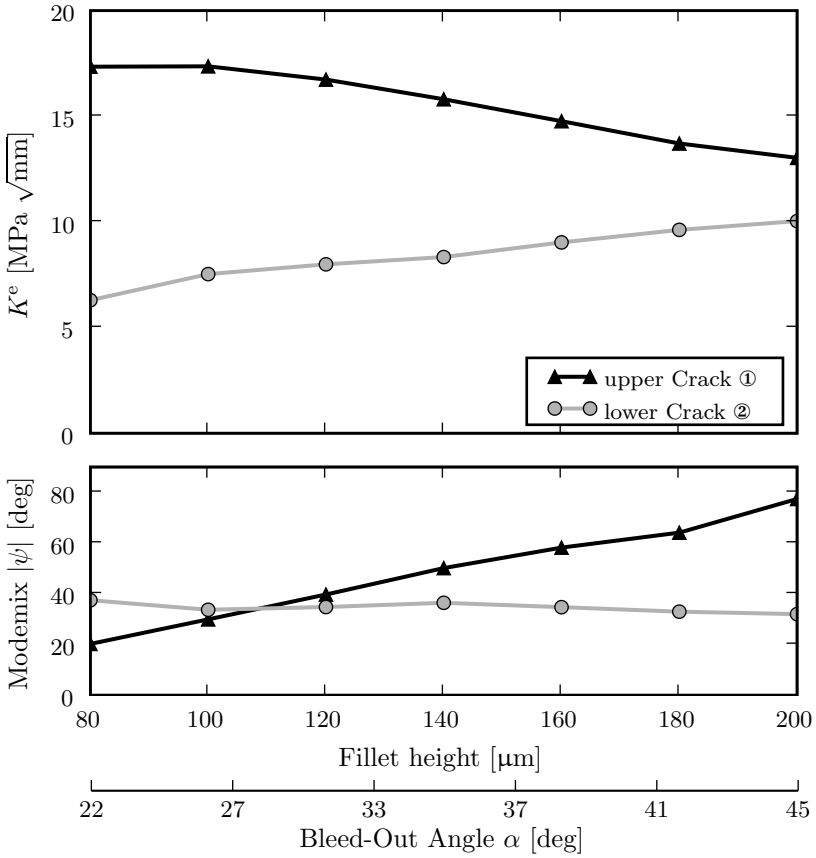

Figure 5.10: Predicted stress intensity factors and mode mixes with respect to a variation of the fillet height with constant bleed-out length, and 1950 µm die length for two different crack positions.

angle values below 15° for the upper crack position. This is a result of the singular point at the die corner and the resulting stress field distortion which interacts with the crack tip stress field.

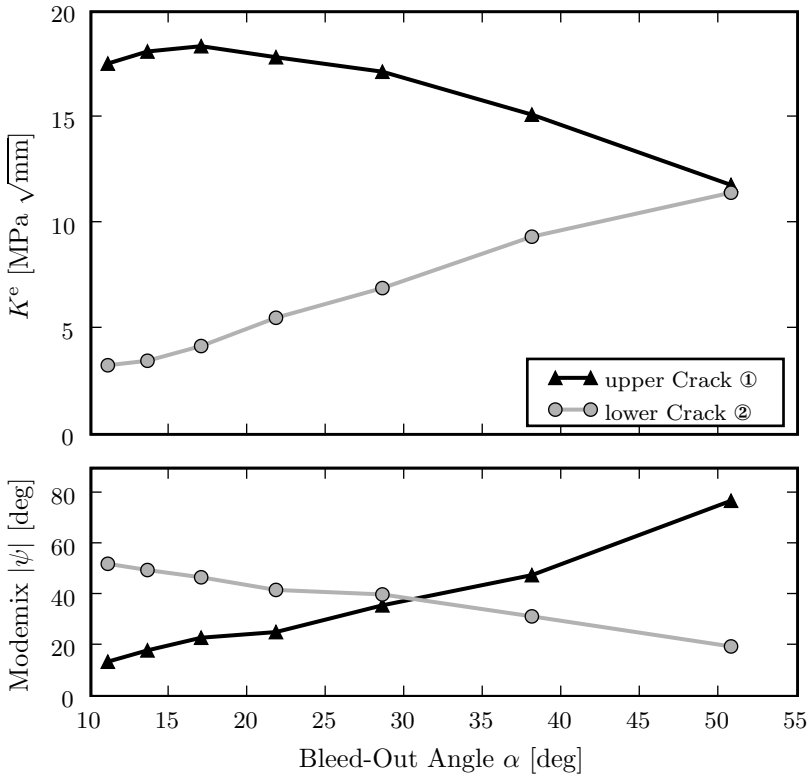

Figure 5.11: Predicted stress intensity factors and mode mixes with respect to a variation of the bleed-out angle with constant bleed-out area, and 1950 µm die length for two different crack positions.

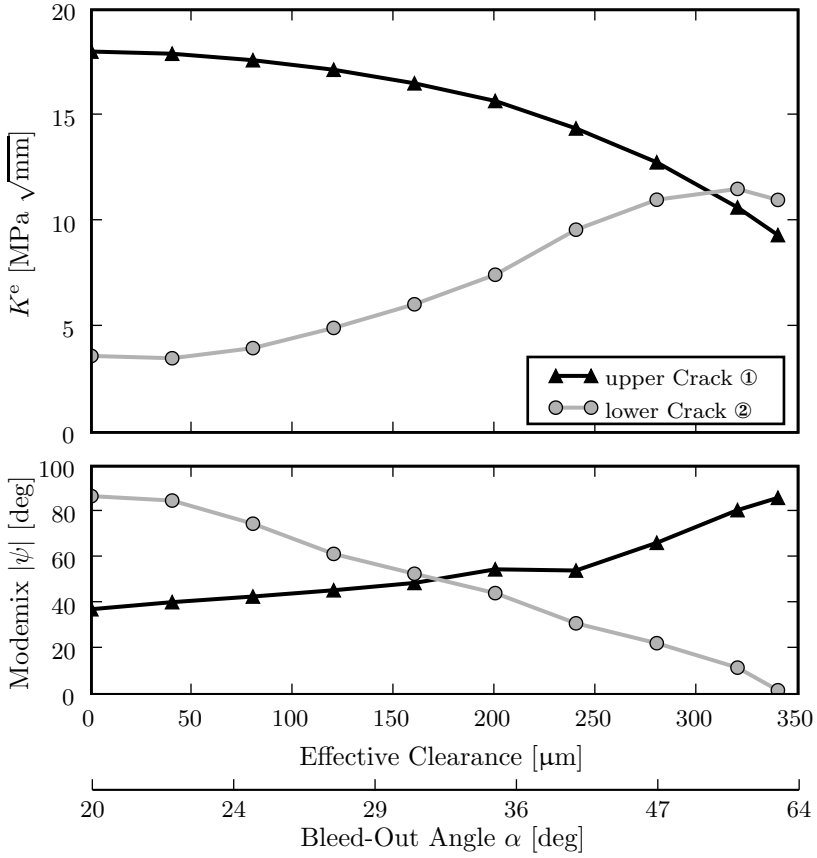

Figure 5.12: Predicted stress intensity factors and mode mixes with respect to a variation of the effective clearance with constant fillet height, and 1800 µm die length for two different crack positions.

Basic configuration – 1800 µm die length

This is the third variation of the die length. Similar to the former two, the results (Fig. 5.12, Fig. 5.13 and Fig. 5.14) encourage the statement that the die length and the clearance, respectively has no influence on the stress intensity factors and mode mixes.

Figure 5.14 shows again the decrease of the stress intensity factor for bleed-out angles below about 15°.

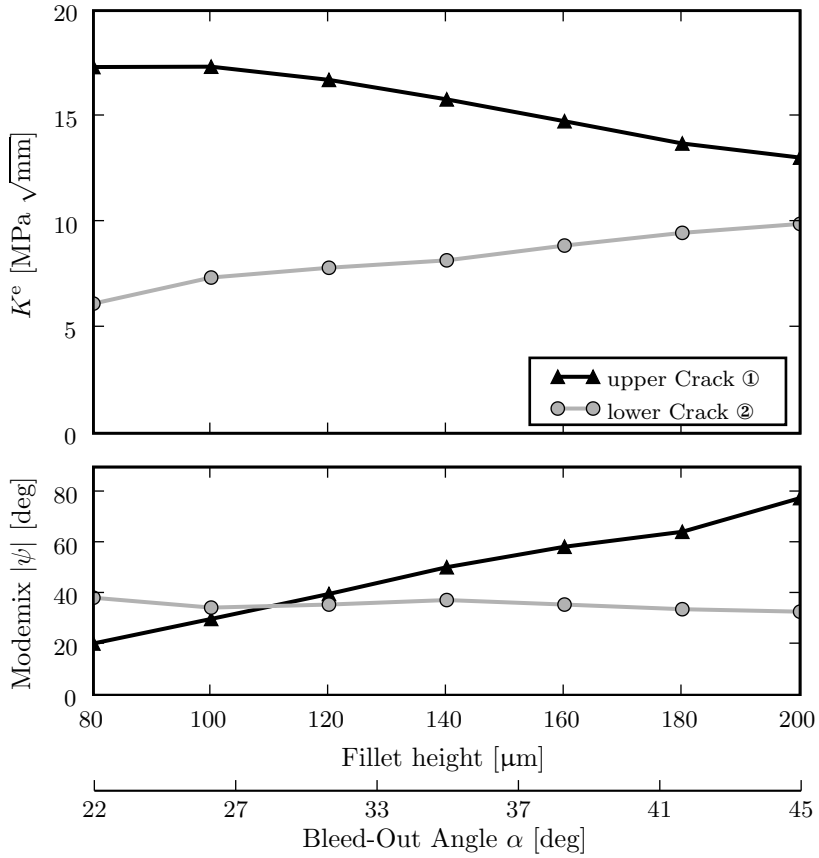

Figure 5.13: Predicted stress intensity factors and mode mixes with respect to a variation of the fillet height with constant bleed-out length, and 1800 µm die length for two different crack positions.

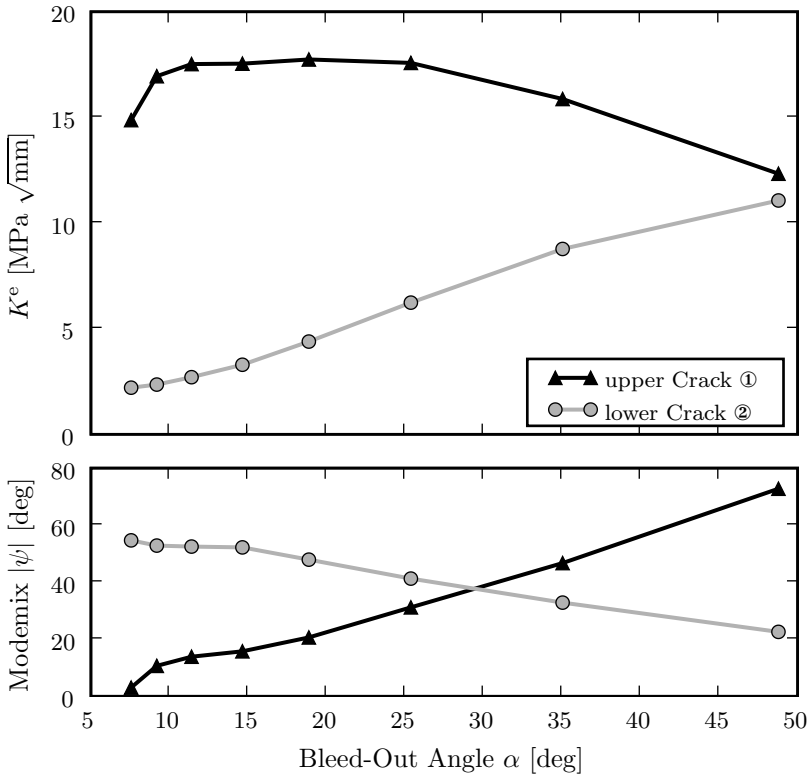

Figure 5.14: Predicted stress intensity factors and mode mixes with respect to a variation of the bleed-out angle with constant bleed-out area, and 1800 µm die length for two different crack positions.

5.2.2 Double edge configuration

The bleed-out of the double edge configuration is modeled in a more realistic way. Thus, the results are expected to be more accurate than those of the basic configuration.

Here only a die length of 1800 µm is modeled since it allows for a wide variation of the lower bleed-out angle. The upper part of the bleed-out remains untouched, see Sec. 4.7.2.

In Figure 5.15 the stress intensity factors and mode mixes affected by a variation of the lower bleed-out angle are presented. The figure shows that the upper crack is nearly uncoupled of the variation of the lower part. Especially the mode mix changes not at all. This implies that a concave shaped bleed-out is reasonable and the results obtained in Sec. 5.2.1 can be applied. Moreover, the stress intensity factor of the lower crack can be dramatically decreased by minimizing the lower bleed-out angle. Another interesting feature is that due to the big bleed-out angle of the upper part the stress intensity level is low, as shown in the previous section, e. g. Fig. 5.12.

The experimental results, provided by K-AI, show that due to the high mode mix the crack kinks out of the interface at the upper part of the bleed-out. Unfortunately, this cannot be simulated because of the lack of toughness data.

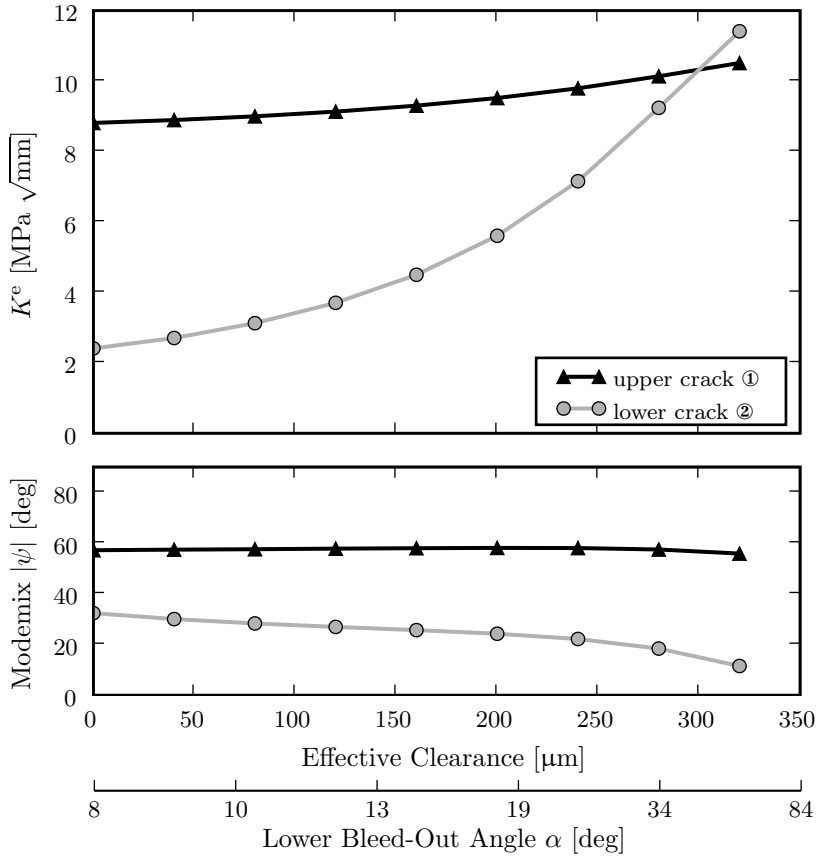

Figure 5.15: Predicted stress intensity factors and mode mixes with respect to a variation of the effective clearance with double edge configuration, and 1800 µm die length, at crack tip N for two different crack positions.

5.2.3 Crack configuration 1

The crack configuration 1 represents a basic crack extended into the lead frame – mould compound interface. As described in Sec. 4.7.2 two different variations are carried out. First, only the clearance is varied and the bleed-out geometry remains constant. And second, the bleed-out length is altered with constant clearance resulting in a variation of the bleed-out angle.

Figure 5.16 presents the stress intensity factors and mode mixes for the variation of the clearance for the upper crack tip N. As can be clearly seen, there is no influence of the clearance on the fracture mechanics parameters. This applies for both crack lengths. Based on the results of the basic configurations this is an expected behavior. One notable thing is that the overall stress intensity factor level is twice as high as the values with the basic configuration.
A completely different behavior shows the lower crack tip S. Figure 5.17 presents the stress intensity factors and mode mixes for this crack tip. Here, the stress intensity factor of the long crack (①) shows a strong dependence on the clearance but the corresponding mode mix remains stable. The strong influence on the stress intensity factors can also be seen in the traction plot in Fig. 5.18. The plot shows the interface tractions σ_{xx}, τ_{xy} along the lead frame – mould compound interface for a small and a big effective clearance (EC). The plot visualizes the influence of the stress singularity at the lead frame corner on the interface tractions. The shorter crack ② is not markedly influenced by the corner singularity. This leads to the assumption that the uncracked ligament along the die-attach – mould compound interface helps to minimize the crack tip loading.

The second variation with crack configuration 1 is a change of the bleed-out length with constant clearance. Again, this implies a variation of the bleed-out angle. Figure 5.19 shows the stress intensity factors and mode mixes for the upper crack tip with this variation for two different crack lengths. The basic characteristics of these plots resemble those of the basic configuration. Hence, an increase of the bleed-out angle leads to a lower stress intensity factor together with a high mode mix for a crack tip at an upper position (crack ①). The upper crack tip of the shorter crack ② resembles a lower crack position in the basic configuration, compare e. g. Fig. 5.5. For both cases the stress intensity factor level is considerably higher than with the basic configuration.
The characteristics of the stress intensity factors and mode mixes of the lower crack tip S are given in Fig. 5.20. This crack tip evinces a similar behavior like with the previous variation. Due to the ambiguity of the variation of the effective clearance the result is a

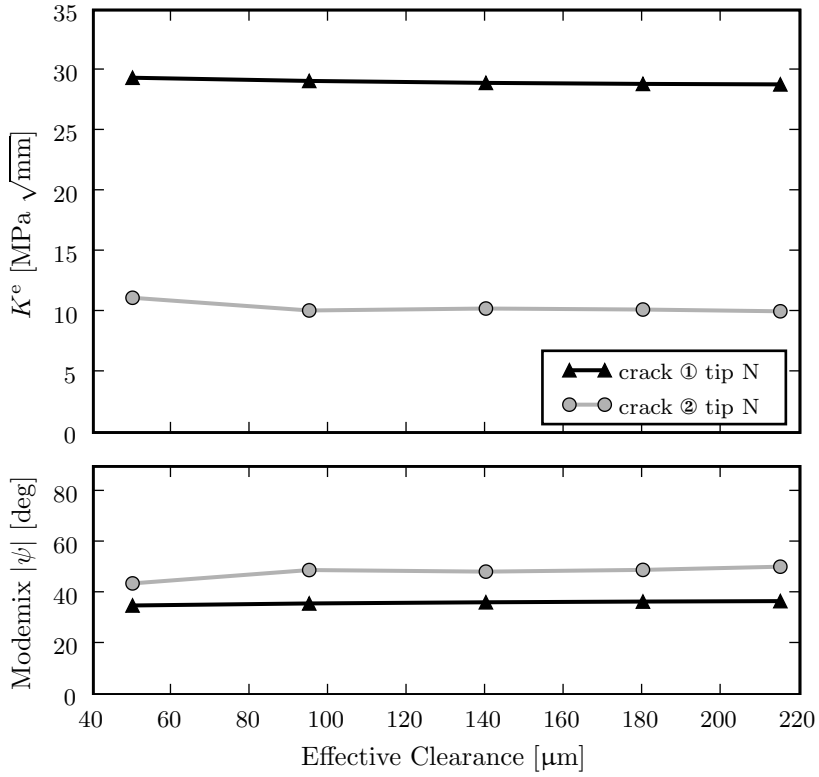

Figure 5.16: Predicted stress intensity factors and mode mixes with respect to a variation of the clearance with crack configuration 1, and constant bleed-out geometry, at crack tip N for two different crack lengths.

combination of the clearance variation and the bleed-out angle variation. A comparison of Fig. 5.20 to Fig. 5.17 visualizes that for the stress intensity factors the influence of the effective clearance dominates at the first half of the variation range. On the second half the influence of the bleed-out angle gains power. This effects are particularly visible for the long crack ①. The mode mix is mainly affected by the bleed-out angle.

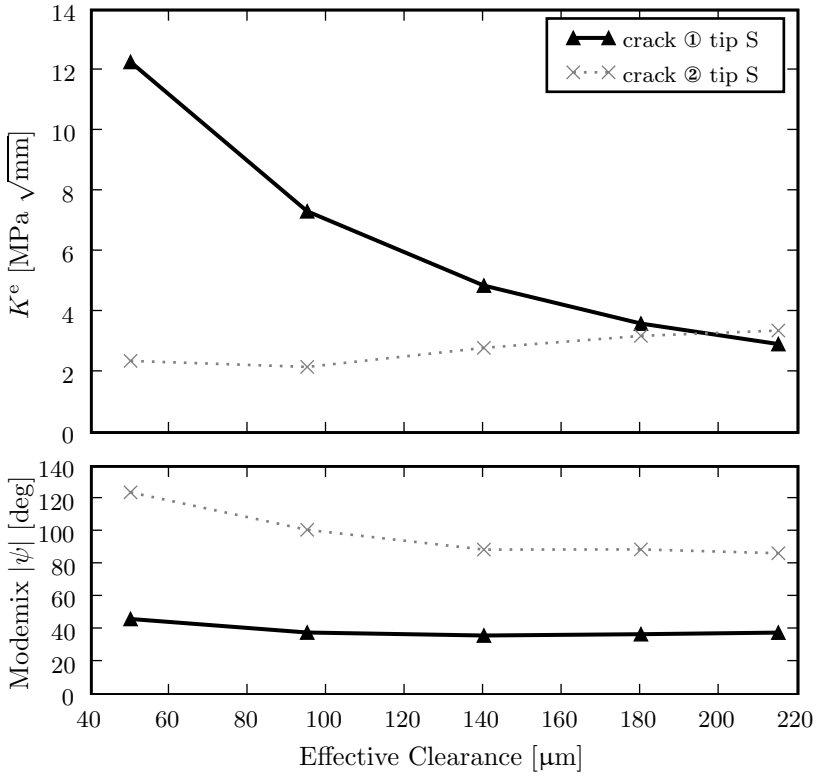

Figure 5.17: Predicted stress intensity factors and mode mixes with respect to a variation of the clearance with crack configuration 1, and constant bleed-out geometry, at crack tip S for two different crack lengths.

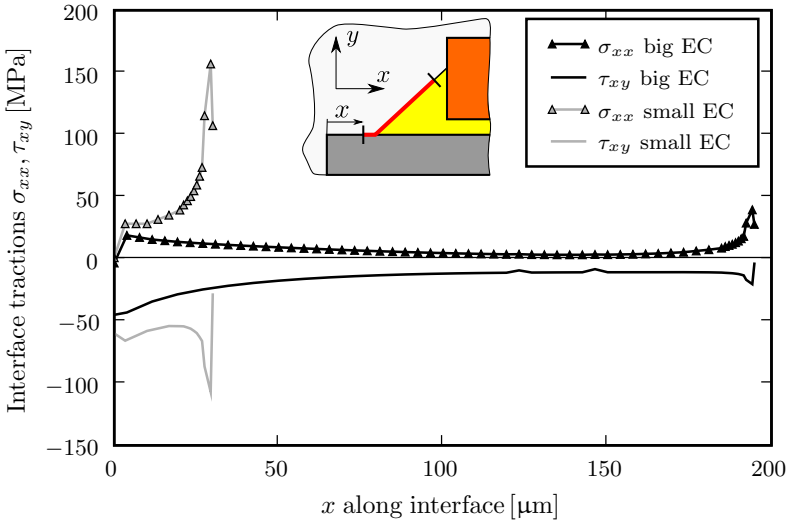

Figure 5.18: Interface tractions σ_{xx}, τ_{xy} at the lead frame – mould compound interface for two different effective clearances (EC).

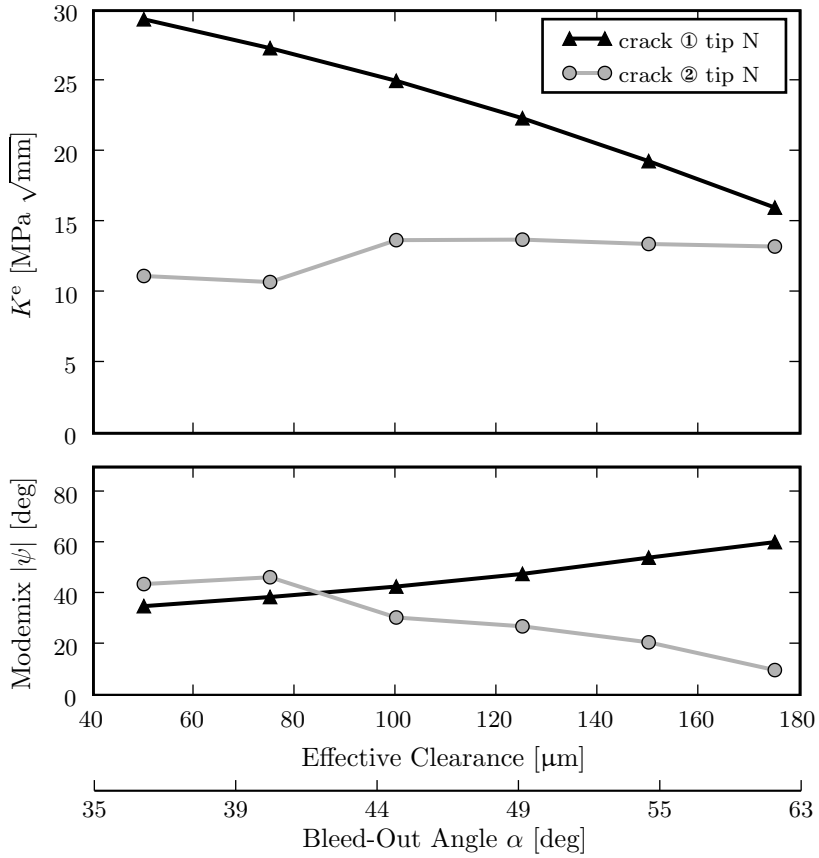

Figure 5.19: Predicted stress intensity factors and mode mixes with respect to a variation of the effective clearance with crack configuration 1, and 2130 µm die length, at crack tip N for two different crack lengths.

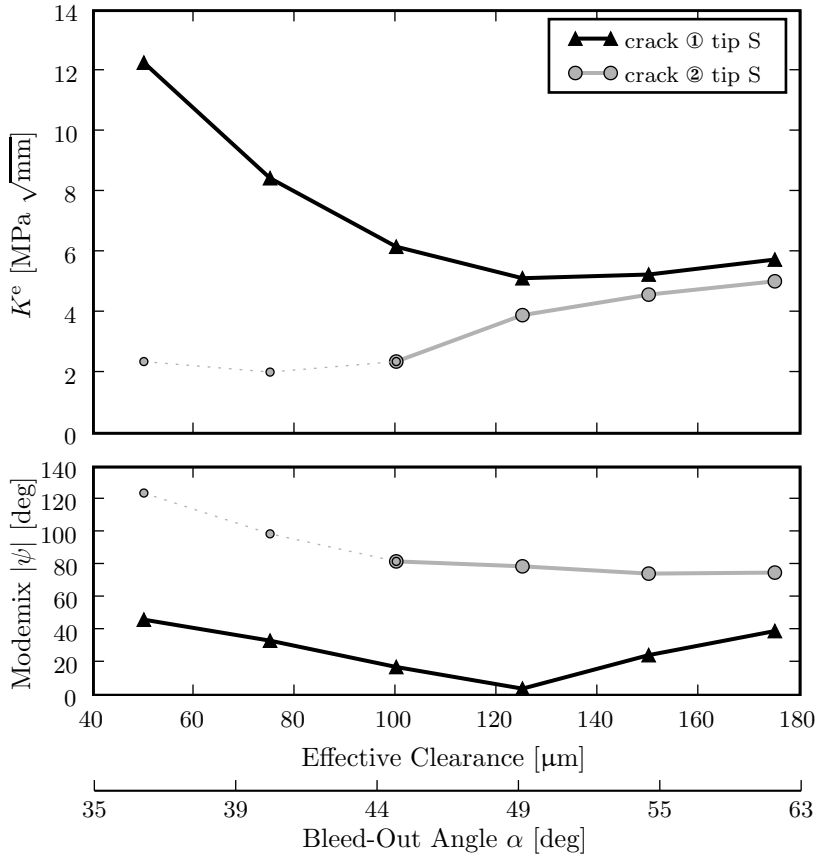

Figure 5.20: Predicted stress intensity factors and mode mixes with respect to a variation of the effective clearance with crack configuration 1, and 2130 µm die length, at crack tip S for two different crack lengths.

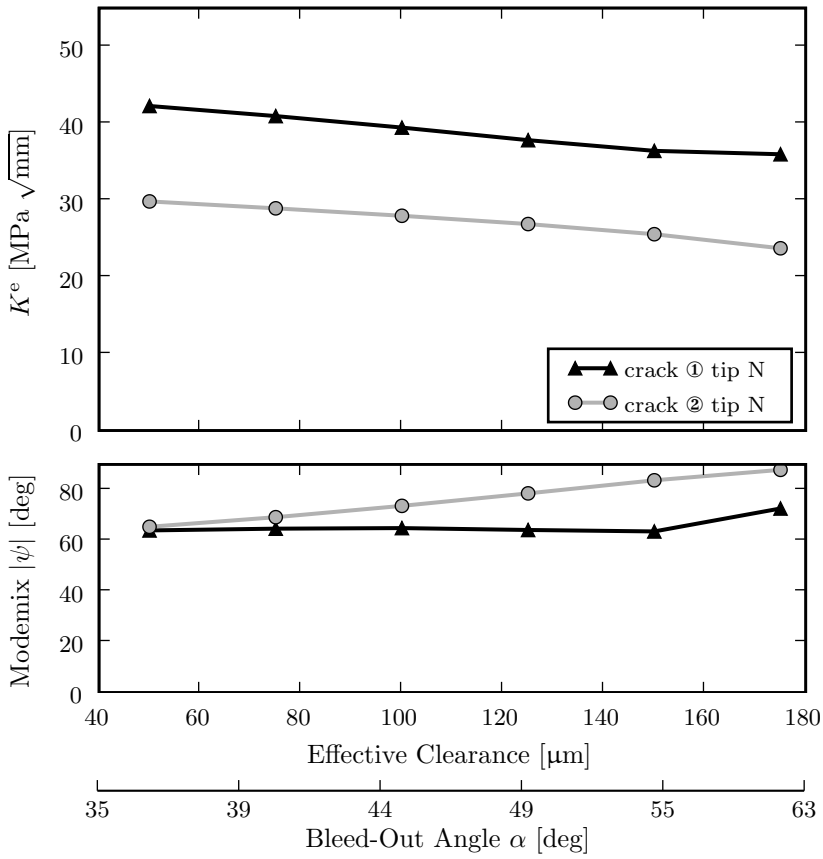

Figure 5.21: Predicted stress intensity factors and mode mixes with respect to a variation of the effective clearance with crack configuration 2, and 2130 µm die length, at crack tip N for two different crack lengths.

5.2.4 Crack configuration 2

As introduced in Sec. 4.7.2 the crack in crack configuration 2 is further extended into the die-attach – die interface. Again, two different crack lengths are examined in the following. Finally, the influence of different delamination length at the lead frame – mould compound interface is studied.

Figure 5.21 presents the stress intensity factors and mode mixes affected by a variation of the bleed-out angle. The figure shows that the variation of the bleed-out angle has only little effect on fracture mechanics parameters of the right crack tip N. It is interesting that the crack tip loading decreases the more the die-attach – die interface gets delaminated. This may lead to an arrest of the crack along this interface.

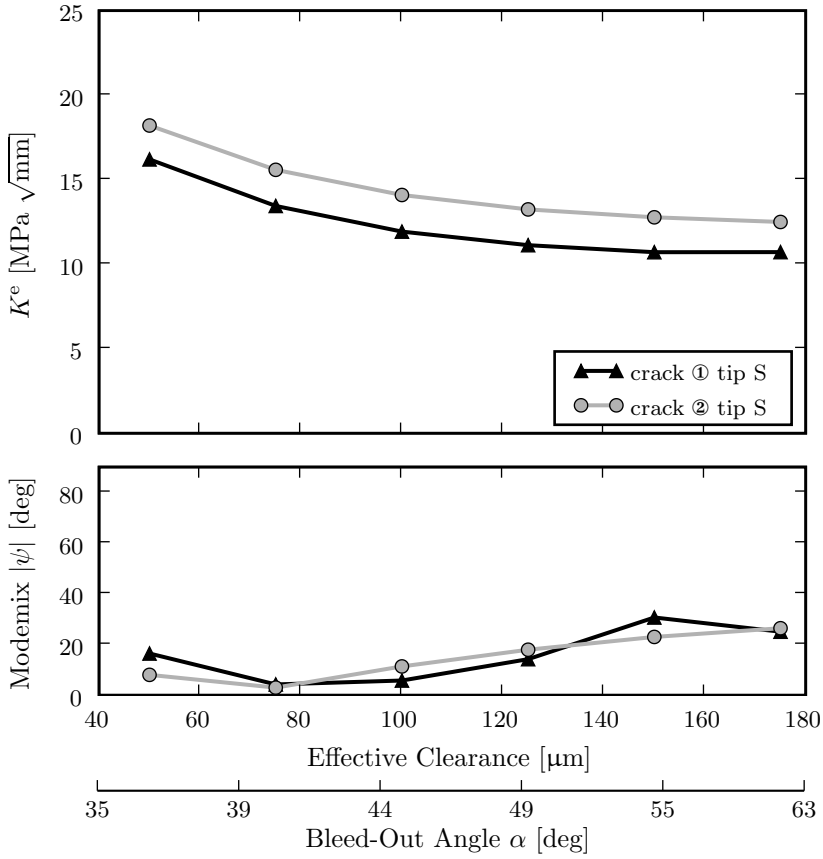

Figure 5.22: Predicted stress intensity factors and mode mixes with respect to a variation of the effective clearance with crack configuration 2, and 2130 µm die length, at crack tip S for two different crack lengths.

The stress intensity factors and mode mixes of the lower left crack tip for the current variation are given in Fig. 5.22. They show a slightly more affected behavior. The decrease of the stress intensity factor results from the increasing distance to the lead frame corner as shown before. The low mode mix combined with the high stress intensity factor compared to crack configuration 1 indicates that the lead frame – mould compound interface will fail at the latest if the crack delaminates the die-attach – die interface.

A variation of the delamination length at the lead frame – mould compound interface is considered next. The stress intensity factors and mode mixes with respect to a variation of the bleed-out angle for different delamination lengths are compared in Fig. 5.23. Here, a delamination length of 20 µm (this equals crack configuration 2), a delaminated effective clearance (EC) and a completely separated lead frame (LF) are used, see Sec. 4.7.2. The figure visualizes that this delamination length has no influence on the stress intensity

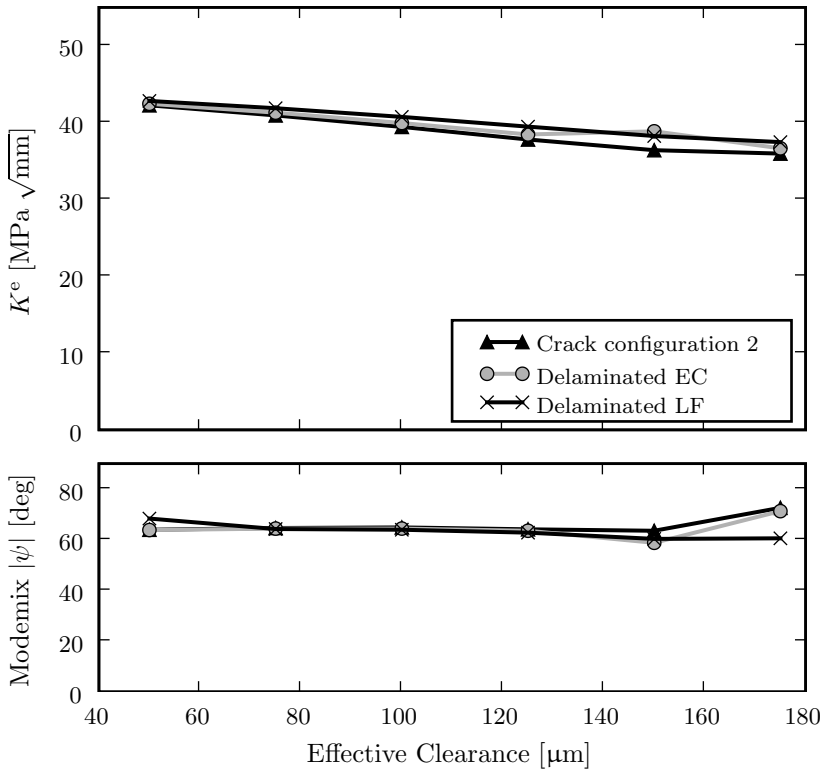

Figure 5.23: Comparison of the stress intensity factors and mode mixes with respect to a variation of the effective clearance for three different length of delamination with crack configuration 2.

factor on the right crack tip at the die-attach – die interface. A plot of the tractions σ_{xx}, τ_{xy} along the die-attach – die interface for different delamination lengths supports this finding, see Fig. 5.24. The difference of the mode mixes for higher bleed-out angles is based on the different contact conditions since due to the variation of the delamination length the crack faces get into contact at different bleed-out angles.

5.3 Findings and Conclusion

In the framework of the applied assumptions the following conclusions can be given. A combined consideration of the results of the previous sections leads to the following conclusions. If the interface between bleed-out and mould compound does not completely delaminate right after the manufacturing due to too high interface tractions, the results of the basic and double edge configuration show that a concave shaped bleed-out will be

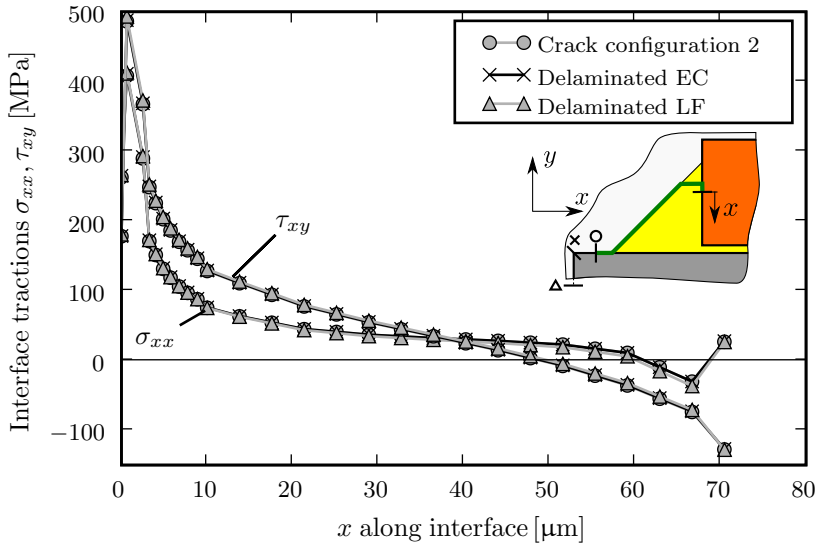

Figure 5.24: Interface tractions σ_{xx}, τ_{xy} along the die – die-attach interface for crack configuration 2, for three different delamination lengths.

the preferable design. Here, a smooth transition between die-attach – lead frame and die-attach – die, respectively, should be aimed at. Since the mode mix of a crack tip in a lower position is mainly affected by the horizontal position, a more extended interface between die-attach and lead frame would increase the fracture resistance of the die-attach – mould compound interface. However, due to the results of crack configuration 1 this would also lead to a marked increase of the stress intensity factor of an extended crack tip in the lead frame – mould compound interface. As the toughness of this interface is classified to be considerably higher than the toughness of the die-attach – mould compound interface a higher effective clearance should be aspired to increase the overall fracture resistance of the device. A comparison of the lower crack tip of configuration 1 and 2 visualizes that the crack will delaminate the effective clearance if the upper crack tip reaches and grows along the die-attach – die interface. This delamination in turn has no effect on the upper crack tip, which is an unexpected behavior. It can be explained by the very pronounced difference in thermo-mechanical properties of the die-attach and the mould compound materials. The influence of this mismatch dominates over the extension in crack length.

When dealing with long delaminated areas the symmetry condition needs to be reconsidered. If the crack has an influence on the stress field over a wide range of the modeled device a symmetry condition may be inappropriate since it assumes two equal cracks on both sides of the symmetry line. In the current cases the global stress field along the symmetry line is not affected by the cracks, thus, the symmetrical representation of the

device is applicable.

The problem reaches the limitations of the applied simulation methods at various points. Thus, it may be appropriate to extend the current work by means of, e. g., visco-elastic fracture mechanics or crack propagation methods. Furthermore, an experimental determination of the interface parameters may help to interpret and to enlarge the derived results.

Chapter 6

Summary

Semiconductor devices are build up of various materials. This multi-material-design leads to specific problems when it comes to thermal loading of the device. The manufacturing process alone introduces considerably interface tractions due to the material properties mismatch. Since typical devices are often subjected to extreme temperature variations during service, the already induced interface tractions can be increased markedly. These tractions, potentially, initiate interface cracks and, therefore, can lead to device failure, e. g., loss of electrical contact. With respect to reliability an understanding of the influences of the crack driving mechanisms and stress fields is essential to develop a reliable product.

To assess the susceptibility of crack initiation at bi-material interfaces a linear elastic fracture mechanics based approach is adapted. Hence, the stress intensity factor and the mode-mix along with the energy release rate are employed. Their computations are based on the displacement extrapolation method for the stress intensity factors and the mode mix, and on the virtual crack closure technique for the energy release rate. These fracture mechanics methods are implemented as post processing routines assuming plane strain conditions. The computation of the underlying stress and displacement fields is done by the finite element method. They are verified by two example problems with available analytical solutions.

For the numerical simulation of a semiconductor device a two dimensional representation of the devices' cross section in conjunction with a proper level of abstraction and simplification is used. The stress, strain, and displacement fields are computed by the Finite Element Method, which allows simulating multi-material components under thermo-mechanical loads. Generalized plane strain conditions are assumed. At the crack tips,

special purpose "crack tip elements" with square-root singularity are used. To characterize the acting crack tip situation the fracture mechanics methods are applied. Thus, initial interface cracks have to be placed at certain interfaces. The manufacturing process is simulated and the interface cracks are assumed to exist after the manufacturing. A thermo-elastic simulation is carried out assuming a homogeneous cool-down of the whole device to the minimal considered temperature. Finally, the crack tips are classified by the fracture mechanics methods.

The aim of this thesis is to identify certain geometry parameters which have a potential impact on the susceptibility of crack initiation. A special focus is laid on the effective clearance which is the area between lead frame corner and bleed-out corner at the lead frame – mould compound interface. Various geometry and crack configurations are simulated to obtain an understanding of the stress fields and, consequently, the fracture mechanics parameters. For the studied parameter combinations, the risk of interface crack initiation was assessed and compared qualitatively, as no critical interface toughnesses and mode mix criteria are available.

A simple triangular bleed-out shape reveals that the effective clearance alone has no influence on the fracture parameters as long as the crack remains in the die-attach – mould compound interface. Rather, the bleed-out angle, which can be controlled by the effective clearance, is the parameter with the main influence on the crack tips in this simple situation. If the crack is extended into the lead frame – mould compound interface the effective clearance shows a strong influence on the crack tip at this interface. A variation of the bleed-out angle shows in all configurations a strong influence leading to the result that a concave shaped bleed-out is the preferable design. This is especially suggested by means of a more realistic bleed out shape at the double edge configuration. A crack extended to both sides, into the lead frame – mould compound and the die-attach – die interface shows that the crack tip in the latter interface is not affected by the extension length on the other interface. This means, the delamination of the lead frame does not alter the stress state at the die-attach – die interface. This somehow unexpected result can be explained by the severe mismatch in thermo-elastic material properties of the mould compound and die-attach.

Finally, it can be said that the applied approach is shown to give a useful tool at hand for computational investigations of interface cracks in semiconductor devices. A variety of configurations can be studied and their effect on interface crack initiation can be predicted. In combination with available interface toughness data quantitative results and reliability statements can be given.

Bibliography

[1] A. Agrawal and A. Karlsson. Obtaining mode mixity for a bimaterial interface crack using the virtual crack closure technique. *International Journal of Fracture*, 141(1): 75–98, 2006.

[2] A. Ayhan and H. Nied. Finite element analysis of interface cracking in semiconductor packages. *Components and Packaging Technologies, IEEE Transactions on*, 22(4): 503–511, 1999.

[3] L. Banks-Sills and D. Ashkenazi. A note on fracture criteria for interface fracture. *International Journal of Fracture*, 103(2):177–188, 2000.

[4] G. I. Barenblatt. The mathematical theory of of equilibrium cracks in brittle fracture. In H. Dryden and T. von Kármán, editors, *Advances in Applied Mechanics*, volume 7, pages 55–129. Academic Press, 1962.

[5] R. Bitsche. *Design and computational analysis of compound castings and other multi-material structures*. PhD thesis, Technical University of Vienna, 2009.

[6] B. A. Boley and J. H. Weiner. *Theory of Thermal Stresses*. Krieger Pub Co, 1985.

[7] A. F. Bower. *Applied Mechanics of Solids*. CRC Press, 2009.

[8] A. Carpinteri and M. Paggi. Analytical study of the singularities arising at multi-material interfaces in 2D linear elastic problems. *Engineering Fracture Mechanics*, 74 (1-2):59–74, 2007.

[9] A. Carpinteri and M. Paggi. Asymptotic analysis in linear elasticity: From the pioneering studies by Wieghardt and Irwin until today. *Engineering Fracture Mechanics*, 76(12):1771–1784, 2009.

[10] M. Comninou. The interface crack. *Journal of Applied Mechanics*, 44:631–636, 1977.

[11] A. Cornec, I. Scheider, and K.-H. Schwalbe. On the practical application of the cohesive model. *Engineering Fracture Mechanics*, 70(14):1963 – 1987, 2003. Cohesive Models.

[12] R. de Borst. Numerical aspects of cohesive-zone models. *Engineering Fracture Mechanics*, 70(14):1743 – 1757, 2003. Cohesive Models.

[13] M. Elices, G. V. Guinea, J. Gmez, and J. Planas. The cohesive zone model: advantages, limitations and challenges. *Engineering Fracture Mechanics*, 69(2):137–163, 2002.

[14] F. Erdogan. Stress distribution in nonhomogeneus elastic plane with cracks. *Journal of Applied Mechanics*, 30:232–236, 1963.

[15] F. Erdogan. Stress distribution in bonded dissimilar materials with cracks. *Journal of Applied Mechanics*, 32:403–410, 1965.

[16] F. Erdogan. Fracture mechanics. *International Journal of Solids and Structures*, 37 (1-2):171–183, 2000.

[17] Y. Freed and L. Banks-Sills. A new cohesive zone model for mixed mode interface fracture in bimaterials. *Engineering Fracture Mechanics*, 75(15):4583–4593, 2008.

[18] W. Grellmann and S. Seidler. *Deformation and Fracture Behaviour of Polymers (Engineering Materials)*. Springer, 1 edition, 2001.

[19] D. Gross and T. Seelig. *Bruchmechanik: Mit einer Einführung in die Mikromechanik (German Edition)*. Springer, 4. bearb. aufl. edition, 2006.

[20] G. V. Guinea, J. Planas, and M. Elices. K_{I} evaluation by the displacement extrapolation technique. *Engineering Fracture Mechanics*, 66(3):243–255, 2000.

[21] S. M. Hu. Stress-related problems in silicon technology. *Journal of Applied Physics*, 70(6):R53–R80, 1991.

[22] J. W. Hutchinson and Z. Suo. Mixed mode cracking in layered materials. *Advances in Applied Mechanics*, 29:63–191, 1992.

[23] J. W. Hutchinson, M. Mear, and J. R. Rice. Crack paralleling an interface between dissimilar materials. *Journal of Applied Mechanics*, 54:828–832, 1987.

[24] C. Hwu and J. S. Hu. Stress intensity factors and energy release rates of delaminations in composite laminates. *Engineering Fracture Mechanics*, 42(6):977–988, 1992.

[25] T. Ikeda and C. Sun. Stress intensity factor analysis for an interface crack between dissimilar isotropic materials under thermal stress. *International Journal of Fracture*, 111(3):229–249, 2001.

[26] Z.-H. Jin and C. Sun. Cohesive zone modeling of interface fracture in elastic bi-materials. *Engineering Fracture Mechanics*, 72(12):1805–1817, 2005.

[27] R. Khandelwal and J. C. Kishen. Complex variable method of computing J_k for bi-material interface cracks. *Engineering Fracture Mechanics*, 73(11):1568–1580, 2006.

[28] R. Khandelwal and J. C. Kishen. The use of conservative integral in bi-material interface crack problems subjected to thermal loads. *International Journal of Solids and Structures*, 45(10):2976–2992, 2008.

[29] R. Khandelwal and J. M. C. Kishen. Computation of thermal stress intensity factors for bimaterial interface cracks using domain integral method. *Journal of Applied Mechanics*, 76(4):041010, 2009.

[30] K. Kishimoto, M. Omiya, and W. Yang. Fracture mechanics of bonding interface: a cohesive zone model. *Sensors and Actuators A: Physical*, 99(1-2):198–206, 2002.

[31] T. Kobayashi. *Strength and Toughness of Materials*. Springer, 2004.

[32] R. Krueger. Virtual crack closure technique: History, approach, and applications. *Applied Mechanics Reviews*, 57(2):109–143, 2004.

[33] M. Kuna. *Numerische Beanspruchungsanalyse von Rissen (Finite Elemente in der Bruchmechanik)*. Vieweg+Teubner, 2008.

[34] S. Liu, Y. Mei, and T. Wu. Bimaterial interfacial crack growth as a function of mode-mixity. *IEEE Transactions on Components, Packaging, and Manufacturing Technology, Part A*, 18(3):618–626, 1995.

[35] V. Mantič and F. París. Relation between SIF and ERR based measures of fracture mode mixity in interface cracks. *International Journal of Fracture*, 130(2):557–569, 2004.

[36] G. Marannano, L. Mistretta, A. Cirello, and S. Pasta. Crack growth analysis at adhesive-adherent interface in bonded joints under mixed mode I/II. *Engineering Fracture Mechanics*, 75(18):5122–5133, 2008.

[37] M. Marder and J. Fineberg. How things break. *Physics Today*, 49(9):24–29, 1996.

[38] P. P. L. Matos, R. M. McMeeking, P. G. Charalambides, and M. D. Drory. A method for calculating stress intensities in bimaterial fracture. *International Journal of Fracture*, 40(4):235–254, 1989.

[39] S. Meguid. *Engineering Fracture Mechanics*. Springer, 1 edition, 1989.

[40] Y. Murakami. *Stress intensity factors handbook*. Number 1–5. Pergamon Press, 1987.

[41] J. Mnguez. Foreman's crack growth rate equation and the safety conditions of cracked structures. *Engineering Fracture Mechanics*, 48(5):663–672, 1994.

[42] K. B. Narayana and B. Dattaguru. Certain aspects related to computation by modified crack closure integral. *Engineering Fracture Mechanics*, 55(2):335–339, 1996.

[43] A. Needleman. A continuum model for void nucleation by inclusion debonding. *Journal of Applied Mechanics*, 54:525–531, 1987.

[44] H. Nied. Mechanics of interface with applications in electronic packaging. *Device and Materials Reliability, IEEE Transactions on*, 3(4):129–143, Dec. 2003.

[45] J. Planas, M. Elices, G. V. Guinea, F. J. Gmez, D. A. Cendn, and I. Arbilla. Generalizations and specializations of cohesive crack models. *Engineering Fracture Mechanics*, 70(14):1759–1776, 2003.

[46] W. Qian and C. T. Sun. Methods for calculating stress intensity factors for interfacial cracks between two orthotropic solids. *International Journal of Solids and Structures*, 35(25):3317–3330, 1998.

[47] I. Raju. Calculation of strain-energy release rates with higher order and singular finite elements. *Engineering Fracture Mechanics*, 28(3):251–274, 1987.

[48] N. Ramanujam, P. Vaddadi, T. Nakamura, and R. P. Singh. Interlaminar fatigue crack growth of cross-ply composites under thermal cycles. *Composite Structures*, 85 (2):175–187, 2008.

[49] J. R. Rice. A path independent integral and the approximate analysis of strain concentration by notches and cracks. *Journal of Applied Mechanics*, 35:379–386, 1968.

[50] J. R. Rice. Elastic fracture mechanics concepts for interfacial cracks. *Journal of Applied Mechanics*, 55:98–103, 1988.

[51] J. R. Rice and G. C. Sih. Plane problems of cracks in dissimilar materials. *Journal of Applied Mechanics*, 32:418–423, 1965.

[52] K. L. Roe and T. Siegmund. An irreversible cohesive zone model for interface fatigue crack growth simulation. *Engineering Fracture Mechanics*, 70(2):209–232, 2003.

[53] E. Rybicki and M. Kanninen. A finite element calculation of stress intensity factors by a modified crack closure integral. *Engineering Fracture Mechanics*, 9(4):931–938, 1977.

[54] M. H. Shirangi, A. Gollhardt, A. Fischer, W. H. Müller, and B. Michel. Investigation of fracture toughness and displacement fields of copper/polymer interface using image correlation technique. In *IMAPS 2008 - 41st International Symposium on Microelectronics*, 2008.

[55] S. Shkarayev, E. Madenci, M. Ibnabdeljalil, and M. P. Savruk. Analytical stress singularities for a crack at a bi- or triple junction of dissimilar materials with bilinear behavior. *Engineering Fracture Mechanics*, 68(4):475–486, 2001.

[56] L. I. Slepyan. *Models and Phenomena in Fracture Mechanics (Foundations of Engineering Mechanics)*. Springer, 2002.

[57] P. M. Stipan, B. C. Beihoff, and M. C. Shaw. *The Electronic Packaging Handbook*, chapter Electronics Package Reliability and Failure Analysis: A Micromechanics-Based Approach. CRC Press, 2000.

[58] M. Stojek, M. Stommel, and W. Korte. *Finite-Elemente-Methode für die Auslegung von Kunststoff- und Elastomerbauteilen*. Springer-VDI-Verlag GmbH, 1998.

[59] C. Sun and Z.-H. Jin. Modeling of composite fracture using cohesive zone and bridging models. *Composites Science and Technology*, 66(10):1297–1302, 2006.

[60] C. T. Sun and W. Qian. The use of finite extension strain energy release rates in fracture of interfacial cracks. *International Journal of Solids and Structures*, 34(20): 2595–2609, 1997.

[61] H. Tada, P. Paris, and G. Irwin. *The stress analysis of cracks handbook*. Paris Production Inc., 2 edition, 1985.

[62] A. A. O. Tay. Modeling of Interfacial Delamination in Plastic IC Packages Under Hygrothermal Loading. *Journal of Electronic Packaging*, 127(3):268–275, 2005.

[63] T. Tay. Characterization and analysis of delamination fracture in composites: An overview of developments from 1990 to 2001. *Applied Mechanics Reviews*, 56(1):1–32, 2003.

[64] M. E. Thurston and A. T. Zehnder. Nickel-alumina interfacial fracture toughness: experiments and analysis of residual stress effects. *International Journal of Fracture*, 76(3):221–241, 1995.

[65] T. C. T. Ting. *Anisotropic Elasticity : Theory and Applications*. Oxford University Press, 1996.

[66] W. van Driel, P. Habets, M. van Gils, and G. Zhang. Characterization of interface strength as function of temperature and moisture conditions. In *Electronic Packaging Technology, 2005 6th International Conference on*, pages 1–6, Sept. 2005.

[67] W. van Driel, M. van Gils, R. van Silfhout, and G. Zhang. Prediction of Delamination Related IC & Packaging Reliability Problems. *Microelectronics and Reliability*, 45(9-11):1633–1638, 2005.

[68] M. L. Williams, R. F. Landel, and J. D. Ferry. The temperature dependence of relaxation mechanisms in amorphous polymers and other glass-forming liquids. *Journal of the American Chemical Society*, 77(14):3701–3707, 1955.

[69] G. Wimmer. *Computational methods for the prediction of emergence and growth of delaminations in laminated composite components*. PhD thesis, Technical University of Vienna, 2009.

[70] A. Xiao, G. Schlottig, H. Pape, B. Wunderle, K. Jansen, and L. Ernst. Mixed mode interface characterization considering thermal residual stress. In *International Conference on Electronic Packaging Technology & High Density Packaging, 2008*, pages 1–7, 2008.

[71] D. Xie, A. M. Waas, K. W. Shahwan, J. A. Schroeder, and R. G. Boeman. Fracture criterion for kinking cracks in a tri-material adhesively bonded joint under mixed mode loading. *Engineering Fracture Mechanics*, 72(16):2487–2504, 2005.

[72] R. Yuuki and S.-B. Cho. Efficient boundary element analysis of stress intensity factors for interface cracks in dissimilar materials. *Engineering Fracture Mechanics*, 34(1): 179–188, 1989.